

1 **Segmentation and Holocene Behavior of the Middle Strand of the North Anatolian**
2 **Fault (NW Turkey)**

3 **Y. Benjelloun¹, J. de Sigoyer², S. Garambois², J. Carcaillet², and Y. Klinger¹**

4 ¹Université de Paris, Institut de physique du globe de Paris, CNRS, F-75005 Paris, France.

5 ²Univ. Grenoble Alpes, Univ. Savoie Mont Blanc, CNRS, IRD, IFSTTAR, ISTERre, 38000
6 Grenoble, France.

7 Corresponding author: Yacine Benjelloun (benjelloun@ipgp.fr)

8 **Key Points:**

- 9 • Systematic measurements of horizontal cumulative offsets along the middle strand of
10 the North Anatolian fault
- 11 • Statistical analysis of the dataset allows to identify the last large ruptures along the
12 fault and the associated slip per-segment
- 13 • Comparison with independent constraints on past earthquakes leads to discuss past
14 rupture scenarios

15

16

17

18

19

20

21

22 **Abstract**

23 The North Anatolian fault in the Marmara region is composed of three parallel strands all
24 separated by ~50 km. The activity of the middle strand, which borders the southern edge of
25 the Marmara Sea, is much debated because of its present-day very low seismicity. The weak
26 seismic activity observed today along the middle strand contrasts with historical,
27 archaeological and paleoseismological evidence, which suggest several destructive
28 earthquakes have occurred during the last 2000 years. Our study aims to better constrain
29 seismic hazard on the middle strand by exploring its Holocene paleoseismicity. For this, we
30 mapped 148 km of the middle strand, using high-resolution satellite imagery. A series of
31 landforms offset by the middle strand activity have been systematically measured to recover
32 the past ruptures. Three Late Pleistocene-Holocene terraces have been dated with the
33 terrestrial cosmogenic nuclide method, constraining a horizontal slip rate of ~4.3 mm/yr. The
34 statistical analysis of the offsets evidences several major ruptures preserved in the landscape,
35 with coseismic lateral displacements ranging between 3 and 6.5 m. This corresponds to Mw
36 ~7.3 earthquakes able to propagate along several fault segments. As the approach used can
37 only resolve large magnitude events, smaller events (e.g. Mw 6.8-7) likely occurred as well
38 even if their geomorphological signature could not be detected. Historical seismicity and
39 paleoseismology data suggest that the last large earthquakes along the MNAF happened in
40 1065 CE and between the 14th and 18th centuries CE. Since then, the MNAF may have
41 accumulated enough stress to generate a destructive rupture.

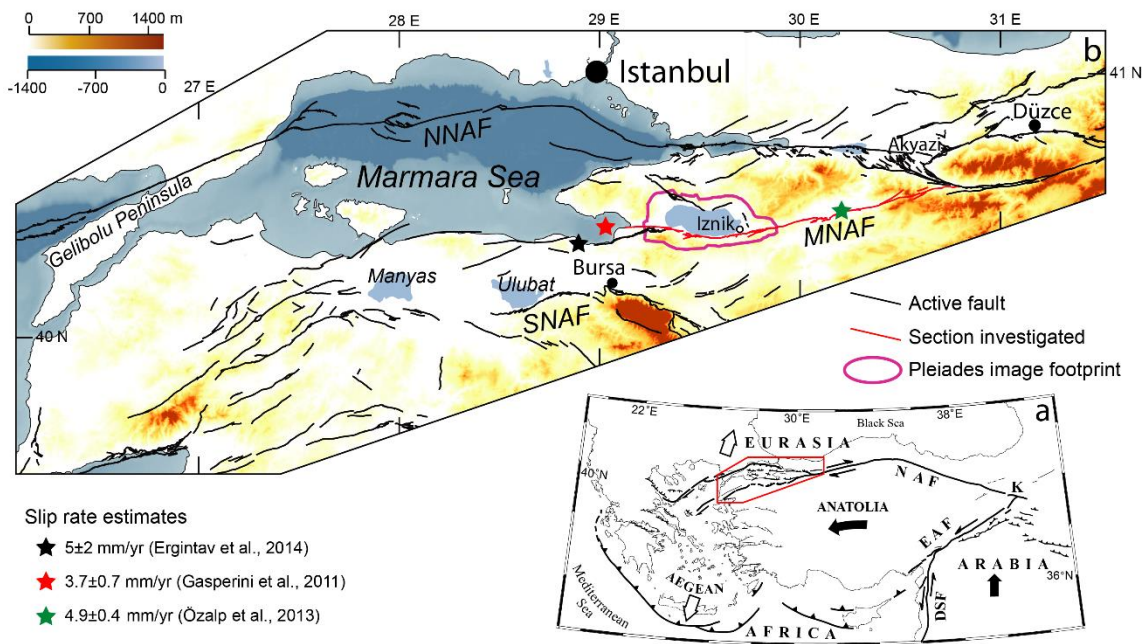
42

43 **1 Introduction**

44 Seismic hazard in the highly inhabited areas of northwestern Turkey is mainly related to the
45 activity of the North Anatolian fault (NAF), a 1000-km long, dextral strike-slip structure that

46 accommodates the relative motion between the Eurasian and Anatolian blocks, with a total
47 geodetic slip estimated around 3 cm/yr (Fig. 1; McClusky et al., 2000; Meade et al., 2002).
48 During the 20th century, the NAF ruptured almost entirely during a westward sequence of
49 major earthquakes from Erzincan, in 1939, to Düzce and Izmit, in 1999 (Ambraseys, 2001a;
50 Hubert-Ferrari et al., 2000; Stein et al., 1997). A seismic gap remains in the Sea of Marmara,
51 in front of Istanbul, where a major earthquake is expected to occur in the next decades
52 (Parsons et al., 2000). In addition to the main northern strand of the NAF, one should also
53 consider the seismic hazard due to the presence of two secondary strands known as the middle
54 and southern strands (MNAF and SNAF, Fig. 1). The deformation rate on these strands is less
55 constrained, although they could together accommodate as much as 25% of the total slip of
56 the NAF (Armijo et al., 2002; Flerit et al., 2003), with estimated slip rates between 3 and 5
57 mm/yr on the MNAF (Ergintav et al., 2014; Gasperini et al., 2011; Özalp et al., 2013). While
58 the SNAF experienced a Mw 7.2 earthquake in 1953 (Kürçer et al., 2008), no major
59 earthquake ruptured the MNAF during the instrumental period, and the seismicity of the
60 MNAF zone during the last eight decades does not include more than a couple of earthquakes
61 larger than Mw 5. The microseismicity recently recorded has been mostly located west of
62 Iznik Lake and around the Gulf of Gemlik, while the other segments in the east have been
63 characterized by much fewer events and appear quiescent compared with the neighboring
64 NAF strands (Baris et al., 2002; Gürbüz et al., 2000; Öztürk et al., 2009; Tsukuda et al.,
65 1988). These observations explain that the middle strand has often been overlooked in the
66 assessment of deformation of the Marmara region (Le Pichon et al., 2014). This current
67 quiescence contrasts with a significant historical seismic activity documented by several
68 chronicles mentioning the destruction of Iznik and other surrounding cities located close to
69 the MNAF during large earthquakes occurring in the last 2000 years (Ambraseys, 2002, 2009;
70 Ambraseys & Finkel, 1991; Ambraseys & Jackson, 1998; Guidoboni & Comastri, 2005; Fig.

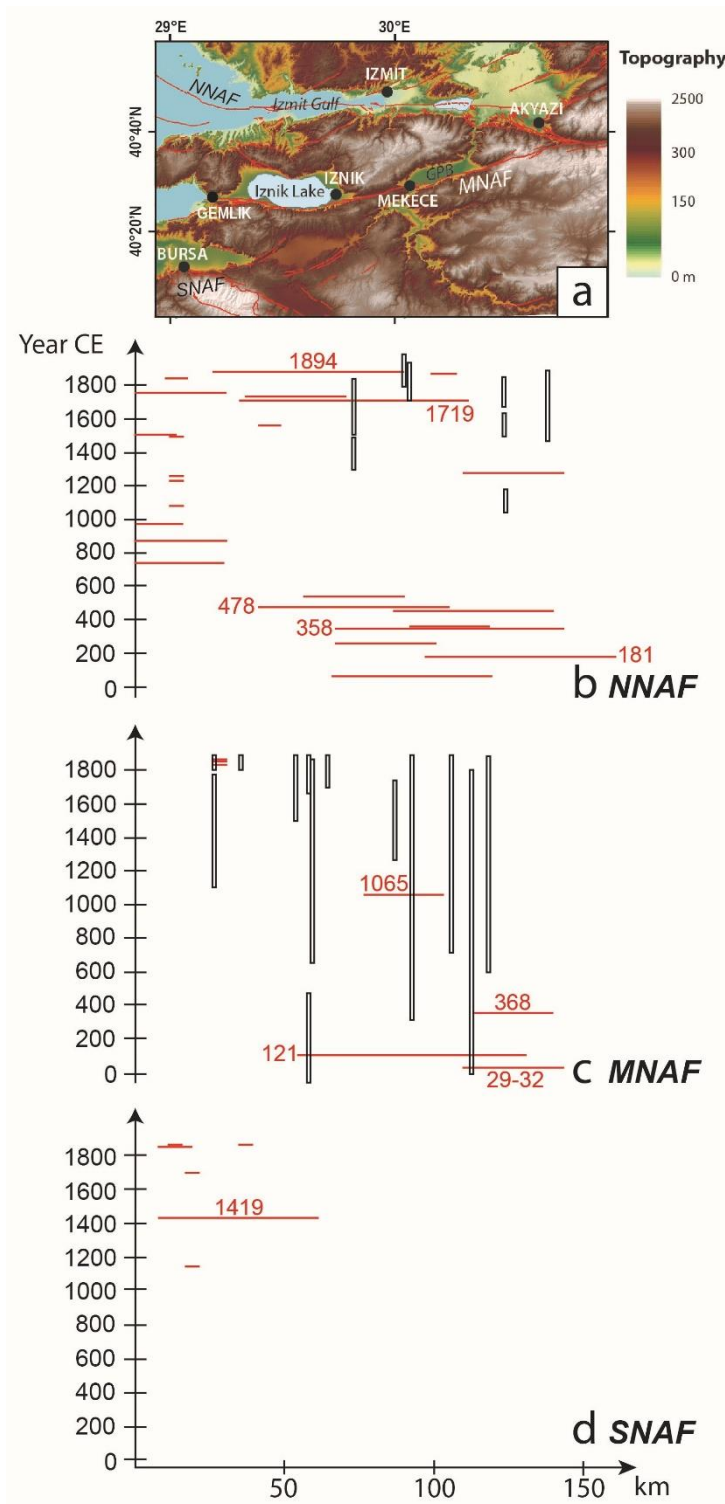
71 2). This calls for a refinement of the paleoseismic activity of this fault zone.



79

80 **Figure 1.** General tectonic context. (a) Schematic map of the main active fault zones of the
81 Eastern Mediterranean (Armijo et al., 1999). NAF = North Anatolian fault, EAF = East
82 Anatolian fault, DSF = Dead Sea fault. The red box surrounds the Marmara region. (b) Main
83 active faults located within the Marmara region. The fault map was modified from Emre et al.
84 (2011). NNAF, MNAF and SNAF refers to the northern, middle and southern strand of the
85 NAF respectively. The bathymetry comes from the EMODnet Bathymetry Consortium
86 (2018). The color stars locate fault sections where slip rates were estimated by geodesy or
87 geomorphology studies (see Section 3 for details).

88



89

90 **Figure 2.** Historical seismicity of the eastern Marmara region before 1900 CE (Common Era).

91 (a) Active faults and main geographic features of the Marmara region. GPB=Geyve-

92 Pamukova Basin. (b, c, d) Historical earthquakes (horizontal red bars) and seismic events

93 documented in palaeoseismological trenches (vertical boxes) along the three strands of the

94 NAF. The horizontal bars are positioned according to the epicentral areas interpreted from the
95 sources. These epicentral areas are determined from the spatial distribution of the seismic
96 intensities interpreted from historical descriptions, and their accuracy depends on the
97 availability and quality of the written archives (Ambraseys et al., 2002). The length of each
98 horizontal bar corresponds to the approximate rupture length of the earthquake. To estimate
99 this length, we rely on the magnitude estimated by historical seismology studies (see Table S1
100 in Supporting Information), from which a surface rupture length was derived using the
101 relationship of Wells and Coppersmith (1984). The length of the vertical boxes corresponds to
102 the dating of the events within 2σ uncertainty (Civico et al., 2021; Dikbas et al., 2018; Dogan,
103 2010; Honkura & Isikara, 1991; Ikeda, Suzuki et al., 1991; Klinger et al., 2003; Özalp et al.,
104 2013; Rockwell et al., 2009; see Table S2 in Supporting Information for detailed data).

105

106 In the last decades, the development of high-resolution satellite imagery has made it possible
107 to measure the deformation and characterize in great detail the geomorphology of tectonically
108 active regions on a large scale (Elliott et al., 2016; Fu et al., 2004; Klinger et al., 2011; Ren et
109 al., 2018). These images enable us to accurately map active faults along several tens of
110 kilometers, to describe their segmentation and therefore provide useful information on the
111 possible extension of a given rupture (e.g. Ansberque et al., 2016; Choi et al., 2018; Klinger et
112 al., 2005). Such data also make it possible to document the long-term, cumulative slip
113 distribution along the fault through inventories of offset geomorphological markers. This
114 approach has been successfully employed since the 1960s on various faults to extract
115 coseismic slip values from cumulative offset measurements, and to discuss the impact of
116 segmentation in modulating the cumulative along-strike displacement (Ansberque et al., 2016;
117 Barka, 1996; Manighetti et al., 2015, 2020; McGill and Rubin, 1999; Sieh and Jahns, 1984;
118 Zielke et al., 2015; Kurtz et al., 2018).

119 In this study, we use a set of high-resolution images and topography measurements obtained
120 from Pleiades data to map the eastern part of the MNAF between Gemlik and Akyazi district
121 (Fig. 2a), and to measure a series of lateral displacements recorded by geomorphological
122 markers, mainly stream talwegs and risers. To gather additional age control on the observed
123 cumulative deformation, we sample and date three levels of wave-cut terraces formed around
124 Iznik Lake. This enables us to constrain a Holocene horizontal slip-rate for the central section
125 of the MNAF. A statistical analysis of the offset measurements helps us to extract coseismic
126 displacements for several of the largest past earthquakes and to discuss the slip distribution
127 generated along the fault during these earthquakes. Comparison of these data with the
128 historical seismicity record and previous paleoseismological data shows that this approach is
129 not sensitive enough to detect the smaller events (Mw 6.8-7) that are also known to occur
130 along the MNAF. We finally explore the implications of several plausible scenarios to help
131 explain past slip history at the scale of the NAF system east of the Marmara Sea.

132

133 **2 Geological context: the NAF in the Marmara region**

134 The formation of the NAF initiated some 11-13 Ma ago within a wider pre-existing shear
135 zone which progressively localized through time (Sengör et al., 2014). From the Messinian
136 and during the Pliocene, the NAF has functioned as a narrow zone, cutting through and
137 deforming several basins inherited from the previous tectonic stages (Barka, 1992; Yılmaz et
138 al., 1995). While the deformation is localized in a narrow zone in the eastern and central part
139 of the NAF, it is structured on a wider area west of Düzce with a distribution of the
140 deformation across three main strands (Armijo et al., 1999; Fig. 1). The NAF strands show
141 oblique kinematics, with local complex partitioning of the deformation between dextral strike-
142 slip and extensional regimes (Koçyigit & Özacar, 2003). The northern strand (NNAF)

143 continues along the strike of the main fault zone and crosses the northern part of the Marmara
144 Sea from the Gulf of Izmit to Gelibolu Peninsula (Fig. 1). The middle strand (MNAF)
145 branches off from the NNAF in Akyazi district, bounds to the south two successive basins
146 known as the Geyve-Pamukova Basin and Iznik Lake, reaches the Marmara Sea through the
147 Gulf of Gemlik and borders the southern shore of Marmara (Fig. 3a). The southern strand
148 (SNAF) separates from the MNAF near Iznik and continues southwestwards to Ulubat and
149 Manyas Lakes (Fig. 1b).

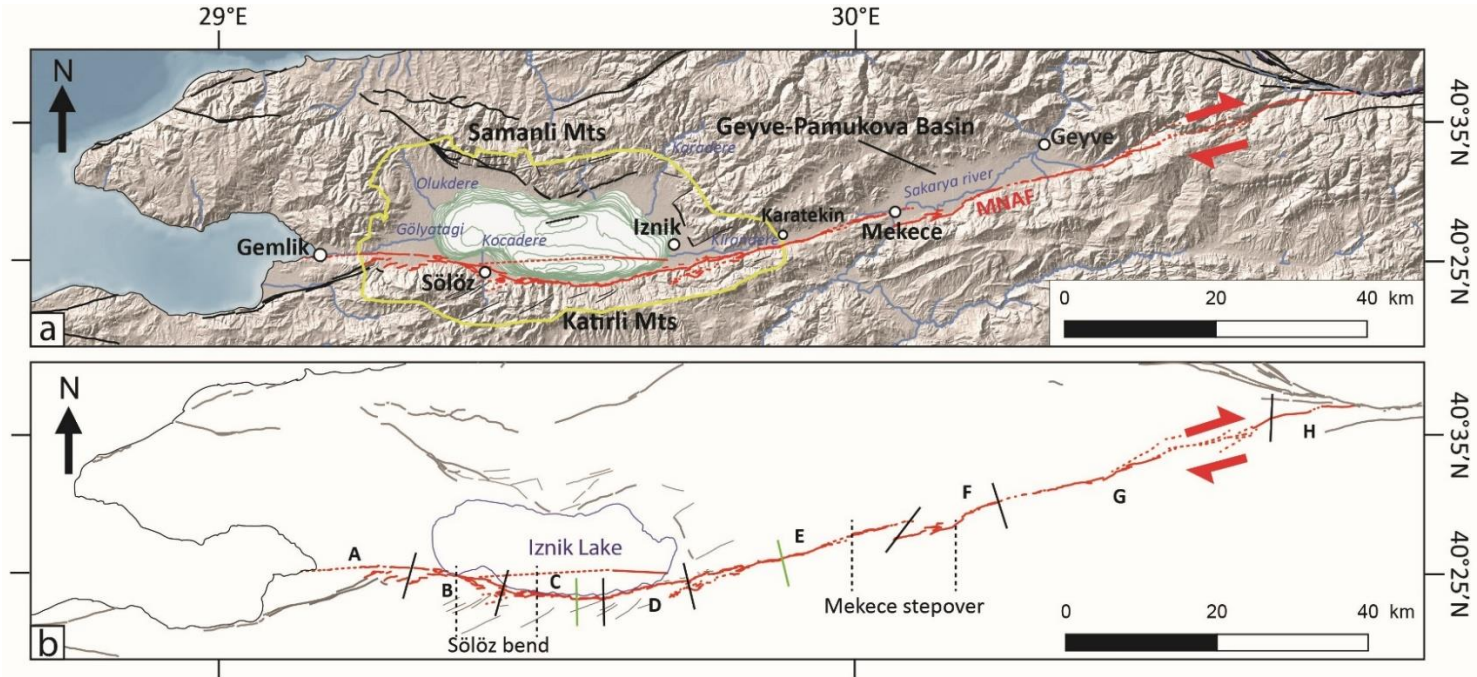
150 The MNAF has been traditionally divided into three major sections over a total length of 135
151 km (Fig. 3). (1) Between the Gulf of Gemlik and Iznik Lake, the fault shows a roughly E-W
152 direction, until a 12 km long releasing bend around Sölöz delta, southwest of the Lake. (2)
153 The fault follows the southern coast of Iznik Lake with an E-W orientation, and continues in
154 the narrow valley of the Kirandere with a constant azimuth of $\sim 80^\circ$. This section in the west
155 of Iznik Lake is marked by greater structural complexity and distribution of the deformation
156 across several overlapping faults. Öztürk et al. (2009) suggested the existence of a continuous
157 strike-slip fault extending along the deepest area of Iznik Lake, while Gastineau et al. (2021)
158 evidenced an active fault strand following the northeastern edge of the lake's southern sub-
159 basin (Fig. 3b). East of Iznik Lake, Sipahioğlu and Matsuda (1986) reported the presence of
160 two lineaments in this section: a geological boundary fault with no marker of Quaternary
161 activation, and an active fault strand crosscutting and deforming recent alluvium. The eastern
162 end of this section around the town of Mekece consists in a narrow, 1 km wide releasing step-
163 over. (3) East of the step-over, the MNAF borders the south of the Geyve-Pamukova basin
164 with a $70\text{-}80^\circ\text{N}$ strike. The fault is associated to another fluvial system with the Sakarya
165 River, collecting waters from the Anatolian plateau to the Black Sea. The river itself presents
166 a large-scale right-lateral offset across the fault, estimated around 15-20 km (Koçyigit, 1988;
167 Özalp et al., 2013). The eastern edge of the basin is marked by a short restraining bend, after

168 which the fault continues with a similar strike in the mountainous area of Akyazi where it
169 connects to the main NAF.

170

171 **3 Previous slip-rates and paleoseismological studies on the MNAF**

172 The most recent estimation of the long-term horizontal slip rate on the MNAF was obtained
173 by Gasperini et al. (2011) who used the displaced edge of a 11,250 years old submerged delta
174 in Gemlik Bay to derive a 3.7 ± 0.7 mm/yr minimal rate (Fig. 1b). This rate is comparable with
175 the rates of $\sim 5\pm 2$ mm/yr derived from strain accumulation modeling of fault-perpendicular
176 GPS measurement profiles (Ergintav et al., 2014; Straub et al., 1997). Another value of
177 4.9 ± 0.4 mm/yr was derived from the 16 ± 1 km long offset of the Sakarya river in the
178 Pamukova plain since the Late Pliocene (Özalp et al., 2013). The vertical motion was
179 documented by Ikeda et al. (1991) who estimated a 0.7-1.4 mm/yr minimal rate from tilted
180 post-glacial beachridges located on the western shore of Iznik Lake.



181

182 **Figure 3.** (a) General morphology of the eastern MNAF region. The footprint of the orthorectified Pleiades images (yellow) is
 183 superimposed on the Shuttle Radar Topography Mission (SRTM) model. The main rivers are drawn in blue. The MNAF is
 184 represented in red and the other active faults in black. Dotted lines indicate low confidence fault mapping (see section 4.2). The
 185 contours on the Iznik lake bottom are at a 5-meter interval (see Data Availability section). The fault traces within Iznik Lake are taken
 186 from Gastineau et al. (2021). (b) Segmentation of the main fault section analyzed in this study. Determined intersegments are located
 187 with black lines and alternative intersegments C/D et D/E with green lines (see section 4.3). Söloz and Mekece step-overs' extent is
 188 shown with dashed lines.

189 A significant number of paleoseismological trenches have been dug along the MNAF (Akyuz &
190 Zabcı, 2012; Fraser et al., 2010) that led to the identification of several ruptures during the last
191 4000 years (Fig. 2c). Yoshioka and Kusçu (1994) studied a site near Geyve and identified a 3rd
192 century BC rupture and a later undated one. In the same area, an unpublished trenching work by
193 Akyüz et al. (2014) led to the identification of three presumed earthquakes. In the east of Iznik,
194 the last rupture was dated between the 13-14th and 18th centuries CE (Honkura & Isikara, 1991;
195 Ikeda, 1988). On the same segment, Barka (1993) opened nine trenches and found three ruptures
196 since ~2000 BC, but none of them were dated precisely. In the eastern part of Iznik Lake,
197 Gastineau et al. (2021) evidenced a historical event in sediment cores, that they correlated to the
198 1065 CE earthquake. South of the lake, Erginal et al. (2021) reported a 50 cm high coseismic
199 scarplet in beachrock deposits that they attributed to an 8th century rupture. On the same
200 segment, Civico et al. (2021) opened two trenches and evidenced one mid-19th century event,
201 one penultimate event after the late 7th century and two older events before the mid-5th century
202 CE. West of Iznik Lake, Ikeda et al. (1989) proposed a mid-19th century event from
203 archaeological remains found in a natural fault exposure. In Gemlik, Özalp et al. (2013) found a
204 similar age for the last event and dated the penultimate between the 12th and 18th centuries. So
205 far, the largest trenching work has been conducted by Dogan (2010) who opened 11 trenches on
206 various MNAF segments. In many cases, very few or no age data could be retrieved, which
207 makes it difficult to discuss whether the identified ruptures are independent from each other.
208 Thus, in terms of earthquake recurrence, the paleoseismological data along the MNAF remain
209 largely inconclusive due to partial results or occasionally contradictory findings (Fig. 2c).

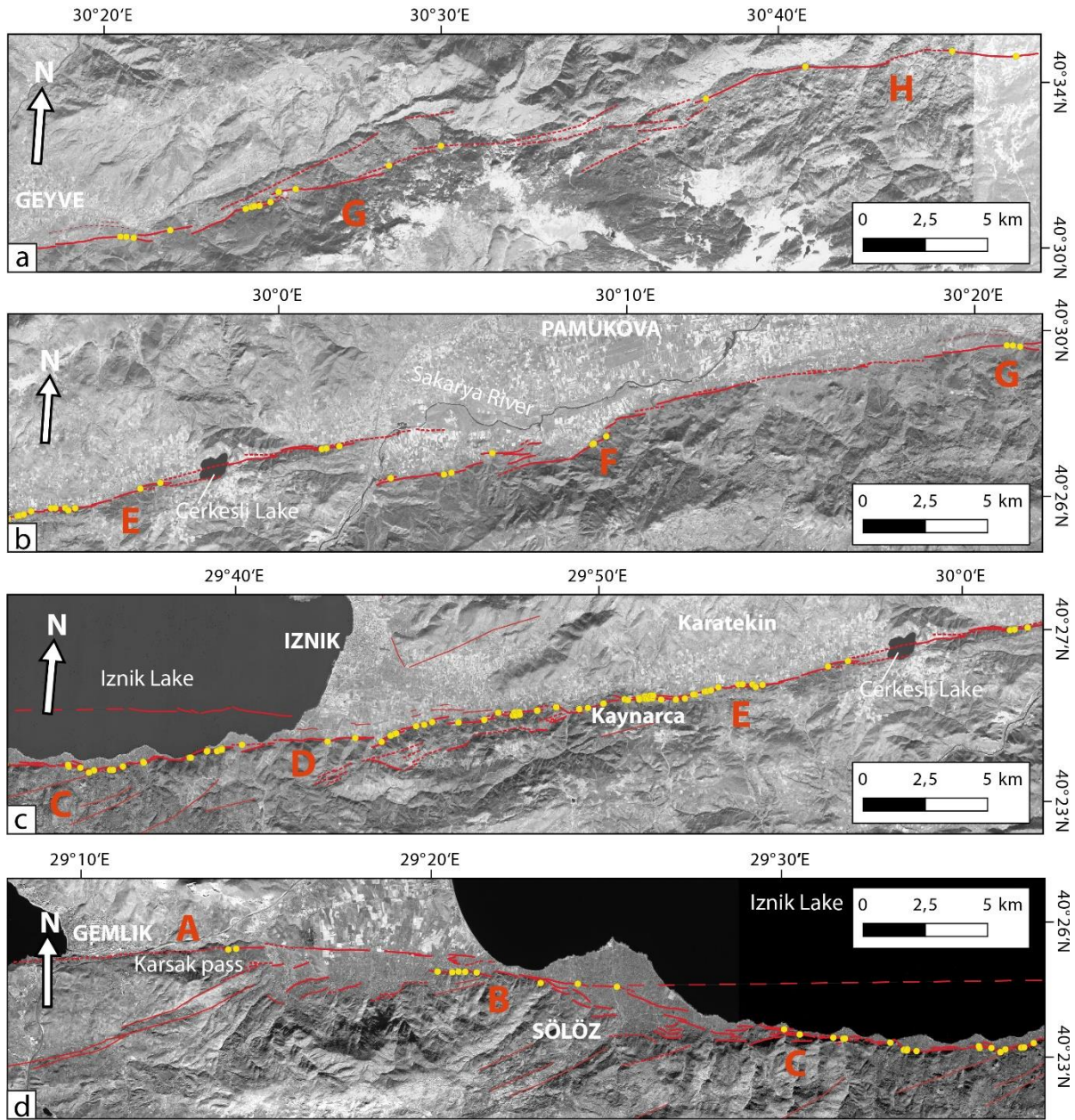
211 **4 Fault geometry and segmentation analysis**

212 **4.1 Imagery datasets used**

213 Four stereo-pairs of Pleiades images covering the area between the Gulf of Gemlik, Iznik Lake,
214 and Karatekin (Fig. 3a) were processed to obtain a high-resolution DEM using the NASA Ames
215 Stereo Pipeline (ASP) software (Broxton and Edwards, 2008; Moratto et al., 2010; Shean et al.,
216 2016) without using ground control points (Fig. 4c,d). The original Pleiades images have a
217 resolution of about 50 cm, while the derived DEM has a horizontal resolution of 2 m and an
218 absolute vertical precision better than 10 m. The DEM was then used to orthorectify the original
219 optical images with the same ASP software. For the area east of 29.88E, which was not covered
220 by our Pleiades images, we relied on Google Earth images (Pleiades images from CNES/Airbus,
221 and QuickBird and WorldView images from Maxar Technologies), the SRTM elevation model
222 and the active fault map of Emre et al. (2011).

223 **4.2 Fault mapping and along-strike geomorphology**

224 The trace of the MNAF between Karsak pass and Akyazi was mapped using the satellite imagery
225 described in the previous section and complementary observations gathered in the field (Fig. 2a,
226 4). In the area benefiting from Pleiades coverage, secondary faults north and east of Iznik Lake
227 were also mapped (Fig. 3). To draw the fault trace, we especially relied on high confidence
228 geomorphological features, such as series of horizontally offset gullies and ridges, shutter ridges,
229 well-defined scarps and facets. Along some other sections, particularly those lacking multiple
230 consistent offsets, the mapping relied on lower confidence features, including large scale
231 lineaments and slope breaks (Fig. 4).



232

233 **Figure 4.** Surface trace of the eastern MNAF, superimposed on the Pleiades orthorectified
 234 images around Iznik Lake and Sentinel 2 images (Copernicus Sentinel Data [2018]) in other
 235 areas. Solid thick, dotted, and thin lines refer to high confidence, low confidence, and secondary
 236 fault mapping, respectively. The subaqueous fault trace is taken from Gastineau et al. (2021).
 237 The yellow dots locate the markers associated with the offsets measured. The areas (a to d) are
 238 presented from east to west. Our proposed segmentation (A to H) is also displayed.

239 Evidence for late Quaternary deformation can be observed in the landscape along the MNAF
240 segments between the Gulf of Gemlik and Akyazi district (Fig. 2a, 3, 4). East of the Gulf of
241 Gemlik, a small, E-W trending fault scarp borders the south of Gemlik alluvial plain and runs
242 along the narrow Karsak pass (Fig. 4d). East of Karsak pass, several parallel faults stretch
243 between the Eocene sedimentary rocks of the mountain range and the derived wide alluvial fan
244 south of the Gölyatagi stream (Fig. 3a, 4d). Southwest of Iznik Lake, a set of overlapping and en
245 echelon fault scarps are visible between the basement rocks and the Holocene alluvium of the
246 large Sölöz delta, striking WNW-ESE. However, the horizontally offset markers are found along
247 an E-W fault strand crossing the delta. This fault appears in the westward continuation of the
248 fault scarp evidenced in the lake close to Iznik (Gastineau et al., 2021), and forms a releasing
249 step-over with the fault section running south of the lake.

250 East of the delta, the fault shows again an E-W orientation with a succession of short, en echelon,
251 recent scarps in the narrow coastal plain south of the lake (Fig. 4c, d). The association of several
252 laterally offset gullies and vertical, south-facing scarplets (Fig. S1 and S2c) evidences the recent
253 dextral motion across the fault with a normal component. A series of significant triangular facets
254 have developed in the same section along the north-facing side of the Katirli range, which
255 suggests long-term cumulative normal deformation in addition to the strike-slip tectonics.

256 Southeast of the lake, the fault becomes more oblique to the main NAF direction, striking 80-
257 85°N (Fig. 4c). East of Iznik Lake, the fault follows the southern edge of a 15 km long narrow,
258 linear valley with a quasi-single, straight and more continuous trace (Fig. 4c). Between Iznik and
259 Kaynarca, large-scale lineaments mark an oblique branch extending south of the main fault zone
260 and striking N070. On the main fault line, markers of strike-slip deformation, such as shutter
261 ridges, offset drainages and alluvial fan surfaces, are well developed (Fig. S2b). Occasionally,

262 parallel or en echelon successive faults can be traced in the landscape. This is the case between
263 Kaynarca and Karatekin where secondary branching can be traced through a series of fan
264 surfaces showing several offsets (Fig. 4c). This geometrical complexity is associated with an
265 orientation change to N080. Close to Mekece, a series of laterally displaced streams running
266 along a north facing scarp show cumulative dextral offsets ranging between 10 m and 25 m.

267 Further east, the fault crosses the Sakarya river and forms a ~1 km wide releasing step-over (Fig.
268 4b). The eastern section of the stepover is composed of shorter, en echelon faults. The fault then
269 follows the southern edge of the Geyve-Pamukova basin as a single, simple straight trace with a
270 70-80°N, but is associated with fewer markers of Holocene horizontal deformation. East of the
271 Geyve plain, the fault runs in the middle of a mountainous area and the precise mapping of the
272 junction with the main NAF strand is less certain (Fig. 4a).

273

274 **4.3 Fault segmentation**

275 To properly interpret the set of deformed markers observed along the fault, it is needed to first
276 determine the fault segmentation. Such segmentation can also provide first-order constraints on
277 the maximum length and magnitude of earthquake that can be expected. The kind of boundary
278 between the successive segments (azimuth difference, width and length of the step-overs. . .) is
279 also thought to control whether a given rupture is likely to propagate through several segments
280 (Aki, 1984; Barka & Kadinsky-Cade, 1988; Wesnousky, 2006). We decomposed the eastern
281 MNAF zone into several successive segments using the automatic procedure developed by
282 Klinger (2010). The digitized MNAF trace was first simplified and resampled each 50 m. The
283 numerical method models the fault as a continuous set of linear segments and seeks, for a given

284 number of segments, the distributions of segment boundaries which best approximate the actual
285 fault trace. We especially explored the solutions for the range between 8 and 19 segments which
286 showed a good trade-off between data-model misfit and limited number of segments (Fig. S3).
287 The locations of most frequently selected inter-segments for this range cluster on 12 points of the
288 fault. Keeping the solutions that included the most visible geometrical discontinuities along
289 strike (e.g. Sölöz and Mekece stepovers, kinks at 29°35'E and south of Iznik) led us to favor a
290 decomposition of the MNAF into 8 segments (denoted A to H on Fig. 3b).

291 Overall, the boundaries most frequently selected correspond to the major strike change occurring
292 south of Iznik Lake (C/D inter-segment, Fig. 3b) and the releasing bend at the eastern edge of the
293 Geyve-Pamukova basin (G-H inter-segment). The significant discontinuities of Sölöz bend (B/C
294 inter-segment) and Mekece stepover (E/F inter-segment) also correspond to recurrently selected
295 boundaries. Some other chosen boundaries are less recurrent. The D/E inter-segment is
296 associated with a minor variation in azimuth but also with a more visible change from multiple
297 parallel branches to a single, simpler fault trace eastward. The F/G inter-segment also reflects a
298 transition from small en echelon faults to a single linear fault line eastward.

299

300 **5 Cumulative and coseismic offsets**

301 **5.1 Method of measurement and uncertainties**

302 Major ground rupturing earthquakes generate meter-scale deformations that can be preserved in
303 the morphology through several seismic cycles (e. g. Ansberque et al., 2016; Klinger et al., 2011;
304 Kurtz et al., 2018). In the case of strike-slip ruptures, it is generally possible to measure in the

305 days following the earthquake a series of laterally displaced markers such as roads, fences, walls,
306 field or vegetation lines, terrace risers or gullies. Older morphological markers can also show
307 larger, cumulative values of offset representing the summation of several coseismic
308 displacements. If enough markers of various ages are preserved along the fault, the compilation
309 of a large number of offset measurements is expected to give several clusters of values,
310 corresponding to the cumulative displacement for various numbers of earthquakes (Beauprêtre et
311 al., 2012, 2013). The offset measurements carried out after recent earthquakes have evidenced
312 that the coseismic slip located on the fault often shows significant variations along-strike, as high
313 as 30-40% around the mean displacement (Choi et al., 2018; Lin et al., 2020; Reitman et al.,
314 2019; Rockwell et al., 2002; Zielke, 2018). Despite the erosive and sedimentary processes which
315 tend to erase the smallest coseismic offsets, the measurement of cumulative offsets can also give
316 access to this slip variability on longer time scales (Rizza et al., 2011).

317

	Total	Segment A	Segment B	Segment C	Segment D	Segment E	Segment F	Segment G	Segment H
Length (full mapping, km)	148	14.4	12.5	13.9	11.5	31.2	16.4	36.6	11.5
Length (confident mapping, km)	107	4.1	12.5	13.6	11.1	24.1	14.9	17.3	9.2
Number of measurements	114	2	10	14	15	50	7	12	4
Measured on Pleiades topography	45	1	6	8	8	22	0	0	0
% Pleiades topography	39	50	60	57	53	44	0	0	0
Measured on Pleiades image	32	1	4	6	7	14	0	0	0
% Pleiades image	28	50	40	43	47	28	0	0	0
Measured on Google Earth image	37	0	0	0	0	14	7	12	4
% Google Earth image	32	0	0	0	0	28	100	100	100
Mean quality /20	12	14	12	11.1	12.3	12.3	10.7	11.8	12.3
Density of data per km	0.77	0.14	0.80	1.01	1.30	1.60	0.43	0.33	0.35
Density of data (confident mapping)	1.07	0.49	0.80	1.03	1.35	2.07	0.47	0.69	0.43
Number of COPD peaks (2σ model)			5	7	11	8	4	6	
Number of COPD peaks (1σ model)			4	4	5	8	4	4	2

318

319 **Table 1.** Summary of the main characteristics of the fault mapping and offset measurements datasets used in this study.

320

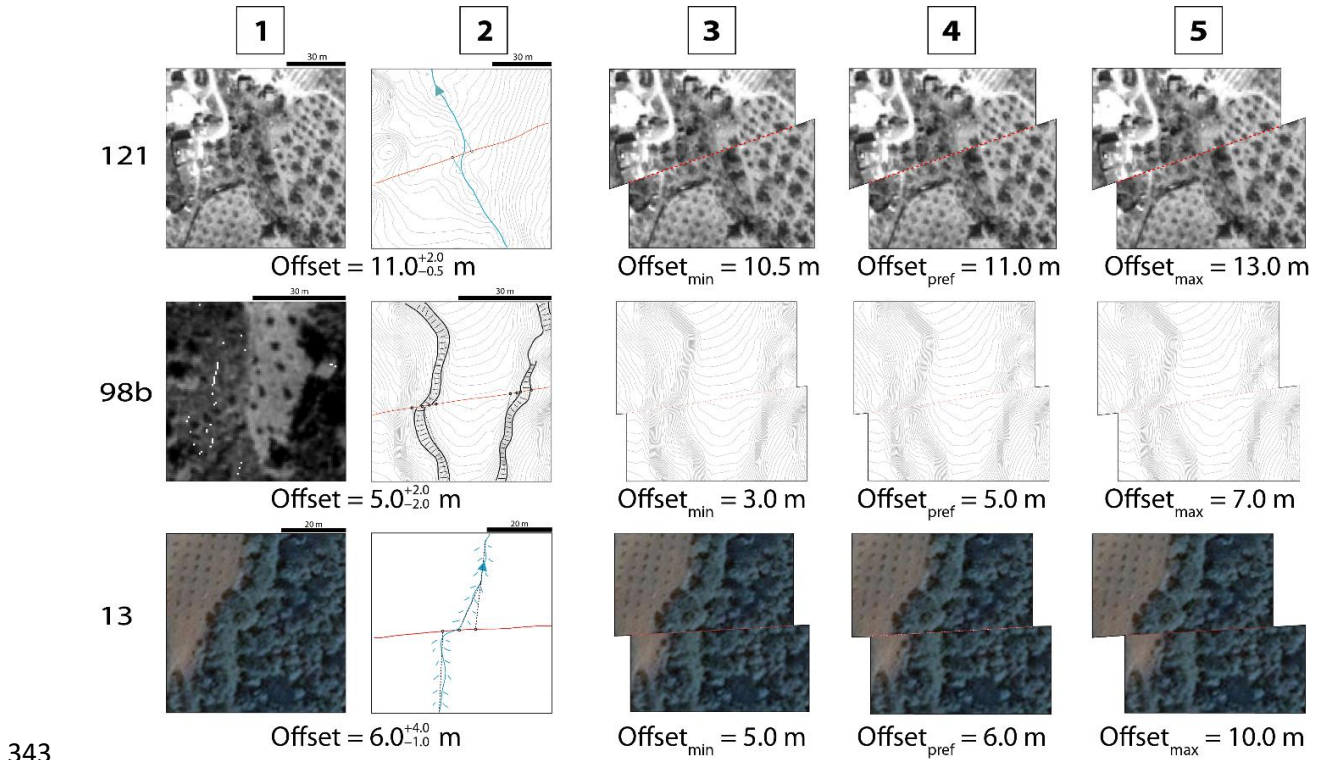
321

322 Along a 148-km long portion of the eastern MNAF, we identified and systematically
323 measured 114 offsets (Tables 1 and S3, see Data Availability section). 40% of the
324 measurements were performed using Pleiades topographic data, while Pleiades ortho-rectified
325 images and Google Earth images each represent 30% of the measurements. The displaced
326 markers considered are river channels, gullies, terrace risers and more occasionally vegetation
327 lines and ridges. We favored markers making a high angle with the fault in order to minimize
328 the apparent offset linked to unaccounted-for vertical slip. For each marker, we define
329 piercing lines, i.e. points that were aligned before the displacement, and that we project on the
330 fault trace. The piercing points across the fault are then realigned by retro-deformation, which
331 gives the offset value (Fig. 5). When one marker is displaced by several parallel fault strands,
332 the offset value to be considered is the sum of the measurements on each fault line (Zielke et
333 al., 2015). Five offsets were also measured in the field with tape (Fig. 6). One field
334 measurement (marker 153) ranges significantly lower than the Pleiades measurement due to
335 different reconstruction hypothesis. The other field measurements are in general in fair
336 agreement with the values obtained from satellite imagery, though ~10% lower on average.
337 The relative underestimation of field offset measurements compared to satellite imagery has
338 been noticed in previous studies (see another example in Klinger et al., 2005) suggesting that
339 the distributed deformation is better assessed in the latter case.

340

341

342



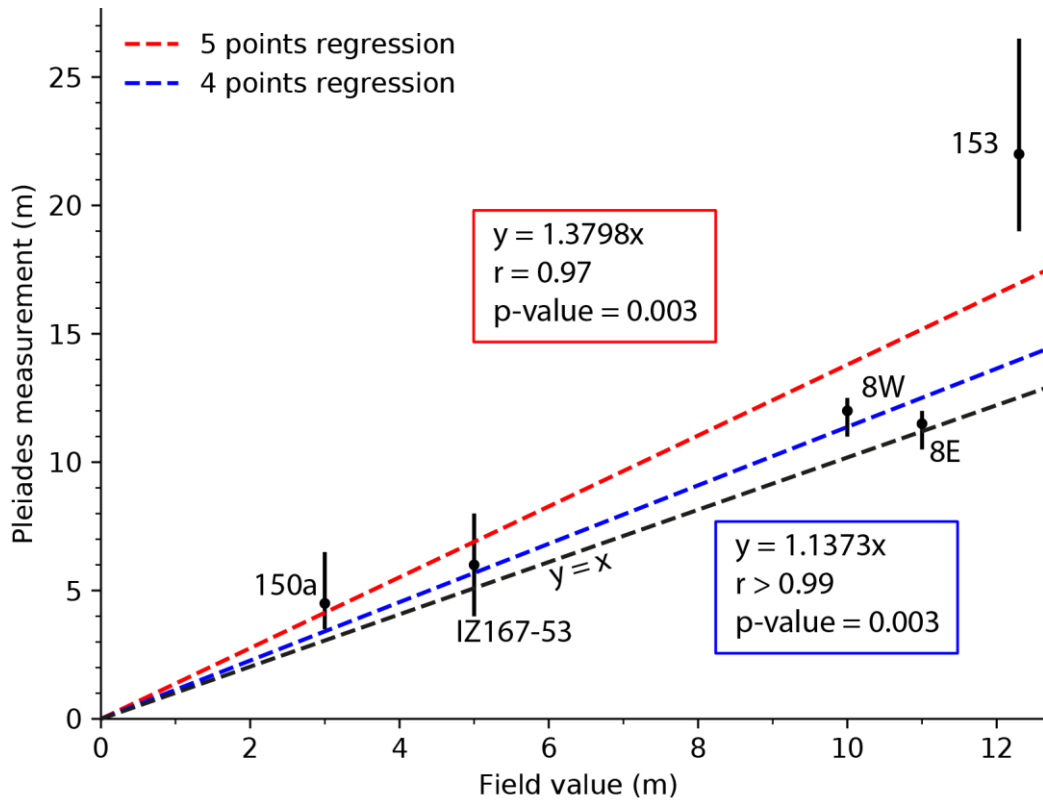
343

344 **Figure 5.** Examples of horizontal offset measurements. Marker ID code is indicated on the
 345 left. North direction is upward. From top to bottom, measurements were respectively done
 346 using the Pleiades image, topography, and the Google Earth image. Columns 1 and 2 show
 347 the original morphologies. The fault is drawn in red. Black lines and circles refer to the
 348 piercing lines and points. Columns 3, 4 and 5 show the retro-deformed morphologies giving
 349 the minimum, preferred and maximum offset values respectively. For the full dataset, see
 350 Data Availability section.

351

352

353



354

355 **Figure 6.** Comparison between field and Pleiades offset measurements. Two linear
 356 regressions are shown, including all data points (red) and excluding marker 153 (blue). For
 357 each regression we present the equation, Pearson's correlation coefficient r and the p-value.

358

359 The uncertainty of the offset measurement mainly originates from the various possibilities for
 360 interpreting and restoring the original, non-deformed geometry of the marker (Ansberque et
 361 al., 2016; Manighetti et al., 2015). Therefore, each measurement consists in our preferred
 362 value for the best reconstruction, and a minimum and a maximum value, each representing an
 363 extreme plausible reconstruction. We use conservative min/max reconstructions, larger than
 364 $\pm 15\%$ of the preferred value on average, so that there is only a small probability that the real
 365 offset falls out of this range (Gold et al., 2013). Each measurement is given a 20-points
 366 quality score, which reflects the intrinsic quality of each marker in providing a relevant
 367 measure (Beauprêtre et al., 2013; Choi et al., 2018; Kurtz et al., 2018; Zielke et al., 2012).

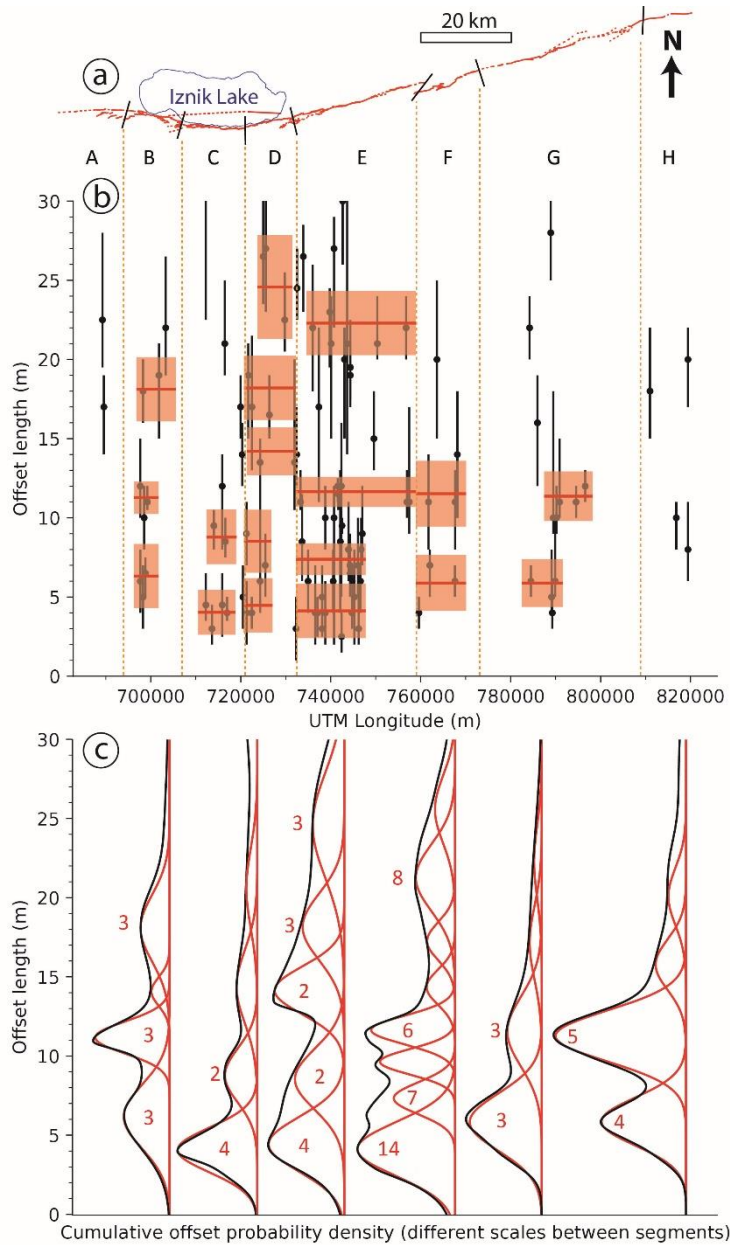
368 This score includes the following criteria: (a) confidence that the offset marker is of tectonic
369 nature and weakly man-modified, (b) degree of preservation (marker visibility and sharpness),
370 (c) marker shape (width and sinuosity), (d) fault zone complexity (plausible fault zone width
371 and number of fault splays), (e) angle of marker with fault, (f) resolution of used dataset (a
372 detailed explanation of how the quality score is determined can be found in Supporting
373 Information).

374 **5.2 Statistical analysis**

375 The 114 offsets measured range between 2.5 and 64 m, with a majority of values smaller than
376 30 m (Fig. 7b, Table S3). In order to identify the most significant offset clusters along each
377 fault segment, which could represent the cumulative signature of past ruptures, we represent
378 the offset values as probability density functions (e.g. Beauprêtre et al., 2012; Kurtz et al.,
379 2018; McGill and Sieh, 1991; Zielke et al., 2010). Each offset measurement is represented
380 with an asymmetric Gaussian distribution, the preferred measured value being the peak of the
381 Gaussian probability density function (PDF). Since the minimum and maximum offsets
382 reflect geologically plausible bounds for the reconstruction values and do not directly
383 correspond to real standard variations (Scharer et al., 2014), we compare two models where
384 these maximum and minimum ranges are taken as $\pm 1\sigma$ and $\pm 2\sigma$ half-widths of the PDF
385 (referred hereafter as “ 1σ model” and “ 2σ model”).

386

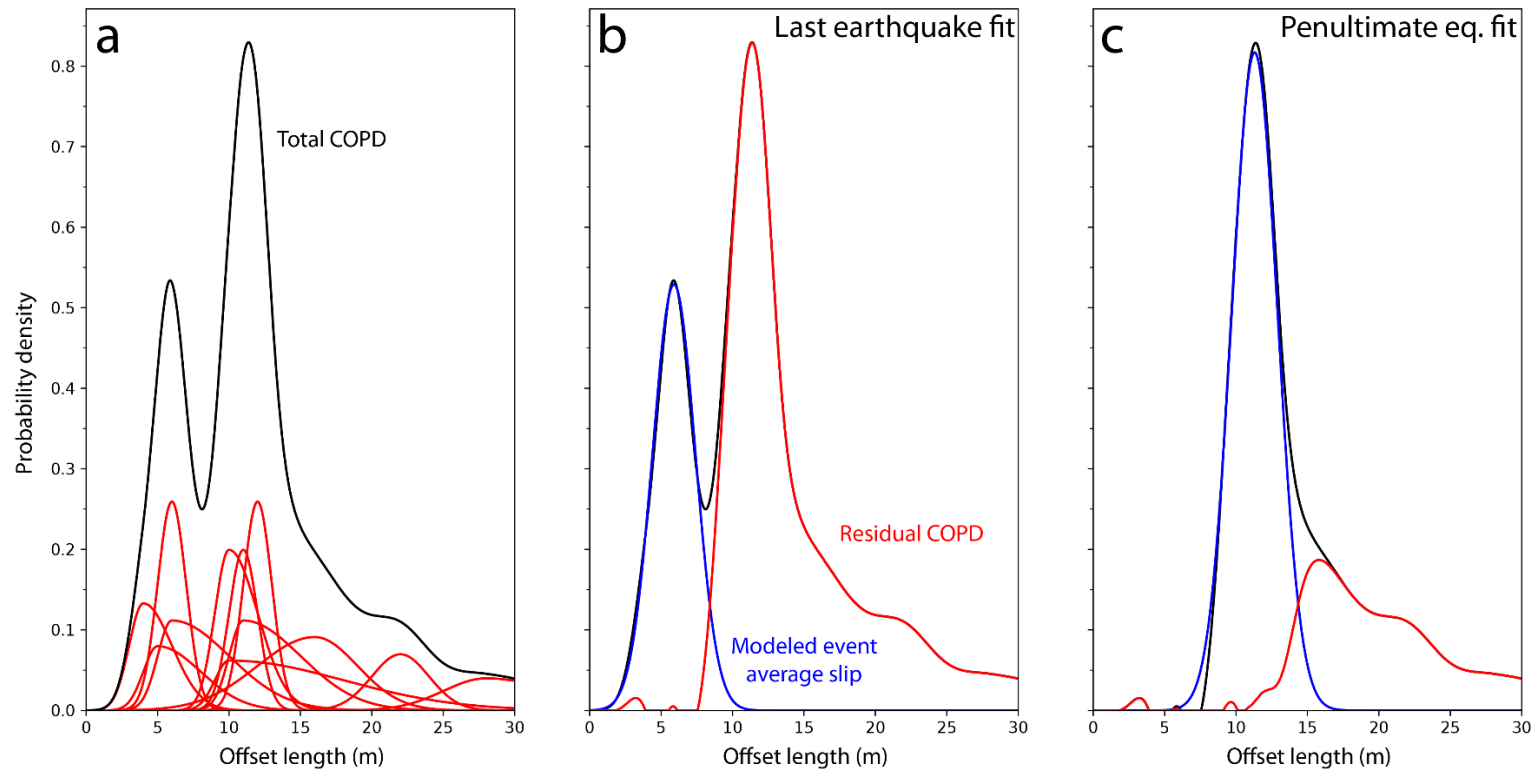
387



388

389 **Figure 7.** (a) Map of the fault section studied with our proposed segmentation. (b) Horizontal
 390 offsets measured along the fault in the range 0-30 m. The color boxes represent the best
 391 constrained peak values, within 1σ uncertainties, obtained on the cumulative offset probability
 392 distribution (COPD) curves for each segment. The segments are separated by the vertical
 393 orange broken lines. (c) COPD curves (black lines) and modeled average slips (red lines) for
 394 the 1σ model. The number of supporting individual measurements is indicated for the best
 395 constrained COPD peaks.

396 The individual PDFs for each segment are then summed into a cumulative offset probability
397 distribution (COPD) curve, using the quality scores as weights for each individual offset
398 measurement (Fig. 7c and 8a). The COPD generally presents local peak values, which indicate
399 the most frequent offsets measured along the fault section considered. The contribution of each
400 measurement in the shape of the COPD depends both on its uncertainty and on its quality score.
401 A larger uncertainty corresponds to a wider and flatter individual PDF, which consequently
402 contributes less to define a clear COPD peak. A lower quality score decreases the effect of the
403 measurement in changing the shape of the COPD. For each COPD curve, it is assumed that the
404 value associated to the first peak value corresponds to the offset related to the most recent large
405 earthquake preserved along that specific segment. The average slip associated with this last
406 rupture is empirically extracted from the COPD through several steps (Kurtz et al., 2018). (1)
407 The rising part of the COPD curve is used to build a symmetric Gaussian function, which
408 represents the modeled average slip associated to the most recent rupture along the segment
409 considered. (2) This modeled function is subtracted from the COPD to derive a residual COPD
410 (Fig. 8b). This residual curve is assumed to represent the cumulative tectonic deformation
411 recorded in the landscape before the most recent earthquake occurred. (3) In general, the rising
412 part of the COPD does not strictly follow a Gaussian function, which produces a residual
413 negative artefact located ahead of the following peak values. This residual is discarded by
414 resetting all negative values to zero before the next extraction. These steps are iterated (Fig. 8c)
415 until the residual COPD curve becomes too flat to constrain another Gaussian fit. The minimum
416 amplitude threshold for a peak to be extracted is fixed at 10% of the maximum amplitude of the
417 original COPD.



418

419 **Figure 8.** Illustration of the statistical analysis methodology used for the offset measurements of segment G. (a) Probability density functions of
 420 the individual measurements (in red) and corresponding Cumulative Offset Probability Density (COPD, in black). (b) Modeling of the last major
 421 surface rupture signal by fitting the increasing part of the COPD with a Gaussian curve (in blue). The red line is the residue of the COPD after
 422 subtracting this last rupture slip model. (c) Same process as (b) for the presumed penultimate event.

423 Interpreting COPD peaks as individual slip signals must be done with caution, especially when
424 relative measurement uncertainties are high and when only few data points are available along a
425 segment. Because of the natural variability in coseismic slip along strike, offset measurements
426 from a single event can produce bimodal distributions (Lin et al., 2020; McGill & Rubin, 1999).
427 Conversely, one large increment might hide two separate, smaller events, but undistinguished
428 due to too few data and/or too large individual uncertainties (e. g. Liu-Zeng et al., 2006; Zielke et
429 al., 2010). Once the COPD peaks are extracted for a given segment, we assess the statistical
430 significance of each peak by looking at the following criteria (Tables 2 and 3): number of
431 supporting individual measurements, spreading of the data supporting the first two peaks, degree
432 of overlapping with preceding peak, sensitivity to alternative segmentation (for segments C, D,
433 E).

434

435 **5.3 Results**

436 Tables 2 and 3 present the offset values extracted from the COPD peaks for each fault segment
437 in the range 0-30 m. We extracted between 4 and 11 peaks per segment for the 2σ model and
438 between 4 and 8 peaks for the 1σ model (Table 1). Smaller modeled uncertainties tend to
439 increase the number of extracted peaks per segment. This effect is most significant for segment
440 D where the number of peaks for the 2σ model is two times larger. However, most of the
441 extracted peaks for the 2σ model show poor statistical robustness. Half of them are not supported
442 by more than one individual measurement (Table 3). For some of them, the increment with the
443 preceding peak is not significantly different from zero. Several of them do not pass the
444 segmentation test. This likely results from a high degree of data scattering compared to

445 uncertainties, especially for segments with small numbers of measurements. Segment E does not
446 show this feature because of its high spatial density of measurements, which is more than twice
447 as high as the average density of the other segments (Table 1).

448 To check for potential biases resulting from this higher density of measurements, we performed a
449 supplementary test on segment E. We produced and analyzed five random subsets of 18
450 measurements obtained on segment E, so that the measurement density of the subsets equals the
451 average density of the other segments, i.e. 0.75 measurement per km. We then identified which
452 extracted peaks remained consistent between all subsets. The sensitivity tests for that segment
453 suggest that only the first two peaks are statistically robust. These peaks still present a high
454 degree of overlapping.

455 Most peaks obtained with the 1σ model are statistically stronger than those obtained with the 2σ
456 model (Table 2). When only the more robust peaks are considered, both models show similar
457 results (Table 4, Fig. 7b). Segments A and H did not provide statistically significant peaks due to
458 the very small number of measurements.

459 We identified two to five statistically robust cumulative slip increments for segments B to G,
460 ranging between 4 and 25 m. Offset values show consistency between all segments for the first
461 two extracted peaks at ~ 5 and ~ 10 m. However, the central segments C, D and E show lower
462 mean values of increments, from 3.2 m to 4.7 m, while they range between 5 and 6.2 m on
463 segments B, F and G. On segment E, despite the higher density of measurements, the events are
464 harder to separate and their respective displacement is less constrained due to the larger
465 scattering of data points. Peak values differ more for higher peaks (Table 4).

Segment	Mean value	($\pm 1\sigma$)	Increment with preceding peak	($\pm 1\sigma$)	Number of supporting measurements	Mean quality	Spreading with previous peak	Overlapping coefficient with previous peak	Sensitivity to segmentation	Sensitivity to downsampling
B	6.2	2			3	12.7				
B	11.2	1	5	3	3	12	<30%	0.09		
B	14.1	0.9	2.9	1.9	0			0.13		
B	18.1	2.1	4	3	3	12		0.16		
C	4.1	1.4			4	14.3				
C	8.8	1.7	4.7	3.1	2	11	<30%	0.13		
C	14.4	2.3	5.6	4	3	9		0.16	x	
C	20.6	2.5	6.2	4.8	1	11		0.2		
D	4.5	1.7			4	12.3				
D	8.6	1.9	4.1	3.6	2	10	<30%	0.25		
D	14.2	1.5	5.6	3.4	2	14.5		0.1		
D	18.2	2.1	4	3.6	3	14		0.26		
D	24.6	3.3	6.4	5.4	3	11.3		0.23		
E	4.2	1.7			14	12.8				
E	7.4	1	3.2	2.7	7	12.1	<30%	0.23		
E	9.7	0.8	2.3	1.8	4	10.8		0.2		x
E	11.7	0.9	2	1.7	6	13.3		0.24		
E	14.4	1.1	2.7	2	2	11		0.18		x
E	17.3	1.2	2.9	2.3	2	13		0.21	x	x
E	21.3	2.1	4	3.3	8	11.6		0.21		
E	25.6	2.1	4.3	4.2	3	13.7		0.31	x	x
F	5.9	1.8			3	10.7				
F	11.6	2.2	5.7	4	3	10	<30%	0.15		
F	17.2	2.3	5.6	4.5	0			0.21		
F	22.3	2.3	5.1	4.6	1	13		0.27		
G	5.9	1.5			4	11.3				

G	11.3	1.6	5.4	3.1	5	13.2	<30%	0.08
G	15.8	1.6	4.5	3.2	1	16		0.16
G	20.1	1.8	4.3	3.4	1	7		0.21
H	9.4	2			2	13		
H	18.7	2.7	9.3	4.7	2	11.5	30-40%	0.05

466 **Table 2.** COPD peaks extracted for the 1σ model. Mean quality is computed on the set of individual measurements supporting each
467 peak. Spreading value is expressed in % of the mean of measurements supporting the first two peaks per segment. The overlapping
468 coefficient is computed using normalized distributions.

Segment	Mean value	Increment with ($\pm 1\sigma$) preceding peak	Number of supporting measurements	Mean quality	Spreading with previous peak	Overlapping coefficient with previous peak	Sensitivity to segmentation	Sensitivity to downsampling	
B	6.1	1.3	3	12.7					
B	9.9	0.6	3.8	1.9	1	13	<30%	0.04	
B	11.1	0.4	1.2	1	1	15		0.22	
B	12.3	0.9	1.2	1.3	1	8		0.32	
B	18.2	1.4	5.9	2.3	2	13.5		0.01	
C	3	0.5			1	17			
C	4.2	0.5	1.2	1	3	13.3	>40%	0.23	
C	5.4	0.5	1.2	1	0			0.23	
C	9	0.8	3.6	1.3	3	10	<30%	0.05	
C	13.9	1.6	4.9	2.4	1	11		0.04	x
C	17.2	0.7	3.3	2.3	1	8		0.14	x
C	21.2	1.6	4	2.3	1	11		0.07	
D	4.2	0.8			3	14			
D	6.8	1	2.6	1.8	2	6.5	30-40%	0.15	

D	9	1	2.2	2	1	14	<30%	0.27		
D	13.2	1.9	4.2	2.9	0			0.14	x	
D	13.7	0.5	0.5	2.4	2	14.5		0.42		
D	14.9	0.5	1.2	1	0			0.23		
D	16.6	0.7	1.7	1.2	2	15		0.15		
D	18.2	0.9	1.6	1.6	1	12		0.31	x	
D	19.8	0.6	1.6	1.5	1	12		0.26		
D	22.5	1.2	2.7	1.8	1	14		0.16	x	
D	26.5	1.7	4	2.9	2	10		0.16		
E	3.8	1			10	13				
E	6.4	0.9	2.6	1.9	7	11.3	<30%	0.17		
E	8.3	0.6	1.9	1.5	4	13.8		0.2		x
E	9.6	0.5	1.3	1.1	4	10.8		0.24		x
E	11.4	0.7	1.8	1.2	6	13.3		0.13	x	x
E	14.4	1.5	3	2.2	3	11.7		0.16	x	x
E	19.7	1.7	5.3	3.2	6	12.8		0.1		x
E	24	2.6	4.3	4.3	5	11.4		0.31	x	
F	4	0.5			1	9				
F	6.2	0.8	2.2	1.3	2	11.5	>40%	0.09		
F	11.1	1.5	4.9	2.3	3	10	<30%	0.03		
F	19.6	3	8.5	4.5	1	13		0.06		
G	4.1	0.6			2	9				
G	6	0.7	1.9	1.3	2	13.5	>40%	0.14		
G	8	0.5	2	1.2	0			0.09		
G	11.3	1.2	3.3	1.7	5	13.2	<30%	0.05		
G	15.2	1.2	3.9	2.4	1	16		0.1		
G	22	1.1	6.8	2.3	1	7		0.003		

470 **Table 3.** COPD peaks extracted for the 2σ model. Mean quality is computed on the set of individual measurements supporting each
471 peak. Spreading value is expressed in % of the mean of measurements supporting the first two peaks per segment. The overlapping
472 coefficient is computed using normalized distributions.

473

474

475

476

477

478

479

480

481

482

	COPD peak values (m)					Increments between peaks (m)				
	Peak 1	Peak 2	Peak 3	Peak 4	Peak 5	Peak 1	Peak 2	Peak 3	Peak 4	Peak 5
B	<u>6.2±2</u> (6.1±1.3)	11.2±1.0	<u>18.1±2.1</u> (18.2±1.4)			<u>6.2±2</u> (6.1±1.3)	5±3.0	<u>6.9±3.1</u> (12.1±2.6)		
C	<u>4.1±1.4</u> (4.2±0.5)	<u>8.8±1.7</u> (9.0±0.8)				<u>4.1±1.4</u> (4.2±0.5)	<u>4.7±3.1</u> (4.8±1.3)			
D	<u>4.5±1.7</u> (5.5±1.8)	8.6±1.9	<u>14.2±1.5</u> (13.7±0.5)	<u>18.2±2.1</u> (16.6±0.7)	<u>24.6±3.3</u> (26.5±1.7)	<u>4.5±1.7</u> (5.5±1.8)	4.1±3.6	5.6±3.4 (8.2±2.3)	4.0±3.6 (2.9±1.2)	6.4±5.4 (9.9±2.4)
E	<u>4.2±1.7</u> (3.8±1.0)	<u>7.4±1.0</u> (6.4±0.9)	11.7±0.9	22.3±2.1		<u>4.2±1.7</u> (3.8±1.0)	<u>3.2±2.7</u> (2.6±1.9)	4.3±1.9	10.6±3.0	
F	<u>5.9±1.8</u> (5.1±1.3)	<u>11.6±2.2</u> (11.1±1.5)				<u>5.9±1.8</u> (5.1±1.3)	<u>5.7±4.0</u> (6.0±2.8)			
G	<u>5.9±1.5</u> (5.1±1.3)	<u>11.3±1.6</u> (11.3±1.2)				<u>5.9±1.5</u> (5.1±1.3)	<u>5.4±3.1</u> (6.2±2.5)			

483

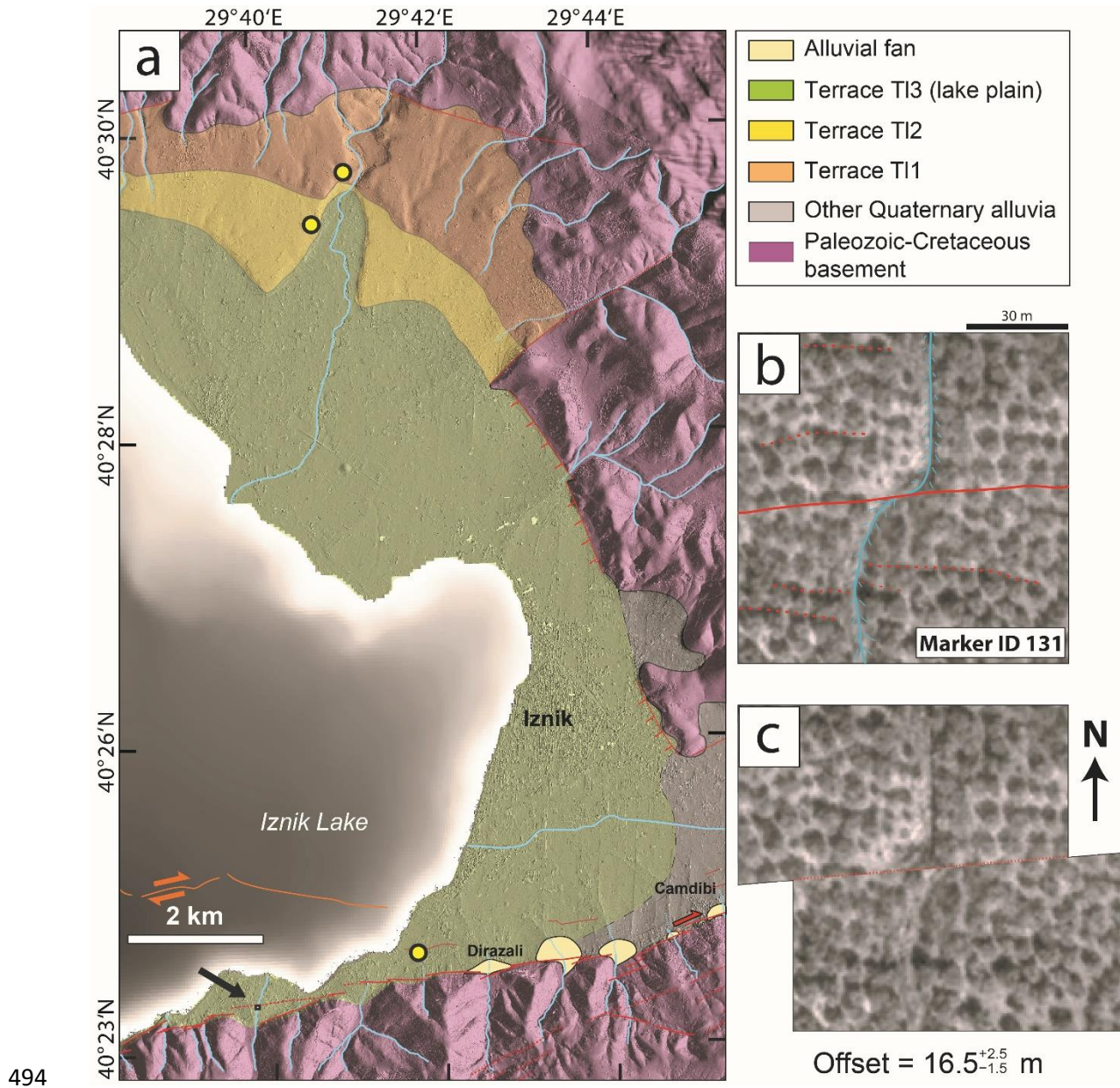
484 **Table 4.** Best constrained cumulative offsets and slip increments computed for each fault segment in the offset range 0-30 m. The
485 retained peaks respect the following conditions: significant increment with preceding peak, more than one supporting individual
486 measurement, less than 30% of spreading with previous peak, consistency through varying segmentation and downsampling.
487 Uncertainties are 1σ . Bold values are from the 1σ model. Values in brackets are those deduced from the 2σ model. We underline
488 values showing consistency between the two models.

Terrace	Sample code	Depth (cm)	Dissolved quartz mass (g)	⁹ Be carrier solution (g)	¹⁰ Be/ ⁹ Be ratio ± 1σ AMS uncertainty (10 ⁻¹⁵ blank corrected)	¹⁰ Be (10 ⁴ at/g)	¹⁰ Be concentration uncertainty (%)	Sampling site location
Tl3	15TUR5-0a	0	17.179	0.2988	9.913 ± 1.208	1.1499	23.05	40.397°N - 29.697°E
Tl3	15TUR5-0b	0	18.480	0.2990	23.17 ± 6.328	2.5003	34.99	94 ± 4 m asl
Tl3	15TUR5-20	20-35	2.864	0.3010	3.428 ± 0.744	2.4060	69.82	TS = 0.997
Tl3	15TUR5-60	60-70	10.739	0.2995	8.012 ± 0.956	1.4902	25.69	
Tl3	15TUR5-80	80-90	16.347	0.2980	12.25 ± 1.234	1.4896	17.91	
Tl3	15TUR5-130	130-140	6.789	0.2976	3.808 ± 0.556	1.1132	49.12	
Tl2	15TUR3-0a	0	20.549	0.3043	178.5 ± 6.176	17.6296	3.65	40.496°N - 29.681°E
Tl2	15TUR3-0b	0	18.510	0.3078	89.09 ± 5.310	9.8809	6.52	127 ± 3 m asl
Tl2	15TUR3-60	60-85	20.824	0.2989	53.09 ± 4.953	5.0837	10.65	TS ~ 1
Tl2	15TUR3-110	110-130	19.941	0.2905	245.1 ± 8.848	23.8183	3.75	
Tl2	15TUR3-150	150-175	17.038	0.2993	200.4 ± 32.61	23.4781	16.79	
Tl1	15TUR4-0a	0	20.838	0.2979	226.9 ± 75.69	21.6293	34.27	40.503°N - 29.686°E
Tl1	15TUR4-0b	0	20.514	0.2973	313.7 ± 11.86	30.3225	3.89	164 ± 3 m asl
Tl1	15TUR4-30	30-40	20.550	0.2958	255.4 ± 7.943	24.5165	3.24	TS ~ 1
Tl1	15TUR4-80	80-90	23.547	0.2981	292.6 ± 11.47	24.7008	4.03	
Tl1	15TUR4-130	130-140	20.510	0.2984	326.3 ± 10.80	31.6621	3.41	
Tl1	15TUR4-260	260-270	22.204	0.2966	184.8 ± 9.776	16.4640	5.52	
Tl1	15TUR4-370	370-380	20.771	0.2980	243.5 ± 12.71	23.2995	5.38	

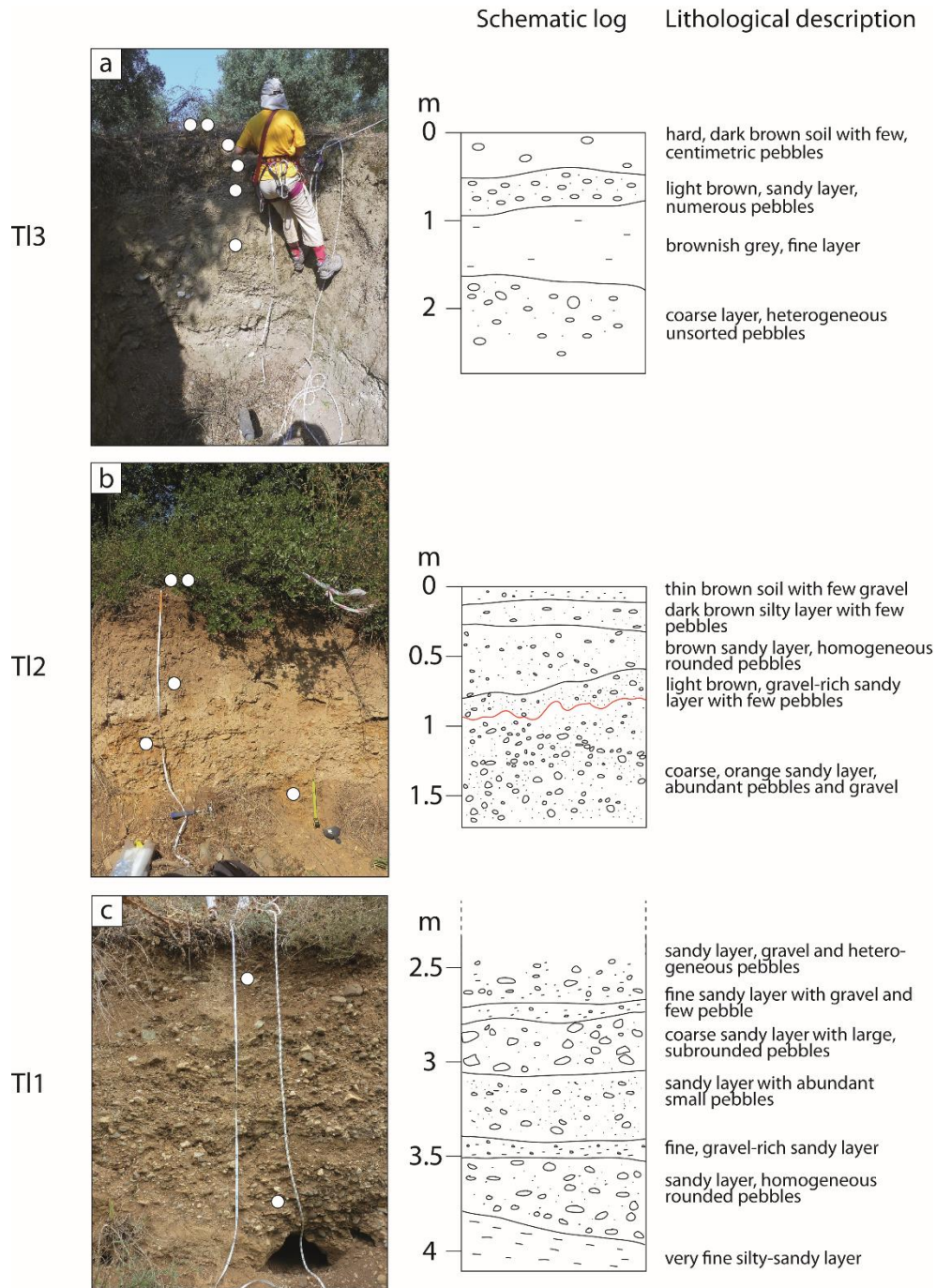
489

490 **Table 5.** Characteristics of the terrace samples and results of the nuclide measurements. The ¹⁰Be/⁹Be ratio of the blank is 6.200.10⁻¹⁵
491 with an analytical uncertainty of 19%. TS is topographic shielding value. The total measurement error includes the uncertainties
492 associated with the AMS measurement, the blank value, the dissolved quartz mass and the spike mass weighing and concentration.

493



495 **Figure 9.** (a) General location of the terrace sampled for cosmogenic dating (yellow dots).
 496 Active faults are mapped in red-orange and main streams are drawn in blue. The subaqueous
 497 fault trace is taken from Gastineau et al. (2021). The eastern limit of terrace T13 is not well
 498 defined in the geomorphology and was drawn assuming a constant elevation. The marker used to
 499 derive a minimum horizontal slip rate is indicated with a black arrow. (b) Interpreted Pleiades
 500 image of the present-day marker morphology. (c) Preferred retro-deformed morphology.



501

502 **Figure 10.** Field photographs (left) and interpreted stratigraphy (right) of the terrace profiles
 503 sampled for dating, Tl3 (a), Tl2 (b), and Tl1 (c). The samples are represented with white circles.
 504 The first meters of Tl1 profile were covered with bushes, and consisted of a homogeneous
 505 brown, silty-sandy unit with a few centimetric pebbles.

506 **6 Terrace dating**

507 Actually, the statistical analysis of cumulative offsets evidences the occurrence of past ruptures
508 along the MNAF and documents the associated slip-per-event, but does not inform the age of
509 these events. To narrow down the age range for the identified events and estimate the late
510 Quaternary slip rate of the MNAF, we need constraints on the age of the terranes that were offset
511 by the fault. For this, we targeted three levels of terraces, which appear particularly well-
512 developed north and east of Iznik Lake (Ikeda et al., 1991; Fig. 9a).

513 **6.1 Sampling and analytical method**

514 To date the terraces, we used the *in-situ* produced terrestrial cosmogenic nuclide (TCN) method.
515 The terraces were sampled along vertical profiles (Fig. 10, Table 5). For terraces T11 and T12,
516 samples were taken on pre-existing scarps, and for terrace T13, which represents the younger,
517 abandoned lake plain, we benefited from a pit dug in the plain for hydrological maintenance. The
518 outcrops displayed alternations of fine sand and coarser gravel-rich conglomerate with graded
519 bedding, with no evidence of buried paleosoils. T11 and T13 mainly showed alluvial facies, the
520 former displaying evidence of paleochannels and cross-stratification. T12 showed lateral facies
521 variations, with finer, lacustrine deposits on the north-central shore of the lake, and coarser
522 fluvial deposits in the east at the sampling site. While T11 and T13 profiles can be assumed to
523 represent a continuous sedimentation sequence, T12 profile displays an irregular interface at 1 m
524 depth that suggests an interruption in the sedimentation process potentially associated with
525 emersion and erosion (Fig. 10b). For each profile, we collected two samples on the surface of the
526 terrace, and when possible, three to four samples in the first 1.5 m below the surface, and one to
527 two deeper samples at the bottom of the profile to constrain the potential inherited nuclide

528 content. We sampled pebbles made of silicate material in order to have ~100 g of quartz per
529 sample.

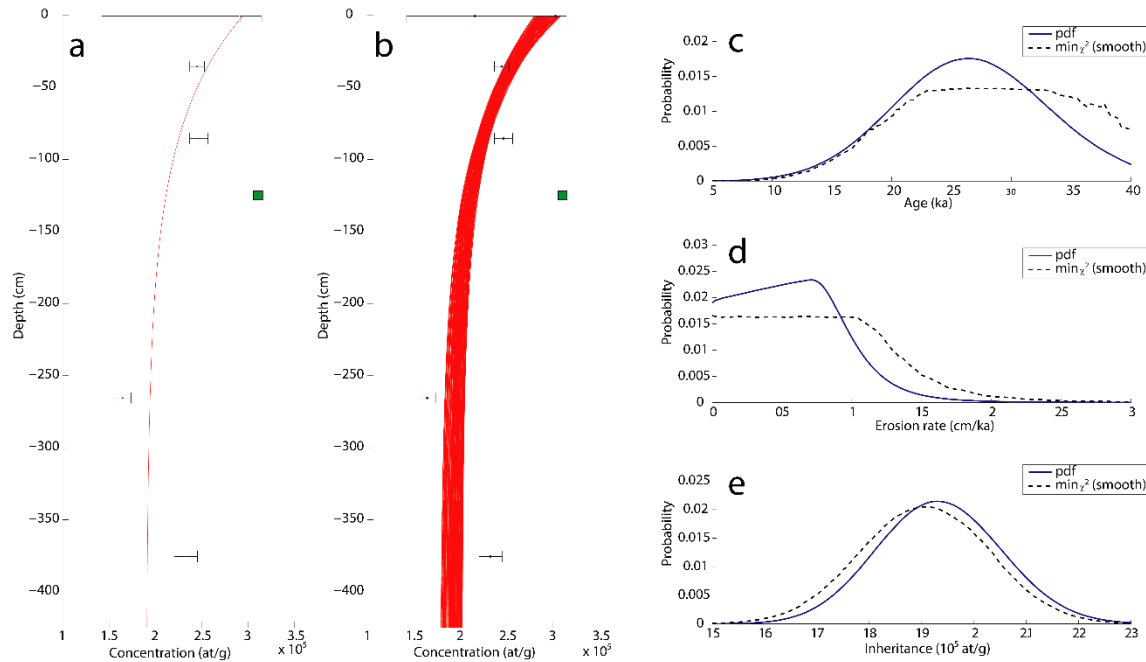
530 The beryllium was extracted at the Geo-thermo-chronology platform (ISTerre, University
531 Grenoble Alpes, France). Quartz was obtained from the 250-500 μm fraction after isolation of
532 the non-magnetic grains by repeated leaching in a $\text{H}_2\text{SiF}_6\text{-HCl}$ mixture. The samples were then
533 processed following the chemical procedure of Brown et al. (1991) and Merchel and Herpers
534 (1999). The beryllium was finally measured as a $^{10}\text{Be}/^9\text{Be}$ ratio at the ASTER Accelerator Mass
535 Spectrometer in Aix-en-Provence, France (Arnold et al., 2010).

536 **6.2 Age determination**

537 The obtained concentration-depth-profiles (Table 5 and Fig. 11, 12, 13) were modelled with a
538 Monte Carlo approach using the code ^{10}Be profile simulator version 1.2 developed by Hidy et al.
539 (2010). This approach enables to find the combination of parameters that best fits the measured
540 profile, including the exposure age, the erosion rate and the inherited TCN concentration. The
541 half-life of ^{10}Be (1.387 ± 0.012 Ma) was taken from Chmeleff et al. (2010). We used a reference
542 production rate of 4.06 ± 0.23 atoms.g $^{-1}$.a $^{-1}$ for the neutron induced spallogenic production at sea
543 level and high latitude using the CREp program (Martin et al., 2017), with the Lifton-Sato-Dunai
544 scaling scheme (Lifton et al., 2014), the ERA40 atmosphere model (Uppala et al., 2005), and the
545 Lifton VDM 2016 geomagnetic correction (Lifton, 2016). The muonic production was calculated
546 using the theoretical equations of Heisinger et al. (2002a,b) and determined at the sampling site's
547 elevation and for a given depth following the approach of Balco et al. (2008). The cumulative
548 bulk density of the material above each sample was assumed constant over depth, with an
549 average value of 2.2 g/cm 3 , previously measured in similar gravel-based terraces (Hidy et al.,

550 2010). For the first iterations, the initial parameters for age, inheritance and erosion rate were
 551 allowed to vary largely.

552



553

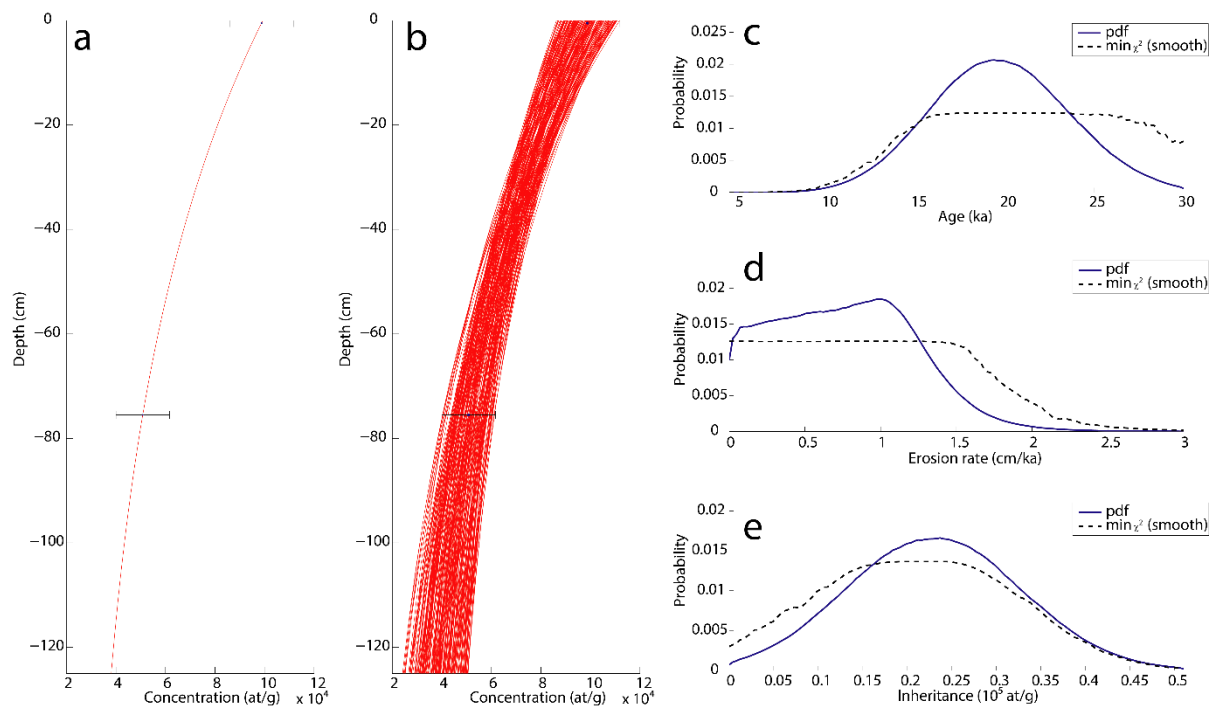
554 **Figure 11.** Result of the Monte Carlo simulations for terrace T11. (a) ^{10}Be concentrations
 555 measured along depth and best fit obtained. (b) All the solutions found in the parameter solution
 556 space defined as inputs. The sample excluded from the inversion is shown as a green box. (c, d,
 557 e) Probability density functions (solid lines) and minimum χ^2 distributions (dashed line) for the
 558 exposure age, erosion rate and inheritance concentration respectively.

559

560 Terrace T11 profile presents one point (15TUR4-130) with a high concentration, larger than the
 561 surface samples, which is incompatible with the theoretical depth profile. The deepest sample
 562 also shows (15TUR4-370) a high concentration, intermediate between 15TUR4-260 and the

563 shallower samples. We ran the simulation only excluding sample 15TUR4-130. The algorithm
 564 was not able to find solutions in the 2σ confidence windows, and we had to increase the χ^2 cut-
 565 off value to 11. The 250,000 solutions obtained provided a most probable, modal age of 27.0
 566 ^{10}Be ka (Fig. 11), a low erosion rate ranging below 1 cm/ka, and a much higher inheritance
 567 around $\sim 190,000$ at/g.

568



569

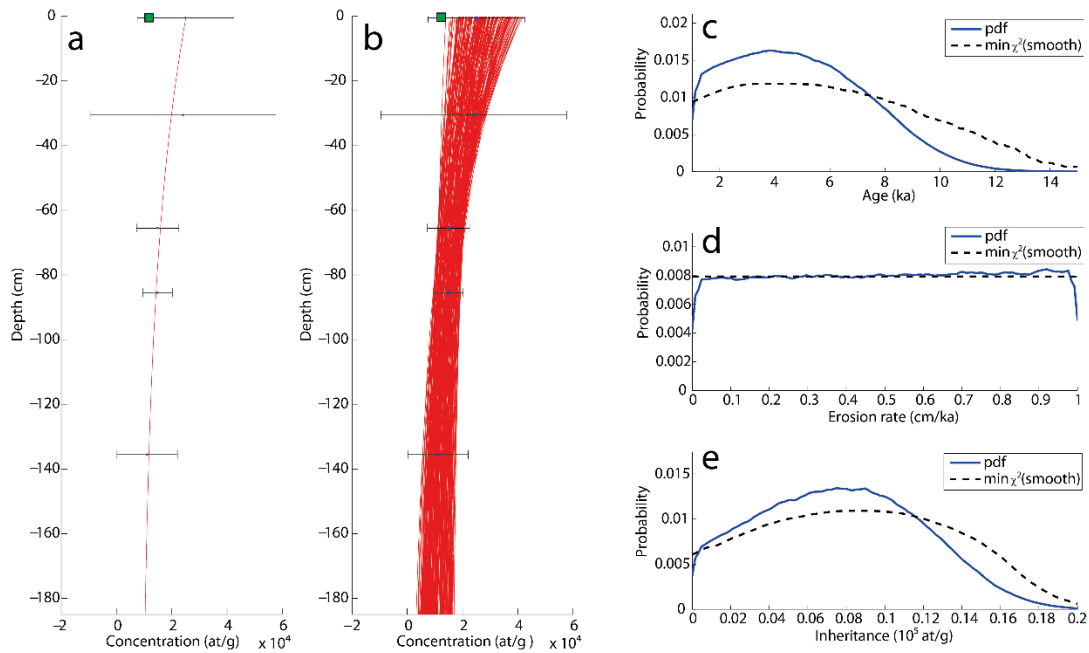
570 **Figure 12.** Result of the Monte Carlo simulations for terrace T12. (a) ^{10}Be concentrations
 571 measured along depth and best fit obtained. (b) All the solutions found in the parameter solution
 572 space defined as inputs. The three samples excluded from the inversion show concentrations
 573 above 120,000 at/g. (c, d, e) Probability density functions (solid lines) and minimum χ^2
 574 distributions (dashed line) for the exposure age, erosion rate and inheritance concentration
 575 respectively.

576 Terrace T12 profile presents more complexity, especially because the two deepest samples
577 (15TUR3-110 and 15TUR3-150) have the highest nuclide concentrations of all the dataset. As
578 the outcrop stratigraphy suggests, they are likely to belong to a previous deposition sequence
579 which was eroded before the onset of a new sedimentation sequence over it. Therefore, we
580 excluded the two deep samples for the simulation. The algorithm could not converge towards a
581 solution for the three remaining points, even when we allowed worse models to be accepted by
582 increasing the χ^2 parameter. We then redid the test excluding sample 15TUR3-0a or 15TUR3-0b,
583 which allowed the algorithm to converge. When keeping the sample 15TUR3-0a, the obtained
584 age was similar to the age found on T11. The other surface sample 15TUR3-0b seems more
585 reliable as it shows a nuclide concentration intermediate between the surface samples of the other
586 terraces. With only two samples, it is impossible to determine statistically robust solutions for the
587 age, erosion rate and inheritance at the same time. To narrow down the solution space, we
588 constrained the initial inheritance using the concentration of sample 15TUR3-60 as upper bound,
589 and the initial age below the age obtained for T11. We finally obtained 250,000 solutions within
590 the 2σ confidence window, giving a most probable age of $19.6_{-7.2}^{+7.7} \text{ }^{10}\text{Be ka}$ (Fig. 12).

591 For terrace T13, the simulator was not able to produce solutions when all the data of the profile
592 were included, especially because one surface sample (15TUR5-0a) showed a very low
593 concentration comparable to the deepest sample (15TUR5-130). We assumed this sample to be
594 an outlier, likely to originate from recent excavation and deposition during agricultural work. We
595 observed that the profile data did not permit to constrain the erosion rate. We tested initial
596 maximum erosion rates of 1, 2 and 3 cm/kyr and obtained similar results between the three
597 simulations. Using a moderate erosion rate of 1 cm/kyr as initial upper bound, the 250,000
598 solutions found within the 2σ confidence window gave a most probable age of $3.8_{-2.7}^{+6.3} \text{ }^{10}\text{Be ka}$.

599 This involves an inheritance of ~ 8000 at/g (i.e. 30% of the surface sample) (Fig. 13e).

600



601

602 **Figure 13.** Result of the Monte Carlo simulations for terrace T13. (a) ^{10}Be concentrations
 603 measured along depth and best fit obtained. (b) All the solutions found in the parameter solution
 604 space defined as inputs. The sample excluded from the inversion is shown as a green box. (c, d,
 605 e) Probability density functions (solid lines) and minimum χ^2 distributions (dashed line) for the
 606 exposure age, erosion rate and inheritance concentration respectively.

607

608 7 Discussion

609 7.1 Horizontal slip rate estimate

610 Horizontal slip rates are usually constrained by dating sedimentary units laterally displaced by

611 the faults (Le Béon et al., 2010; Rizza et al., 2011; van der Woerd et al., 2006). This kind of
612 estimation is preferentially done with cumulative offsets of several hundreds of meters in order
613 to average out the variability of individual coseismic displacements (see e.g. Wechsler et al.,
614 2018). This type of measurement will yield a minimum slip rate as the offset is considered to be
615 as old as the emplacement of the sediments, although it could also be much younger without a
616 way for us to know about it.

617 Southeast of the lake, the MNAF segments have displaced Holocene streams incising in terrace
618 T13, that we have dated at $3.8^{+6.3}_{-2.7}$ ¹⁰Be ka. Among the markers identified, the largest quality 1
619 offset measured was $16.5^{+2.5}_{-1.5}$ m on a river located ~3.5 km west of Dirazali village (Fig. 9). The
620 COPD results suggest that this corresponds to the cumulative slip of the last 3-4 large
621 earthquakes. The ratio between the mean offset and the age of T13 provides a minimum
622 horizontal slip rate of 4.3 mm/yr. This value is in the same range as the rate of 3.7 ± 0.7 mm/yr
623 estimated by Gasperini et al. (2011) on Gemlik segment. Due to the large 2σ upper range for the
624 age of T13, the obtained minimum rate comes with a high level of uncertainty. Dividing the
625 minimum offset by the 2σ upper age gives a lower bound rate of 1.4 mm/yr.

626

627 **7.2 Past seismic events evidenced along-strike**

628 Our study of cumulative offsets along the MNAF provides valuable information on earthquake
629 propagation along this fault, in terms of rupture extent, slip amount and distribution. It also
630 allows us to discuss the behavior of the MNAF segments during the last major earthquakes.

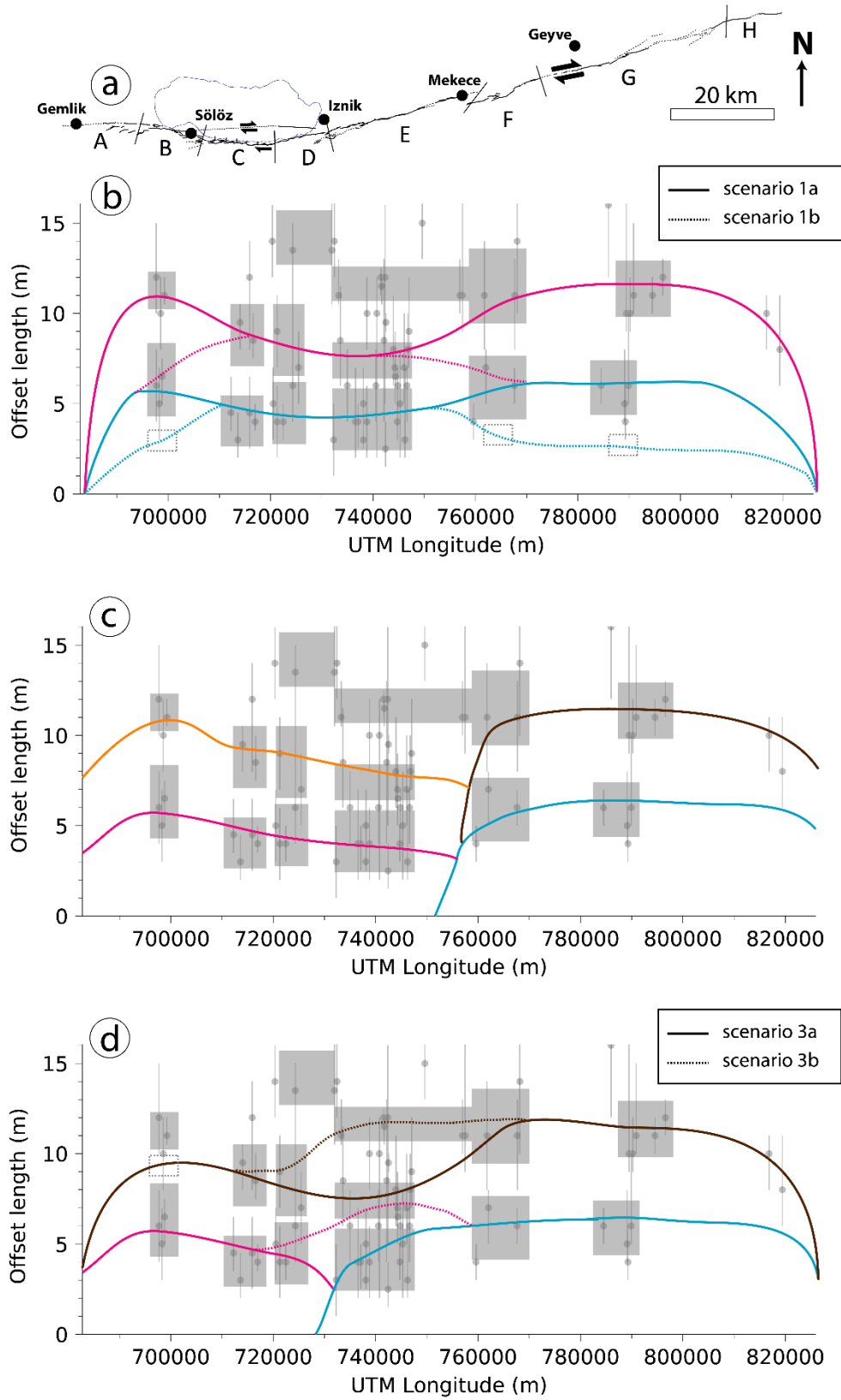
631 If we assume the first two peaks to be the signature of the last two large earthquakes, with

632 respective maximum coseismic slips of 6.2 ± 2 m and 5.7 ± 4 m, empirical scaling laws suggest
633 that they correspond to events of moment magnitude of 7.2 ± 0.2 to 7.4 ± 0.2 , with rupture lengths
634 of 73 ± 28 to 97 ± 42 km (Wells & Coppersmith, 1994; using all-slip-type and strike-slip
635 regressions respectively). Conversely, a rupture extending along the entirety of the 148 km long
636 studies section would correspond to an earthquake of moment magnitude 7.6 ± 0.3 and maximum
637 coseismic displacements of 6.7-6.8 m, using the same scaling relationships. Our results are
638 therefore compatible with large earthquakes able to rupture large parts of the eastern MNAF.
639 Wesnousky (2006) has shown that there exists a maximal step-over size (3-4 km fault-
640 perpendicular) which tends to stop rupture propagation. In our case, Sölöz bend and Mekece,
641 which are the largest identified step-overs of the eastern MNAF, have widths of 2.5 and 1.5 km
642 respectively, and it can thus be assumed that past large ruptures may have propagated through
643 them.

644 Our results show significant along-strike variability of the total number of recorded slip events
645 and the associated slip values. Mean slip values tend to be lower for segments C, D and E. We
646 also note that segments D and E document more individual slip events than the other segments. It
647 has been observed that the COPD curve shows an exponential decay in the peaks' amplitude
648 with increasing cumulative slip (Klinger et al., 2011), as older markers tend to be less preserved
649 in the landscape. We find this kind of pattern for some segments (e.g. segment C), but for
650 segments B and G we observe that peak 1 is smaller than peak 2. The central segments are
651 characterized by higher slopes. This implies more dynamic hydrologic conditions and
652 geomorphic marker formation, and thus a higher capacity to preserve the traces of successive
653 earthquakes (Zielke et al., 2015). By contrast, the lower slopes of the other segments may have
654 favored more intensive agricultural activities, thus partly erasing traces of past ruptures.

655 Therefore, a first possibility to explain the along-strike slip-per-event variability is to assume that
656 COPD peak 1 on segments B, F and G is cumulative, and that the last event was not preserved
657 enough on segments B, F and G to produce a strong COPD peak (Fig. 14b).

658 Alternatively, the slip decrease observed in the central segments may be related to their higher
659 geometrical complexity (fault bends and obliquity, overlapping segments and branching, see
660 sections 2 and 4.2). Distribution of the deformation across several structures implies that only
661 part of the slip can be measured on the investigated MNAF strand, leading to apparent local slip
662 decrease. A more oblique slip vector with a larger, unaccounted for vertical component,
663 especially along segments C and D, may have a similar effect. Lower horizontal coseismic slip
664 values along these segments may also suggest partial partitioning, with the subaqueous Iznik
665 fault accommodating a part of the horizontal displacement (see e.g. de Michele et al., 2010; King
666 et al., 2005 for recent examples of this). Finally, structural complexities may act as a barrier for
667 the propagation of ruptures, leading to smaller offsets through slip tapering (Ward, 1997; Zielke
668 et al., 2015).



670 **Figure 14.** (a) Geometry of the fault section studied. (b) First order scenarios of horizontal slip
671 distribution during past events. The last major event (light blue) is assumed to have ruptured all
672 the segments. The penultimate (magenta) replicates this slip distribution. Alternative scenario 1b
673 assumes a partly unpreserved, smaller slip (broken boxes) for the last major rupture. (c) Scenario
674 2 of horizontal slip distribution. The last rupture is assumed to have propagated in the east of the
675 section studied and along segments F to H. The penultimate event propagated along the
676 remaining segments and further west. The previous events (brown and orange) replicate these
677 slip distributions. (d) Scenario 3 of horizontal slip distribution. The last ruptures propagated
678 partially along the MNAF and neighboring systems. The antepenultimate event (brown) was a
679 full MNAF rupture with a partly unpreserved smaller slip on segment A. Alternative scenario 3b
680 assumes overlapping traces for the last ruptures on segment D.

681

682 The combination of the coseismic slip variation along strike, the epistemic uncertainty affecting
683 offset measurements and the evolution of markers' morphology since the last event can limit the
684 interpretation of COPD peaks as individual earthquakes (Lin et al., 2020; Reitman et al., 2019).
685 Given that the last large earthquake along the MNAF happened before the 20th century and was
686 not accurately documented at the time, we ignore the typical range of variation for the coseismic
687 slip. The surface slip during 1999 Düzce and Izmit earthquakes on the NNAF show coefficients
688 of variation (CoV) of 0.5-0.6 (Akyüz et al., 2002; Barka et al., 2002). Such values of CoV hardly
689 enable to confidently recover more than one or two events or sequence of events from the COPD
690 curve and estimate the associated slip values. Therefore, higher COPD peak values and
691 increments, which come with higher uncertainty, should be considered with caution. A couple of
692 slip increments on segments B and E exceed 6.5 m (Table 4) and seem less realistic given the

693 magnitudes typically observed for recent earthquakes and estimated for historical earthquakes in
694 the Marmara region. Thus, we interpret those as being cumulative contributions of two or more
695 smaller, distinct events.

696 The slip history per segment resulting from our offset analysis does not unambiguously unravel
697 the past earthquakes succession along the MNAF. Alternative scenarios, with different numbers
698 of earthquakes, locations, lengths of ruptures, can be proposed that account equally for these
699 observations. Given the resolution of our satellite images and the uncertainties in our offset
700 measurements, our analysis can hardly detect individual offsets below 2.5 m and thus slip events
701 of $M_w < 7$. We cannot rule out that some smaller slip events were not resolved by our analysis,
702 which would add some local variability of the slip distribution in the possible scenarios. The
703 amount of slip involved in these events would logically be smaller as well, and so the
704 uncertainties associated with them would not fundamentally change the proposed scenarios.

705 To assess the possible scenarios, we require independent constraints about the location, age and
706 characteristics of past earthquakes along the MNAF. Fortunately, the seismicity of the MNAF
707 region of the last two millennia is documented by significant written accounts (see e.g.
708 Ambraseys, 2009), archeological evidence (Benjelloun et al., 2018, 2020) and a few
709 paleoseismological investigations (see section 3). According to the slip rate estimates (sections 3
710 and 7.1), this time frame should correspond to a cumulative horizontal slip ranging between 6
711 and 10 meters. This includes between one and three COPD peaks, depending on segments.

712

713

714 **7.3 Independent constraints on historical earthquakes along the MNAF**

715 **7.3.1 Historical seismicity**

716 At least five destructive ruptures are documented in the historical seismicity catalogues for the
717 eastern part of the MNAF (Ambraseys, 2002, 2009; Ambraseys and Finkel, 1991, 1995;
718 Ambraseys and Jackson, 1998; Guidoboni et al., 1994; Fig. 2; Table S1). These events come
719 with high uncertainties on their location and magnitude, and it is generally difficult to locate the
720 ruptured fault from historical data only. Most of the information available relates to the cities of
721 Iznik and Gemlik. Excluding the earthquakes documented on the NNAF, Iznik was destroyed by
722 local earthquakes around 29-32 CE (M_s 7), in 121 CE (M_s 7.4), in 368 CE (M_s 6.8), and 1065 CE
723 (M_s 6.8). The region of Gemlik was affected by the $M_s \sim 7.2$ 1419 CE earthquake, which may
724 have originated from the SNAF system as no effect was reported in Iznik. A series of minor
725 ruptures, with estimated magnitudes about 5, are known between 1855 and 1863, also felt in
726 Gemlik and along the southern shore of Iznik Lake.

727 **7.3.2 Archeoseismology**

728 Through an archeoseismological study in Iznik, Benjelloun et al. (2020) evidenced three
729 episodes of seismic damage in the city since the Roman period: (1) between the early 6th and late
730 8th century CE, (2) between the mid-9th and late 11th century CE, and (3) after the late 14th
731 century CE. These episodes were associated with a minimal intensity of VIII (EMS-98) in Iznik,
732 suggesting earthquakes of at least M_w 6. The modeling of a standing Roman obelisk north of the
733 city ruled out the occurrence of $M_w > 7.2$ ruptures along the fault section south of Iznik since the
734 1st century AD.

735 **7.3.3 Paleoseismology**

736 Paleoseismological trenching works have documented mid-19th century events on segments A
737 and C. On segment A, a penultimate event was identified between the 12th and 18th centuries CE,
738 but was not seen in trenches located south of Iznik Lake. A possibly contemporaneous event was
739 also documented between the 14th and 18th centuries in a trench west of Mekece. On segment C,
740 one penultimate event was documented after the late 7th century CE, and two older events were
741 identified before the mid-5th century CE in two trenches (see section 3, Fig. 2c). South of Iznik
742 Lake, Erginal et al. (2021) reported a 50 cm high coseismic scarplet in beachrock deposits that
743 they attributed to an 8th century rupture.

744 Other important constraints can be derived from the lake core recently studied by Gastineau et al.
745 (2021). These sedimentary archives recorded the occurrence of several major earthquakes
746 documented both on the NNAF and MNAF, among which the 29-32 CE, 121 CE, 1065 CE, and
747 an 8th century CE event. The 1065 CE earthquake ruptured a sublacustrine fault trace identified
748 within Iznik Lake, north of the onshore segment D. No event was recorded in these cores in the
749 eight centuries following the 1065 CE earthquake, which strongly supports the absence of $M_w >$
750 6.5 events on the central segments of the MNAF after 1065 CE. However, the lack of earthquake
751 recording after 1065 may be due to too low sedimentation rates in the lake in the last millennium,
752 even for large events located farther than 20-30 km from the lake.

753 **7.3.4 Synthesis**

754 The events documented by at least two types of record, include the 29-32 (M_s 7), 121 (M_s 7.4),
755 1065 (M_s 6.8) and 1419 (M_s 7.2) CE historical earthquakes. The precise location of the 1419 CE
756 earthquake is not well constrained, but the fact that it was not recorded in the Iznik Lake cores

757 nor in trenches south of Iznik Lake, and that destructions were only reported in the region of
758 Bursa, suggest that it did not extend east of Sölöz. To these we can add an 8th century event
759 which affected the central MNAF segments south of Iznik Lake, and a 14th-18th century event
760 attested by some damaged buildings in Iznik and one trench on segment E.

761

762 **7.4 Analysis of COPD peak 1**

763 In a first assumption (Fig. 14b, scenario 1a), COPD peak 1 can be interpreted as a large Mw 7.2-
764 7.4 event rupturing the whole length of the studied fault. This first interpretation involves
765 significant slip variations along strike, with slip values on the central segments C, D and E ~33%
766 lower than on the other segments. The hypothesis of differential preservation across segments
767 suggests another scenario (Fig. 14b, scenario 1b), with a more homogeneous slip of ~4 m along
768 the studied section, only recovered on the central segments. Instead of decreasing slip on the
769 central segments as in the scenario 1a, this scenario involves a maximum slip in the central area,
770 which decrease towards both rupture tips. Given the higher structural complexity of this area,
771 lower horizontal slip values are expected along the central segments. Therefore, scenario 1a can
772 be considered more likely than scenario 1b. The favored historical candidate is the 1065 CE
773 earthquake, which is the best documented event. However, this means that the magnitude of the
774 1065 CE earthquake, estimated at 6.8 by historical seismology studies, should be significantly
775 raised, by at least 0.3 units. It also implies that the 1065 CE rupture identified in Iznik lake
776 propagated along the onshore fault segments as well. In addition, the deformation of the obelisk
777 north of Iznik does not support magnitudes over Mw 7.2 for events located south of Iznik, but
778 might be accounted for with a more distant epicenter, located on the western or eastern segments

779 (Benjelloun et al., 2020).

780 Another possibility is to propose earthquakes rupturing only a part of the studied MNAF section,
781 with the central segments acting as a slip barrier (Fig. 14c, d). Following this hypothesis, COPD
782 peak 1 would correspond to two different earthquakes. These earthquakes ruptured different
783 sections of the fault, either adjacent (scenarios 2 and 3a) or overlapping (scenario 3b). The lower
784 slip values on the central segments are associated with the termination of earthquakes. In this
785 case, no significant slip variation appears along strike. The high slip values imply that the
786 ruptured area during these earthquakes could be respectively extended west of Gemlik and east
787 of the junction with the main NAF strand. This interpretation best accounts for the multiple
788 events found in the different records of past seismicity. The 1065 CE earthquake is a favored
789 candidate for the western and central segments. The historical seismicity of the east of the
790 studied area is less documented, but the 14th-18th c. event found in the archeological and
791 paleoseismic record is a possible candidate for the eastern rupture of this scenario.

792

793 **7.5 Analysis of COPD peak 2 and implications for the long-term behavior of the MNAF**

794 The increments between COPD peaks 1 and 2 suggest that the slip values of the last and
795 penultimate events (or sequences of events) were comparable. Although the slip values estimated
796 for the penultimate event come with higher uncertainties, they also suggest magnitudes as high
797 as $M_w 7.4 \pm 0.2$. The lacustrine record documents at least two events in the first centuries CE
798 (Gastineau et al., 2021). The historical catalogues include two candidates, in 29-32 CE and in
799 121 CE, with poorly constrained locations along the MNAF. Both events can be accounted for
800 by interpreting peak 2 as two distinct ruptures (scenario 2, Fig. 14c). Given the uncertainties, a

801 full MNAF rupture may also be proposed (scenarios 1 and 3, Fig. 14b and d).

802 The reconstructions of along-fault slip accumulation derived from systematic offset
803 measurements have been associated to the development of earthquake recurrence models
804 (Schwartz & Coppersmith, 1984; Zielke et al., 2015). In our case, given the large uncertainties,
805 the successive increments on each segment cannot be unambiguously discriminated. Our dataset
806 remains compatible with a “characteristic slip” behavior, as in scenarios 1 and 2 (Fig. 14b, c),
807 where the earthquakes show recurring, similar slip distributions (see e. g. Klinger et al., 2011;
808 Kurtz et al., 2018; Zielke et al., 2010). In scenarios 1a and 2, the horizontal cumulative slip on
809 segments C, D and E is 25-35% lower than on the other segments for the last two events. This
810 cumulative slip deficit on the central segments produces a higher apparent slip rate variation
811 along-strike. The interpretations of scenario 3 depart from the characteristic slip model, as the
812 proposed distributions of the last events differ from the previous one, which resembles a variable
813 slip model.

814 The Late Quaternary slip accumulation along the MNAF seems dominated by large events with
815 comparable per-segment slip increments. This corresponds to the synoptic model of Zielke et al.
816 (2015), which also considers the occurrence of smaller ruptures contributing marginally to the
817 overall slip accumulation. The 8th century CE event reported south of Iznik Lake (Erginal et al.,
818 2021), and the 19th century CE earthquakes reported in Gemlik (Özalp et al., 2013) may illustrate
819 these features. Future trenching work is needed to document the timing of earthquakes and to
820 judge between both models.

821

822

823 **7.6 Possible interactions between the NAF strands for the historical period**

824 In all the scenarios discussed, we can propose that the eastern MNAF has experienced two major
825 sequences of ruptures in the last two millennia. These historical sequences correspond to large
826 magnitude events, with amounts of slip ranging between 3.2 and 6.2 m. Most of the deformation
827 was produced during intervals of high seismic activity, separated by longer quiescent periods
828 (1000-1500 years). This can be compared to the rupture history of other strike-slip fault systems
829 such as the San Andreas and Dead Sea faults (Lefevre et al., 2018; Rockwell et al., 2014). This
830 long recurrence time contrasts with the historical behavior of the NNAF (Fig. 2), and is
831 consistent with a slip rate ~5 times smaller on the MNAF. In the final part of this discussion, we
832 replace our propositions of past rupture history in the wider frame of the eastern Marmara region.

833 The last sequence of high seismicity along the MNAF, whatever the scenario considered, seems
834 to occur between the 11th and 18th centuries, while the northern strand of the NAF along the
835 Izmit Gulf (between 29.2° and 30.3°E) knew a period of lower seismic activity (Fig. 2b). The
836 1065 CE earthquake was preceded by a major event on the NNAF in 1063 CE. However, it
837 mainly affected the western part of the Marmara region, with no significant damage reported east
838 of Constantinople (Ambraseys, 2009). Between the 14th and 18th centuries, only one major
839 earthquake is known for the eastern Marmara region in 1509 CE (M~7.2). The Gulf of Izmit was
840 likely affected by this earthquake (Klinger et al., 2003), but the contemporary historical records
841 do not account for heavy damage farther east (Ambraseys, 2001b). After this earthquake, a
842 quiescence period is reported for the Marmara region between 1509 and 1719 CE (Ambraseys &
843 Jacskon, 2000; Pondard et al., 2007; Rockwell et al., 2009).

844 By contrast, the southern strands of the NAF were marked by a significant seismic activity in the

845 east of the Marmara Sea. After the 1065 CE earthquake on the MNAF, this activity seems to
846 restart in the early 15th century CE. It includes the 1419 CE earthquake which affected the Bursa
847 region, and the event proposed between the 14th and 18th centuries CE along the eastern segments
848 of the MNAF (scenarios 2 and 3). This earthquake may have propagated across the junction with
849 the main NAF strand. The junction zone does not present any significant step-over, but only an
850 azimuth change of $\sim 20^\circ$. The 1967 CE earthquake propagated across this junction between the
851 main NAF and the NNAF, with a similar azimuth difference. Therefore, a symmetrical rupture
852 between the main NAF and the MNAF is not unrealistic. A trenching study carried out by
853 Palyvos et al. (2007) in the Mudurnu valley, located a few kilometers east of the junction with
854 the main NAF strand, identified at least two events younger than 1394 CE. The authors have
855 suggested that some of these ruptures may have propagated across of the junction along the
856 MNAF. Analogous alternations of active and quiescent phases between adjacent fault strands
857 have been previously identified on the San Andreas fault system in relation to the San Jacinto
858 fault (Lozos, 2016; Onderdonk et al., 2018). In the case of the NAF in the Marmara region, the
859 investigation of older sedimentary records of past earthquakes on the different strands might help
860 to better document this behavior and check for earlier occurrences of it.

861

862 **8 Conclusion**

863 By combining field observations and the analysis of high-resolution satellite images, we have
864 demonstrated that the segments constituting the MNAF in the southeast of the Marmara region
865 have been significantly active during the Holocene. The fault displays morphological features
866 typical of strike-slip deformation, associated locally with a smaller vertical component. We

867 collected 114 measurements of horizontally offset markers, providing evidence for large,
868 repeated earthquakes along the MNAF. Through a statistical analysis of the offsets, we
869 particularly documented at least two major surface-rupturing earthquakes whose deformation
870 was preserved in the landscape. They are characterized by coseismic horizontal displacement
871 ranging from 3.2 to 6.2 m, which indicates moment magnitudes ranging between 7.2 ± 0.2 and
872 7.4 ± 0.2 according to empirical scaling laws. Some of these events may have ruptured the whole
873 eastern MNAF section along more than 100 km. Although smaller earthquakes also happened in
874 the past, our analysis may not resolve accurately their frequency due to the data uncertainties and
875 preservation issues. According to the historical catalogues of seismicity and paleoseismological
876 studies, the last large events documented along this fault strand possibly happened in 1065 CE,
877 or between the 14th and 18th centuries CE along the eastern segments. These intervals correspond
878 to a period of relative quiescence along the NNAF segments located east of the Marmara Sea.
879 We estimated a late Holocene horizontal slip rate of ~ 4.3 mm/yr on the central MNAF segments,
880 in agreement with previous estimates. Since the last large events, the eastern MNAF segments
881 may have therefore accumulated stress equivalent to 1-4 m of horizontal deformation. Therefore,
882 the current level of stress may be enough to generate a significant earthquake, comparable or
883 larger than a 1065 CE type rupture, which caused important damage in Iznik. The activity of the
884 secondary strands of the NAF should not be neglected in terms of slip history and should be
885 considered into any seismic hazard assessment.

886

887 **Data Availability Statement**

888 The bathymetric map of Marmara was made available by the EMODnet Bathymetry project

889 (<https://www.emodnet.eu/bathymetry>), using the EMODnet Bathymetry portal (EMODnet
890 Bathymetry Consortium, 2016, EMODnet Digital Bathymetry [DTM], DOI:
891 10.12770/c7b53704-999d-4721-b1a3-04ec60c87238) funded by the European Commission
892 Directorate General for Maritime Affairs and Fisheries. The large-scale topography of the study
893 area was obtained from the Shuttle Radar Topography Mission 1 Arc-Second Global
894 (DOI:10.5066/F7PR7TFT). The bathymetry of İznik Lake was provided by and can be obtained
895 from the Turkish General Directorate of Hydraulic Works (DSI). Pleiades imagery is available
896 for purchase from Airbus industry (<https://www.intelligence-airbusds.com/en/8692-pleiades>).
897 The full offset retro-deformation dataset and a vector file of the fault map are available on the
898 Zenodo repository (Benjelloun et al., 2021) [open access]. The maps of Figures 5 are from
899 Google Earth satellite imagery. The diagrams of Figures 6, 7, 8 and 14 were prepared using the
900 Matplotlib 3.3.0 package for Python (<https://matplotlib.org/>; Hunter, 2007). All websites were
901 last accessed in January 2021. Supporting Information for this article includes a detailed
902 explanation of the marker quality score determination, a list of historical earthquakes in the area
903 of interest, a summary of paleoseismic trenching works done in the area, the offset measurement
904 data, and supplementary figures on the vertical slip markers south of Iznik Lake, some field
905 examples of Quaternary faulting, and the automatic fault discretization procedure.

906

907 **Acknowledgments**

908 This work has been supported by the Mediterranean Integrated STudies at Regional And Local
909 Scales – ENVIronment of the MEDiterranean (MISTRALS-ENVIMED) program (The North
910 Anatolian Fault in the region Iznik: Geomorphological Evolution and Archaeoseismicity

911 [NAFIGEA] project), and the Institut National des Sciences de l'Univers (INSU) Aleas program
912 (France). The Pleiades images were bought with support from LabEx OSUG@2020
913 (Investissements d'avenir – ANR10 LABX56, France). This study contributes to the IdEx
914 Université de Paris ANR-18-IDEX-0001. The authors warmly thank the ASTER team (D.
915 Boulès, G. Aumaitre, K. Keddadouche, and R. Braucher) for the measurements performed at the
916 ASTER AMS facility (CEREGE, Aix-en-Provence). We thank the Turkish Ministry of Culture
917 and Tourism for allowing the field work. We thank Pr. Mustafa Sahin and his research group,
918 and the Kandilli observatory in Iznik for their help with logistics and housing. The authors
919 declare no conflict of interests.

920

921 **References**

922 Aki, K. (1984). Asperities, barriers, characteristic earthquakes and strong motion prediction.
923 *Journal of Geophysical Research: Solid Earth*, 89(B7), 5867–5872.

924 Akyüz, S., Dogan, B., Aksoy, M. E., Tigli, O., & Zabcı, C. (2014). *Preliminary*
925 *Palaeoseismological results of the Middle Strand of the North Anatolian Fault (NAF) in the*
926 *Marmara Region, NW Turkey*. Paper presented at European Geosciences Union General
927 Assembly, Vienna, Austria.

928 Akyüz, H. S., Hartleb, R., Barka, A., Altunel, E., Sunal, G., Meyer, B., & Armijo, R. (2002).
929 Surface rupture and slip distribution of the 12 November 1999 Düzce earthquake (M 7.1), North
930 Anatolian fault, Bolu, Turkey. *Bulletin of the Seismological Society of America*, 92(1), 61-66.

931 <https://doi.org/10.1785/0120000840>

932 Akyuz, H. S. & Zabcı, C. (2012). *A review of paleoseismic investigations along the North*

- 933 *Anatolian Fault, Turkey*. Paper presented at PANAF: Paleoseismology Along the North
934 Anatolian Fault Meeting, Istanbul, Turkey.
- 935 Ambraseys, N. (2000). The Seismicity of the Marmara Sea Area 1800-1899. *Journal of*
936 *Earthquake Engineering*, 4(3), 377–401. <https://doi.org/10.1080/13632460009350376>
- 937 Ambraseys, N. N. (2001a). Reassessment of earthquakes, 1900–1999, in the eastern
938 Mediterranean and the Middle East. *Geophysical Journal International*, 145(2), 471–485.
939 <https://doi.org/10.1046/j.0956-540x.2001.01396.x>
- 940 Ambraseys, N. N. (2001b). The Earthquake of 1509 in the Sea of Marmara, Turkey, Revisited.
941 *Bulletin of the Seismological Society of America*, 91(6), 1397-1416.
942 <https://doi.org/10.1785/0120000305>
- 943 Ambraseys, N. (2002). The seismic activity of the Marmara Sea region over the last 2000 years.
944 *Bulletin of the Seismological Society of America*, 92(1), 1–18.
945 <https://doi.org/10.1785/0120000843>
- 946 Ambraseys, N. (2009). *Earthquakes in the Mediterranean and Middle East. A multidisciplinary*
947 *study of seismicity up to 1900*. Cambridge: Cambridge University Press.
948 <https://doi.org/10.1017/CBO9781139195430>
- 949 Ambraseys, N. & Finkel, C. (1991). Long-term seismicity of Istanbul and of the Marmara Sea
950 region. *Terra Nova*, 3(5), 527–539. <https://doi.org/10.1111/j.1365-3121.1991.tb00188.x>
- 951 Ambraseys, N. N., & Finkel, C. F. (1995). The Seismicity of Turkey and Adjacent Areas: A
952 Historical Review, 1500–1800. Istanbul: Muhittin Salih Eren.
- 953 Ambraseys, N. N., & Jackson, J. (1998). Faulting associated with historical and recent

- 954 earthquakes in the eastern Mediterranean region. *Geophysical Journal International*, 133(2),
955 390–406. <https://doi.org/10.1046/j.1365-246X.1998.00508.x>
- 956 Ambraseys, N.N., & Jackson, J.A. (2000). Seismicity of the Sea of Marmara (Turkey) since
957 1500. *Geophysical Journal International*, 141(3), F1-F6. <https://doi.org/10.1046/j.1365-246x.2000.00137.x>
- 959 Ambraseys, N. N., Jackson, J. A., & Melville, C. P. (2002). Historical Seismicity and Tectonics:
960 The Case of the Eastern Mediterranean and the Middle East. In: Lee, W. H. K., Kanamori, H.,
961 Jennings, P. C., & Kisslinger, C. (Eds.). *International Handbook of Earthquake and Engineering*
962 *Seismology* (Part A, pp. 747-763). Cambridge, MA: Academic Press.
963 [https://doi.org/10.1016/S0074-6142\(02\)80248-0](https://doi.org/10.1016/S0074-6142(02)80248-0)
- 964 Ansberque, C., Bellier, O., Godard, V., Lasserre, C., Wang, M., Braucher, R., et al. (2016). The
965 Longriqu fault zone, eastern Tibetan Plateau: Segmentation and Holocene behavior. *Tectonics*,
966 35(3), 565–585.
- 967 Armijo, R., Meyer, B., Hubert, A., & Barka, A. A. (1999). Westward propagation of the North
968 Anatolian fault into the northern Aegean: Timing and kinematics. *Geology*, 27, 267–270.
969 [https://doi.org/10.1130/0091-7613\(2000\)28<188:WPONAF>2.0.CO;2](https://doi.org/10.1130/0091-7613(2000)28<188:WPONAF>2.0.CO;2)
- 970 Armijo, R., Meyer, B., Navarro, S., King, G., & Barka, A. (2002). Asymmetric slip partitioning
971 in the Sea of Marmara pull-apart: a clue to propagation processes of the North Anatolian Fault?
972 *Terra Nova*, 14(2), 80–86. <https://doi.org/10.1046/j.1365-3121.2002.00397.x>
- 973 Arnold, M., Merchel, S., Boursès, D. L., Braucher, R., Benedetti, L., Finkel, R. C., et al. (2010).
974 The French accelerator mass spectrometry facility ASTER: Improved performance and
975 developments. *Nuclear Instruments and Methods in Physics Research Section B: Beam*

- 976 *Interactions with Materials and Atoms*, 268, 1954-1959.
- 977 <https://doi.org/10.1016/j.nimb.2010.02.107>
- 978 Balco, G., Stone, J. O., Lifton, N. A., & Dunai, T. J. (2008). A complete and easily accessible
979 means of calculating surface exposure ages or erosion rates from ^{10}Be and ^{26}Al measurements.
980 *Quaternary Geochronology*, 3(3), 174 – 195. <https://doi.org/10.1016/j.quageo.2007.12.001>
- 981 Baris, S., Ito, A., Üçer, S. B., Honkura, Y., Kafadar, N., Pektas, R., et al. (2002).
982 Microearthquake Activity before the Izmit Earthquake in the Eastern Marmara region, Turkey (1
983 January 1993-17 August 1999). *Bulletin of the Seismological Society of America*, 92(1), 394–
984 405. <https://doi.org/10.1785/0120000826>
- 985 Barka, A. (1992). The North Anatolian fault zone. *Annales Tectonicae*, 6, 164–195.
- 986 Barka, A. (1993). *Kuzey Anadolu Fayı'nın Sapanca-Izmit ve Geyve-Iznik Kolları üzerinde*
987 *Palaeosismik Arastirmalar* (Technical Report YBAG-4/7551). Istanbul: TÜBİTAK.
- 988 Barka, A. (1996). Slip distribution along the North Anatolian fault associated with the large
989 earthquakes of the period 1939 to 1967. *Bulletin of the Seismological Society of America*, 86(5),
990 1238–1254.
- 991 Barka, A., Akyüz, H. S., Altunel, E., Sunal, G., Cakir, Z., Dikbas, A., et al. (2002). The Surface
992 Rupture and Slip Distribution of the 17 August 1999 Izmit Earthquake ($M 7.4$), North Anatolian
993 Fault. *Bulletin of the Seismological Society of America*, 92(1), 43-60.
994 <https://doi.org/10.1785/0120000841>
- 995 Barka, A. & Kadinsky-Cade, K. (1988). Strike-slip fault geometry in Turkey and its influence on
996 earthquake activity. *Tectonics*, 7(3), 663–684.
- 997 Beauprêtre, S., Garambois, S., Manighetti, I., Malavieille, J., Sénéchal, G., Chatton, M., et al.

- 998 (2012). Finding the buried record of paste earthquakes with GPR-based palaeoseismology: a case
999 study on the Hope fault, New Zealand. *Geophysical Journal International*, 189(1), 73-100.
1000 <https://doi.org/10.1111/j.1365-246X.2012.05366.x>
- 1001 Beauprêtre, S., Manighetti, I., Garambois, S., Malavieille, J., & Dominguez, S. (2013).
1002 Stratigraphic architecture and fault offsets of alluvial terraces at Te Marua, Wellington fault,
1003 New Zealand, revealed by pseudo-3D GPR investigation. *Journal of Geophysical Research:*
1004 *Solid Earth*, 118, 4564-4585.
- 1005 Benjelloun, Y., de Sigoyer, Dessales, H., Baillet, L., Guéguen, P., & Sahin, M. (2020). Historical
1006 Earthquake Scenarios for the Middle Strand of the North Anatolian Fault Deduced from Archeo-
1007 Damage Inventory and Building Deformation Modeling. *Seismological Research Letters*, 92,
1008 583-598. <https://doi.org/10.1785/0220200278>
- 1009 Benjelloun, Y., de Sigoyer, J., Dessales, H., Garambois, S., & Sahin, M. (2018). Construction
1010 history of the aqueduct of Nicaea (Iznik, NW Turkey) and its on-fault deformation viewed from
1011 archaeological and geophysical investigations. *Journal of Archaeological Science: Reports*, 21,
1012 389-400. <https://doi.org/10.1016/j.jasrep.2018.08.010>
- 1013 Benjelloun, Y., de Sigoyer, J., Garambois, S., Carcaillet, J., & Klinger, Y. (2021). Data for:
1014 Segmentation and Holocene Behavior of the Middle Strand of the North Anatolian Fault (NW
1015 Turkey) (Version 1.0.0) [Data set]. Zenodo. <http://doi.org/10.5281/zenodo.4467906>
- 1016 Broxton, M. J. & Edwards, L. J. (2008). *The Ames Stereo Pipeline: Automated 3D Surface*
1017 *Reconstruction from Orbital Imagery*. Paper presented at the 39th Lunar and Planetary Science
1018 Conference, League City, TX.
- 1019 Brown, E. T., Edmond, J. M., Raisbeck, G. M., Yiou, F., Kurz, M. D., & Brook, E. J. (1991).

- 1020 Examination of surface exposure ages of Antarctic moraines using in situ produced ^{10}Be and
1021 ^{26}Al . *Geochimica et Cosmochimica Acta*, 55, 2269-2283. [https://doi.org/10.1016-](https://doi.org/10.1016/0016-7037(91)90103-C)
1022 7037(91)90103-C
- 1023 Chmeleff, J., von Blanckenburg, F., Kossert, K., & Jakob, D. (2010). Determination of the ^{10}Be
1024 half-life by multicollector ICP-MS and liquid scintillation counting. *Nuclear Instruments and*
1025 *Methods in Physics Research Section B: Beam Interactions with Materials and Atoms*, 268(2),
1026 192–199. <https://doi.org/10.1016/j.nimb.2009.09.012>
- 1027 Choi, J. H., Klinger, Y., Ferry, M., Ritz, J. F., Kurtz, R., Rizza, M. et al. (2018). Geologic
1028 Inheritance and Earthquake Rupture Processes: The 1905 $M \geq 8$ Tsetserleg-Bulnay Strike-Slip
1029 Earthquake Sequence, Mongolia. *Journal of Geophysical Research: Solid Earth*, 123.
1030 <https://doi.org/10.1002/2017JB013962>.
- 1031 Civico, R., Smedile, A., Pantosti, D., Cinti, F. R., De Martini, P. M., Pucci, S., et al. (2021). New
1032 trenching results along the Iznik segment of the central strand of the North Anatolian Fault
1033 (Turkey): an integration with preexisting data. *Mediterranean Geoscience Reviews*.
1034 <https://doi.org/10.1007/s42990-021-00054-9>
- 1035 de Michele, M., Raucoules, D., de Sigoyer, J., Pubellier, M., & Chamot-Rooke, N. (2010).
1036 Three-dimensional surface displacement of the 2008 May 12 Sichuan earthquake (China)
1037 derived from Synthetic Aperture Radar: evidence for rupture on a blind thrust. *Geophysical*
1038 *Journal International*, 183(3), 1097-1103. <https://doi.org/10.1111/j.1365-246X.2010.04807.x>
- 1039 Dikbas, A., Akyüz, H. S., Meghraoui, M., Ferry, M., Altunel, E., Zabcı, C., et al. (2018).
1040 Paleoseismic history and slip rate along the Sapanca-Akyazi segment of the 1999 Izmit
1041 earthquake rupture ($MW=7.4$) of the North Anatolian Fault (Turkey). *Tectonophysics*, 738-739,

- 1042 92-111. <https://doi.org/10.1016/j.tecto.2018.04.019>
- 1043 Dogan, B. (2010). *Kuzey Anadolu Fay Sistemi Güney Kolunun Geyve-Gemlik Arasındaki*
1044 *Kesiminin Morfotektonik, Tektonostratigrafik ve Palaeosismolojik Evrimi*. (Doctoral
1045 dissertation). Istanbul: Istanbul Teknik Üniversitesi.
- 1046 Elliott, J. R., Walters, R. J., & Wright, T. J. (2016). The role of space-based observation in
1047 understanding and responding to active tectonics and earthquakes. *Nature Communications*, 7,
1048 13844. <https://doi.org/10.1038/ncomms13844>
- 1049 Emre, Ö., Duman, T. Y., & Özalp, S. (2011). *1:250.000 Ölçekli Türkiye Diri Fay Haritası Serisi*.
1050 (Technical report). Ankara: Maden Tetkik ve Arama Genel Müdürlüğü.
- 1051 Erginal, A. E., Erenoglu, R. C., Yildirim, C., Selim, H., H., Kiyak, N. G, Erenoglu, O, et al.
1052 (2021). Co-seismic beachrock deformation of 8th century CE Earthquake in Middle Strand of
1053 North Anatolian Fault, Lake Iznik, NW Turkey. *Tectonophysics*, 799, 2286990.
1054 <https://doi.org/10.1016/j.tecto.2020.228690>
- 1055 Ergintav, S., Reilinger, R. E., Çakmak, R., Floyd, M., Cakir, Z., Dogan, U., et al. (2014).
1056 Istanbul's earthquake hot spots: Geodetic constraints on strain accumulation along faults in the
1057 Marmara seismic gap. *Geophysical Research Letters*, 41(16), 5783–5788.
1058 <https://doi.org/10.1002/2014GL060985>
- 1059 Flerit, F., Armijo, R., King, G. C. P., Meyer, B., & Barka, A. (2003). Slip partitioning in the Sea
1060 of Marmara pull-apart determined from GPS velocity vectors. *Geophysical Journal*
1061 *International*, 154(1), 1–7. <https://doi.org/10.1046/j.1365-246X.2003.01899.x>
- 1062 Fraser, J., Vanneste, K., & Hubert-Ferrari, A. (2010). Recent behavior of the North Anatolian
1063 Fault: Insights from an integrated palaeoseismological data set. *Journal of Geophysical*

- 1064 *Research: Solid Earth*, 115(B9): B09316.
- 1065 Fu, B., Ninomiya, Y., Lei, X., Toda, S., & Awata, Y. (2004). Mapping active fault associated
1066 with the 2003 Mw 6.6 Bam (SE Iran) earthquake with ASTER 3D images. *Remote Sensing of*
1067 *Environment*, 92(2), 153–157. <https://doi.org/10.1016/j.rse.2004.05.019>
- 1068 Gastineau, R., de Sigoyer, J., Sabatier, P., Fabbri, S. C., Anselmetti, F. S., Develle, A. L., et al.
1069 (2021). Active subaquatic fault segments in Lake Iznik along the middle strand of the North
1070 Anatolian Fault, NW Turkey. *Tectonics*, 40, e2020TC006404.
- 1071 Gasperini, L., Polonia, A., Çagatay, M. N., Bortoluzzi, G., & Ferrante, V. (2011). Geological
1072 slip rates along the North Anatolian Fault in the Marmara region. *Tectonics*, 30(6), TC6001.
- 1073 Gold, P. O., Oskin, M. E., Elliott, A. J., Hinojosa-Corona, A., Taylor, M. H., Kreylos, O., &
1074 Cowgill, E. (2013). Coseismic slip variation assessed from terrestrial lidar scans of the El
1075 Mayor-Cucapah surface rupture. *Earth and Planetary Science Letters*, 366, 151-162.
1076 <https://doi.org/10.1016/j.epsl.2013.01.040>
- 1077 Guidoboni, E., and Comastri, A. (Eds.) (2005). *Catalogue of Earthquakes and Tsunamis in the*
1078 *Mediterranean Area From the 11th to the 15th Century*. Roma: Istituto Nazionale di Geofisica e
1079 Vulcanologia.
- 1080 Guidoboni, E., Comastri, A., & Traina, G. (1994). Catalogue of ancient earthquakes in the
1081 Mediterranean area up to the 10th century. Roma: Istituto Nazionale di Geofisica.
- 1082 Gürbüz, C., Aktar, M., Eyidogan, H., Cisternas, A., Haessler, H., Barka, A., et al. (2000). The
1083 seismotectonics of the Marmara region (Turkey): results from a microseismic experiment.
1084 *Tectonophysics*, 316(1), 1–17. [https://doi.org/10.1016/S0040-1951\(99\)00253-X](https://doi.org/10.1016/S0040-1951(99)00253-X)
- 1085 Heisinger, B., Lal, D., Jull, A., Kubik, P., Ivy-Ochs, S., Knie, K., & Nolte, E. (2002a),

- 1086 Production of selected cosmogenic radionuclides by muons: 2. capture of negative muons. *Earth*
1087 *and Planetary Science Letters*, 200(3), 357 – 369. <https://doi.org/10.1016/S0012->
1088 821X(02)00641-6
- 1089 Heisinger, B., Lal, D., Jull, A., Kubik, P., Ivy-Ochs, S., Neumaier, S., Knie, K., Lazarev, V., &
1090 Nolte, E. (2002b). Production of selected cosmogenic radionuclides by muons: 1. fast muons.
1091 *Earth and Planetary Science Letters*, 200(3), 345 – 355. <https://doi.org/10.1016/S0012->
1092 821X(02)00640-4
- 1093 Hidy, A. J., Gosse, J. C., Pederson, J. L., Mattern, J. P., & Finkel, R. C. (2010). A geologically
1094 constrained Monte Carlo approach to modeling exposure ages from profiles of cosmogenic
1095 nuclides: An example from Lees Ferry, Arizona. *Geochemistry, Geophysics, Geosystems*, 11(9),
1096 Q0AA10. <https://doi.org/10.1029/2010GC003084>
- 1097 Honkura, Y. & Isikara, A. M. (1991). Multidisciplinary research on fault activity in the western
1098 part of the North Anatolian Fault Zone. *Tectonophysics*, 193(4), 347–357.
1099 [https://doi.org/10.1016/0040-1951\(91\)90343-Q](https://doi.org/10.1016/0040-1951(91)90343-Q)
- 1100 Hubert-Ferrari, A., Barka, A., Jacques, E., Nalbant, S. S., Meyer, B., Armijo, R., et al. (2000).
1101 Seismic hazard in the Marmara Sea region following the 17 August 1999 Izmit earthquake.
1102 *Nature*, 404(6775), 269–273. <https://doi.org/10.1038/35005054>
- 1103 Hunter, J. D. (2007). Matplotlib: A 2D graphics environment. *Computing in Science &*
1104 *Engineering*, 9, 90–95. <https://doi.org/10.1109/MCSE.2007.55>
- 1105 Ikeda, Y. (1988). Recent activity of the Iznik-Mekece fault at Corak Stream, east of Iznik. In
1106 Honkura, Y. & Isikara, A. M. (Eds.), *Multidisciplinary research on fault activity in the western*
1107 *part of the North Anatolian Fault Zone* (pp. 15–27). Tokyo: Institute of Technology.

- 1108 Ikeda, Y. (1988). Recent activity of the Iznik-Mekece fault at Corak Stream, east of Iznik. In
1109 Honkura, Y. & Isikara, A. M. (Eds.), *Multidisciplinary research on fault activity in the western*
1110 *part of the North Anatolian Fault Zone* (pp. 15–27). Tokyo: Institute of Technology.
- 1111 Ikeda, Y., Herece, E., Sugai, T., & Isikara, A. M. (1991). Postglacial crustal deformation
1112 associated with slip on the western part of the North Anatolian Fault Zone in the Iznik Lake
1113 Basin, Turkey. *Bulletin of the Department of Geography University of Tokyo*, 23, 13–23.
- 1114 Ikeda, Y., Suzuki, Y., & Herece, E. (1989). Late Holocene activity of the North Anatolian fault
1115 zone in the Orhangazi plain, northwestern Turkey. In Honkura, Y. & Isikara, A. M. (Eds.),
1116 *Multidisciplinary research on fault activity in the western part of the North Anatolian fault zone*
1117 (Vol. 2, pp. 16–30). Tokyo: Institute of Technology.
- 1118 Ikeda, Y., Suzuki, Y., Herece, E., Saroglu, F., Isikara, A. M., & Honkura, Y. (1991). Geological
1119 evidence for the last two faulting events on the north Anatolian Fault zone in the Mudurnu
1120 Valley, western Turkey. *Tectonophysics*, 193(4), 335-345. [https://doi.org/10.1016/0040-](https://doi.org/10.1016/0040-1951(91)90342-P)
1121 [1951\(91\)90342-P](https://doi.org/10.1016/0040-1951(91)90342-P)
- 1122 King., G., Klinger, Y., Bowman, D., & Tapponnier, P. (2005). Slip-Partitioned Surface Breaks
1123 for the M_w 7.8 2001 Kokoxili Earthquake, China. *Bulletin of the Seismological Society of*
1124 *America*, 95(2), 731-738. doi: 10.1785/0120040101
- 1125 Klinger, Y. (2010). Relation between continental strike-slip earthquake segmentation and
1126 thickness of the crust. *Journal of Geophysical Research: Solid Earth*, 115, B07306.
- 1127 Klinger, Y., Etchebes, M., Tapponnier, P., & Narteau, C. (2011). Characteristic slip for five great
1128 earthquakes along the Fuyun fault in China. *Nature Geoscience*, 4(6), 389–392.
1129 <https://doi.org/10.1038/ngeo1158>

- 1130 Klinger, Y., Sieh, K., Altunel, E., Akoglu, A., Barka, A., Dawson, T., et al. (2003).
1131 Palaeoseismic Evidence of Characteristic Slip on the Western Segment of the North Anatolian
1132 Fault, Turkey. *Bulletin of the Seismological Society of America*, 93(6), 2317-2332.
1133 <https://doi.org/10.1785/0120010270>
- 1134 Klinger, Y., Xu, X., Tapponnier, P., Van der Woerd, J., Lasserre, C., & King, G. (2005). High-
1135 Resolution Satellite Imagery Mapping of the Surface Rupture and Slip Distribution of the M_w
1136 ~7.8, 14 November 2001 Kokoxili Earthquake, Kunlun Fault, Northern Tibet, China. *Bulletin of*
1137 *the Seismological Society of America*, 95(5), 1970-1987. <http://dx.doi.org/10.1785/0120040233>
- 1138 Koçyigit, A. (1988). Tectonic setting of the Geyve Basin: age and total displacement of the
1139 Geyve Fault Zone. *Journal of Pure and Applied Sciences*, 21, 81–104.
- 1140 Koçyigit, A. & Özacar, A. A. (2003). Extensional neotectonic regime through the NE edge of the
1141 outer Isparta Angle, SW Turkey: new field and seismic data. *Turkish Journal of Earth Sciences*,
1142 12(1), 67–90.
- 1143 Kürçer, A., Chatzipetros, A., Tutkun, S. Z., Pavlides, S., Özkan Ates, & Valkaniotis, S. (2008).
1144 The Yenice–Gönen active fault (NW Turkey): Active tectonics and palaeoseismology.
1145 *Tectonophysics*, 453(1), 263 – 275. <https://doi.org/10.1016/j.tecto.2007.07.010>
- 1146 Kurtz, R., Klinger, Y., Ferry, M., & Ritz, J. F. (2018). Horizontal surface-slip distribution
1147 through several seismic cycles: The Eastern Bogd fault, Gobi-Altai, Mongolia. *Tectonophysics*,
1148 734-735, 167-182. <https://doi.org/10.1016/j.tecto.2018.03.011>
- 1149 Le Béon, M., Klinger, Y., Al-Qaryouti, M., Mériaux, A. S., Finkel, R., C., Elia, A., et al. (2010).
1150 Early Holocene and Late Pleistocene slip rates of the southern Dead Sea Fault determined from
1151 ^{10}Be cosmogenic dating of offset alluvial deposits. *Journal of Geophysical Research: Solid*

- 1152 *Earth*, 115, B11414, doi:10.1029/2009JB007198.
- 1153 Lefevre, M., Klinger, Y., Al-Qaryouti, M., Le Béon, M., & Moumani, K. (2018). Slip deficit and
1154 temporal clustering along the Dead Sea fault from palaeoseismological investigations. *Scientific*
1155 *Reports*, 8, doi:10.1038/s41598-018-22627-9.
- 1156 Le Pichon, X., Imren, C., Rangin, C., Sengör, A. M. C., & Siyako, M. (2014). The South
1157 Marmara Fault. *International Journal of Earth Sciences*, 103(1), 219–231.
1158 <https://doi.org/10.1007/s00531-013-0950-0>
- 1159 Lifton, N. (2016). Implications of two Holocene time dependent geomagnetic models for
1160 cosmogenic nuclide production rate scaling. *Earth and Planetary Science Letters*, 433, 257-268.
1161 <https://doi.org/10.1016/j.epsl.2015.11.006>
- 1162 Lifton, N. A., Sato, T., & Dunai, T. J. (2014). Scaling in situ cosmogenic nuclide production
1163 rates using analytical approximations to atmospheric cosmic-ray fluxes. *Earth and Planetary*
1164 *Science Letters*, 386, 149-160. <https://doi.org/10.1016/j.epsl.2013.10.052>
- 1165 Lin, Z., Liu-Zeng, J., Weldon II, R. J., Tian, J., Ding, C., & Du, Y. (2020). Modeling repeated
1166 coseismic slip to identify and characterize individual earthquakes from geomorphic offsets on
1167 strike-slip faults. *Earth and Planetary Science Letters*, 545, 116313.
1168 <https://doi.org/10.1016/j.epsl.2020.116313>
- 1169 Liu-Zeng, J., Klinger, Y., Sieh, K., Rubin, C., & Seitz, G. (2006). Serial ruptures of the San
1170 Andreas fault, Carrizo Plain, California, revealed by three-dimensional excavations. *Journal of*
1171 *Geophysical Research*, 111, B02306.
- 1172 Lozos, J. C. (2016). A case for historic joint rupture of the San Andreas and San Jacinto faults.
1173 *Science Advances*, 2(3), e1500621. <https://doi.org/10.1126/sciadv.1500621>

- 1174 Manighetti, I., Perrin, C., Dominguez, S., Garambois, S., Gaudemer, Y., Malavieille, J., et al.
1175 (2015). Recovering paleoearthquake slip record in a highly dynamic alluvial and tectonic region
1176 (Hope Fault, New Zealand) from airborne lidar. *Journal of Geophysical Research: Solid Earth*,
1177 120(6), 4484–4509. <https://doi.org/10.1002/2014JB011787>
- 1178 Manighetti, I., Perrin, C., Gaudemer, Y., Dominguez, S., Stewart, N., Malavieille, J., Garambois,
1179 S. (2020). Repeated giant earthquakes on the Wairarapa fault, New Zealand, revealed by Lidar-
1180 based paleoseismology. *Scientific Reports*, 10, 2124. [https://doi.org/10.1038/s41598-020-59229-](https://doi.org/10.1038/s41598-020-59229-3)
1181 3
- 1182 Martin, L. C. P., Blard, P.-H., Balco, G., Lavé, J., Delunel, R., Lifton, N., Laurent, V. (2017).
1183 The CREp program and the ICE-D production rate calibration database: A fully parameterizable
1184 and updated online tool to compute cosmic-ray exposure ages. *Quaternary Geochronology*, 38,
1185 25-49. <https://doi.org/10.1016/j.quageo.2016.11.006>
- 1186 McClusky, S., Balassanian, S., Barka, A., Demir, C., Ergintav, S., Georgiev, I., et al. (2000).
1187 Global Positioning System constraints on plate kinematics and dynamics in the eastern
1188 Mediterranean and Caucasus. *Journal of Geophysical Research: Solid Earth*, 105(B3), 5695–
1189 5719.
- 1190 McGill, S. F., & Rubin, C. M. (1999). Surficial slip distribution on the central Emerson fault
1191 during the June 28, 1992, Landers earthquake, California. *Journal of Geophysical Research:*
1192 *Solid Earth*, 104(B3), 4811–4833.
- 1193 McGill, S. F., & Sieh, K. (1991). Surficial offsets on the Central and Eastern Garlock Fault
1194 associated with prehistoric earthquakes. *Journal of Geophysical Research*, 96(B13), 21597-
1195 21621.

- 1196 Meade, B. J., Hager, B. H., McClusky, S. C., Reilinger, R. E., Ergintav, S., Lenk, O., et al.
1197 (2002). Estimates of seismic potential in the Marmara Sea region from block models of secular
1198 deformation constrained by Global Positioning System measurements. *Bulletin of the*
1199 *Seismological Society of America*, 92(1), 208–215. <http://dx.doi.org/10.1785/0120000837>
- 1200 Merchel, S. & Herpers, U. (1999). An update on radiochemical separation techniques for the
1201 determination of long-lived radionuclides via accelerator mass spectrometry. *Radiochimica Acta*,
1202 84(4), 215-219. <https://doi.org/10.1524/ract.1999.84.4.215>
- 1203 Moratto, Z. M., Broxton, M. J., Beyer, R. A., Lundy, M., & Husmann, K. (2010). *Ames Stereo*
1204 *Pipeline, NASA's Open Source Automated Stereogrammetry Software*. Paper presented at the
1205 41th Lunar and Planetary Science Conference, Woodlands, TX.
- 1206 Onderdonk, N., McGill, S., & Rockwell, T. (2018). A 3700 yr paleoseismic record from the
1207 northern San Jacinto fault and implications for joint rupture of the San Jacinto and San Andreas
1208 faults. *Geosphere*, 14(6), 2447-2468. <https://doi.org/10.1130/GES01687.1>
- 1209 Özalp, S., Emre, Ö., & Dogan, A. (2013). The segment structure of southern branch of the North
1210 Anatolian Fault and palaeoseismological behaviour of the Gemlik fault, NW Anatolia. *Bulletin of*
1211 *MTA*, 147, 1–17.
- 1212 Öztürk, K., Yaltirak, C., & Alpar, B. (2009). The relationship between the tectonic setting of the
1213 Lake Iznik Basin and the Middle Strand of the North Anatolian Fault. *Turkish Journal of Earth*
1214 *Sciences*, 18, 209–224.
- 1215 Palyvos, N., Pantosti, D., Zabci, C., & D'Addezio, G. (2007). Paleoseismological Evidence of
1216 Recent Earthquakes on the 1967 Mudurnu Valley Earthquake Segment of the North Anatolian
1217 Fault Zone. *Bulletin of the Seismological Society of America*, 97(5), 1646-1661.

1218 <https://doi.org/10.1785/0120060049>

1219 Parsons, T., Toda, S., Stein, R. S., Barka, A., & Dieterich, J. H. (2000). Heightened odds of large
1220 earthquakes near Istanbul: An interaction-based probability calculation. *Science*, 288(5466),
1221 661–665. <https://doi.org/10.1126/science.288.5466.661>

1222 Pondard, N., Armijo, R., King, G. C. P., Meyer, B., & Flérit, F. (2007). Fault interactions in the
1223 Sea of Marmara pull-apart (North Anatolian Fault): earthquake clustering and propagating
1224 earthquake sequences. *Geophysical Journal International*, 171, 1185-1197.
1225 <https://doi.org/10.1111/j.1365-246X.2007.03580.x>

1226 Reitman, N. G., Mueller, K. J., Tucker, G. E., Gold, R. D., Briggs, R. W., & Barnhart, K. R.
1227 (2019). Offset channels may not accurately record strike-slip fault displacements: Evidence from
1228 landscape evolution models. *Journal of Geophysical Research: Solid Earth*, 124, 13,427-13,451.

1229 Ren, Z., Zielke, O., & Yu, J. (2018). Active tectonics in 4D high-resolution. *Journal of*
1230 *Structural Geology*, 117, 264-271. <https://doi.org/10.1016/j.jsg.2018.09.015>

1231 Rizza, M., Ritz, J. F., Braucher, R., Vassallo, R., Prentice, C., Mahan, S., et al. (2011). Slip rate
1232 and slip magnitudes of past earthquakes along the Bogd left-lateral strike-slip fault (Mongolia).
1233 *Geophysical Journal International*, 186(3), 897-927. [https://doi.org/10.1111/j.1365-](https://doi.org/10.1111/j.1365-246X.2011.05075.x)
1234 [246X.2011.05075.x](https://doi.org/10.1111/j.1365-246X.2011.05075.x)

1235 Rockwell, T. K., Dawson, T. E., Young Ben-Horin, J., & Seitz, G. (2014). A 21-Event, 4,000
1236 Year History of Surface Ruptures in the Anza Seismic Gap, San Jacinto Fault, and Implications
1237 for Long-term Earthquake Production on a Major Plate Boundary Fault. *Pure and Applied*
1238 *Geophysics*, 172, 1143-1165. <https://doi.org/10.1007/s00024-014-0955-z>

1239 Rockwell, T. K., Lindvall, S., Dawson, T., Langridge, R., Lettis, W., & Klinger, Y. (2002).

- 1240 Lateral Offsets on Surveyed Cultural Features Resulting from the 1999 Izmit and Düzce
1241 Earthquakes, Turkey. *Bulletin of the Seismological Society of America*, 92(1), 79-94.
1242 <https://doi.org/10.1785/0120000809>
- 1243 Rockwell, T., Ragona, D., Seitz, G., Langridge, R., Ersen Aksoy, M., Uçarkus, G., et al. (2009).
1244 Palaeoseismology of the North Anatolian Fault near the Marmara Sea: Implications for fault
1245 segmentation and seismic hazard. In: Reicherter, K., Michetti, A. M., Silva, P. G. (Eds.),
1246 *Palaeoseismology: Historical and Prehistorical Records of Earthquake Ground Effects for*
1247 *Seismic Hazard Assessment, Geological Society Special Publications* (Vol. 316(1), pp. 31-54).
1248 London: The Geological Society. <https://doi.org/10.1144/SP316.3>
- 1249 Scharer, K. M., Salisbury, J. B., Arrowsmith, J. R., & Rockwell, T. K. (2014). Southern San
1250 Andreas Fault Evaluation Field Activity: Approaches to Measuring Small Geomorphic Offsets –
1251 Challenges and Recommendations for Active Fault Studies. *Seismological Research Letters*, 85,
1252 68-76. <https://doi.org/10.1785/0220130108>
- 1253 Schwartz, D. P., & Coppersmith, K. J. (1984). Fault Behavior and Characteristic Earthquakes:
1254 Examples From the Wasatch and San Andreas Fault Zones. *Journal of Geophysical Research*,
1255 89(B7), 5681-5698.
- 1256 Sengör, A. M. C., Grall, C., Imren, C., Le Pichon, X., Görür, N., Henry, P., et al. (2014). The
1257 geometry of the North Anatolian transform fault in the Sea of Marmara and its temporal
1258 evolution: implications for the development of intracontinental transform faults. *Canadian*
1259 *Journal of Earth Sciences*, 51(3), 222–242. <https://doi.org/10.1139/cjes-2013-0160>
- 1260 Shean, D. E., Alexandrov, O., Moratto, Z., Smith, B. E., Joughin, I. R., Porter, C. C., & Morin, P.
1261 J. (2016). An automated, open-source pipeline for mass production of digital elevation models

- 1262 (DEMs) from very high-resolution commercial stereo satellite imagery. *ISPRS Journal of*
1263 *Photogrammetry and Remote Sensing*, 116, 101–117.
1264 <https://doi.org/10.1016/j.isprsjprs.2016.03.012>
- 1265 Sieh, K. E. & Jahns, R. H. (1984). Holocene activity of the San Andreas fault at Wallace Creek,
1266 California. *Geological Society of America Bulletin*, 95(8), 883–896.
1267 [https://doi.org/10.1130/0016-7606\(1984\)95<883:HAOTSA>2.0.CO;2](https://doi.org/10.1130/0016-7606(1984)95<883:HAOTSA>2.0.CO;2)
- 1268 Sipahioglu, S. & Matsuda, T. (1986). Geology and Quaternary fault in the Iznik-Mekece area. In:
1269 Isikara A. M. & Honkura, Y. (Eds.), *Electric and Magnetic Research on Active Faults in the*
1270 *North Anatolian Fault Zone*. (pp. 25-41). Tokyo: Tokyo Inst. Technology.
- 1271 Stein, R. S., Barka, A. A., & Dieterich, J. H. (1997). Progressive failure on the North Anatolian
1272 fault since 1939 by earthquake stress triggering. *Geophysical Journal International*, 128(3), 594–
1273 604. <https://doi.org/10.1111/j.1365-246X.1997.tb05321.x>
- 1274 Straub, C., Kahle, H.-G., & Schindler, C. (1997). GPS and geologic estimates of the tectonic
1275 activity in the Marmara Sea region, NW Anatolia. *Journal of Geophysical Research: Solid*
1276 *Earth*, 102(B12), 27587–27601.
- 1277 Stroeven, A. P., Heyman, J., Fabel, D., Björck, S., Caffee, M. W., Fredin, O., & Harbor, J. M.
1278 (2015). A new Scandinavian reference ¹⁰Be production rate. *Quaternary Geochronology*, 29,
1279 104–115. <https://doi.org/10.1016/j.quageo.2015.06.011>
- 1280 Tsukuda, T., Satake, K., Honkura, Y., Üçer, S. B., & Isikara, A. M. (1988). Low seismicity, low
1281 coda-Q and discontinuities of the upper crust in the vicinity of the Iznik-Mekece fault, the North
1282 Anatolian Fault Zone, Turkey. *Bulletin of Earthquake Research of the Institute University of*
1283 *Tokyo*, 63, 327–348.

- 1284 Uppala, S. M., KÅllberg, P. W., Simmons, A. J., Andrae, U., Bechtold, V. D. C., Fiorino, M., et
1285 al. (2005). The ERA-40 re-analysis. *Quarterly Journal of the Royal Meteorological Society*, 131,
1286 2961-3012. <https://doi.org/10.1256/qj.04.176>
- 1287 van der Woerd, J., Klinger, Y., Sieh, K., Tapponnier, P., Ryerson, F. J., & Mériaux, A. S. (2006).
1288 Long-term slip rate of the southern San Andreas Fault from ^{10}Be - ^{26}Al surface exposure dating of
1289 an offset alluvial fan. *Journal of Geophysical Research*, 111, B04407.
- 1290 Ward, S. N. (1997). Dogtails versus rainbows: synthetic earthquake rupture models as an aid in
1291 interpreting geological data. *Bulletin of the Seismological Society of America*, 87(1), 1422-1441.
- 1292 Wechsler, N., Rockwell, T. K., & Klinger, Y. (2018). Variable slip-rate and slip-per-event on a
1293 plate boundary fault: The Dead Sea fault in northern Israel. *Tectonophysics*, 722, 210-226.
1294 <https://doi.org/10.1016/j.tecto.2017.10.017>
- 1295 Wells, D. L., & Coppersmith, K. J. (1994). New Empirical Relationships among Magnitude,
1296 Rupture Length, Rupture Width, Rupture Area, and Surface Displacement. *Bulletin of the*
1297 *Seismological Society of America*, 84(4), 974-1002.
- 1298 Wesnousky, S. G. (2006). Predicting the endpoints of earthquake ruptures. *Nature*, 444, 358-360.
1299 <https://doi.org/10.1038/nature05275>
- 1300 Yılmaz, Y., Genç, C., Yigitbas, E., Bozcu, M., & Yılmaz, K. (1995). Geological evolution of the
1301 late Mesozoic continental margin of Northwestern Anatolia. *Tectonophysics*, 243(1), 155–171.
1302 [https://doi.org/10.1016/0040-1951\(94\)00196-G](https://doi.org/10.1016/0040-1951(94)00196-G)
- 1303 Yoshioka, T. & Kusçu, I. (1994). Late Holocene faulting events on the Iznik-Mekece fault in the
1304 western part of the North Anatolian fault zone, Turkey. *Bulletin of the Geological Survey of*
1305 *Japan*, 45(11), 677–685.

1306 Zielke, O. (2018). Earthquake Recurrence and the Resolution Potential of Tectono-Geomorphic
1307 Records. *Bulletin of the Seismological Society of America*, 108(3A), 1399-1413.

1308 <https://doi.org/10.1785/0120170241>

1309 Zielke, O., Arrowsmith, J. R., Grant Ludwig, L., & Akçiz, S. O. (2010). Slip in the 1857 and
1310 earlier large earthquakes along the Carrizo Plain, San Andreas Fault. *Science*, 327, 1119-1122.

1311 <https://doi.org/10.1126/science.1182781>

1312 Zielke, O., Arrowsmith, J. R., Grant Ludwig, L., & Akciz, S. O. (2012). High-Resolution
1313 Topography-Derived Offsets along the 1857 Fort Tejon Earthquake Rupture Trace, San Andreas
1314 Fault. *Bulletin of the Seismological Society of America*, 102(3), 1135-1154.

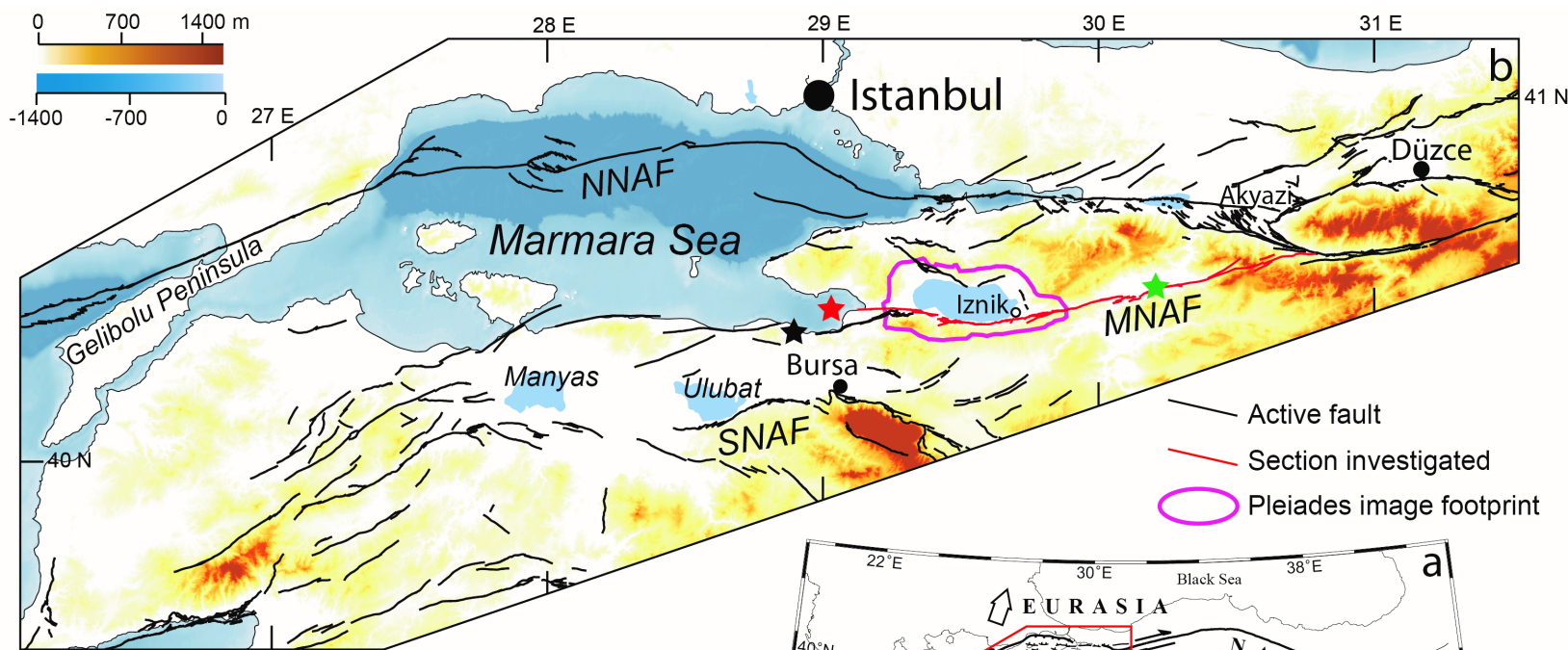
1315 <https://doi.org/10.1785/0120110230>

1316 Zielke, O., Klinger, Y., & Arrowsmith, J. R. (2015). Fault slip and earthquake recurrence along
1317 strike-slip faults - Contributions of high-resolution geomorphic data. *Tectonophysics*, 638, 43–

1318 62. <https://doi.org/10.1016/j.tecto.2014.11.004>

1319

Figure 1.



Slip rate estimates

- ★ 5 ± 2 mm/yr (Ergintav et al., 2014)
- ★ 3.7 ± 0.7 mm/yr (Gasperini et al., 2011)
- ★ 4.9 ± 0.4 mm/yr (Özalp et al., 2013)

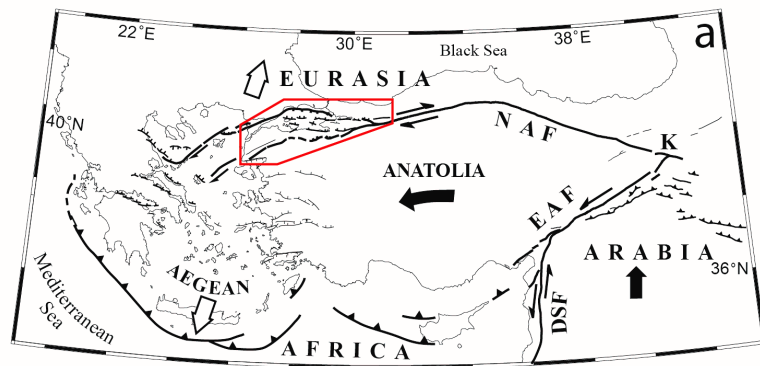


Figure 2.

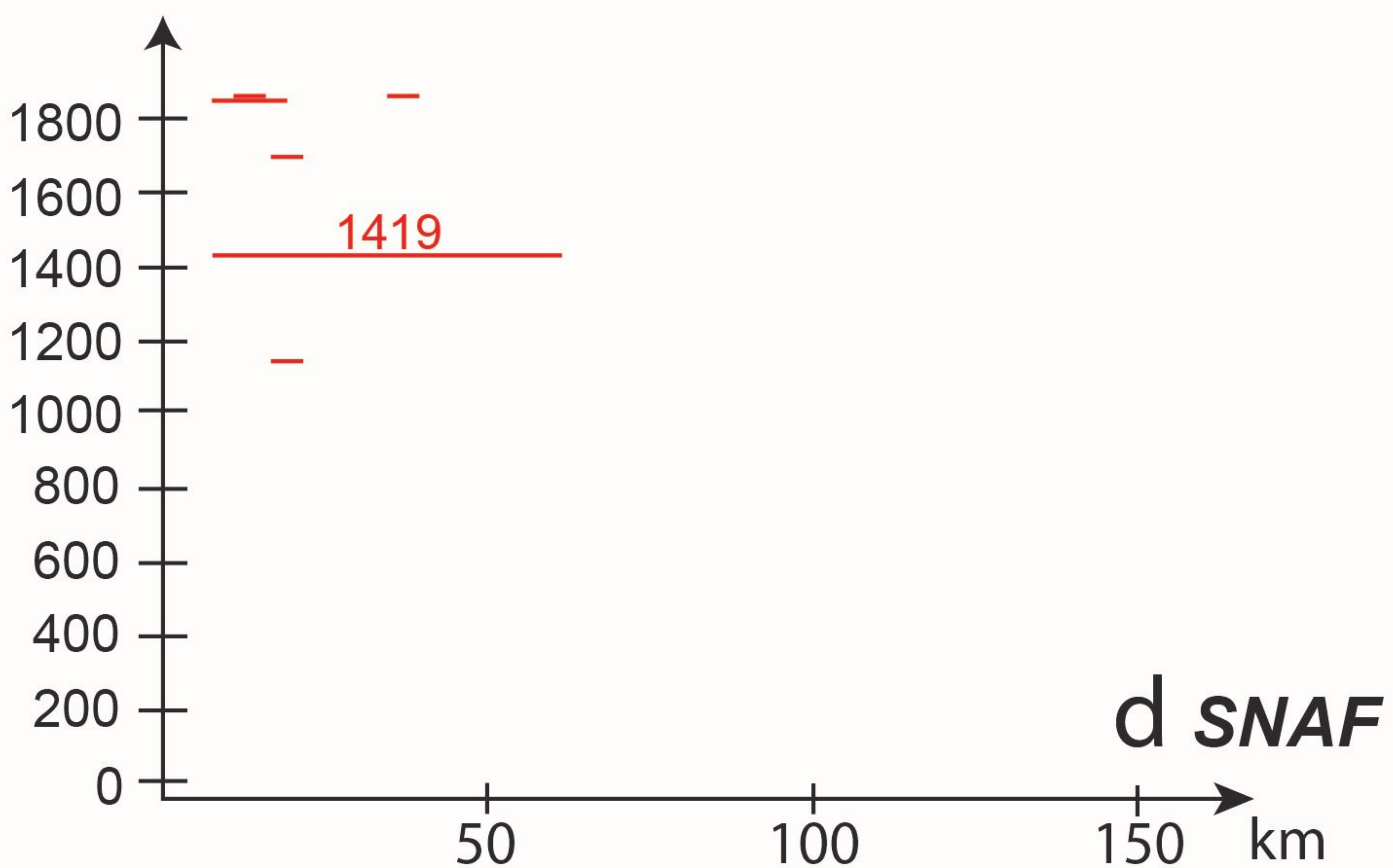
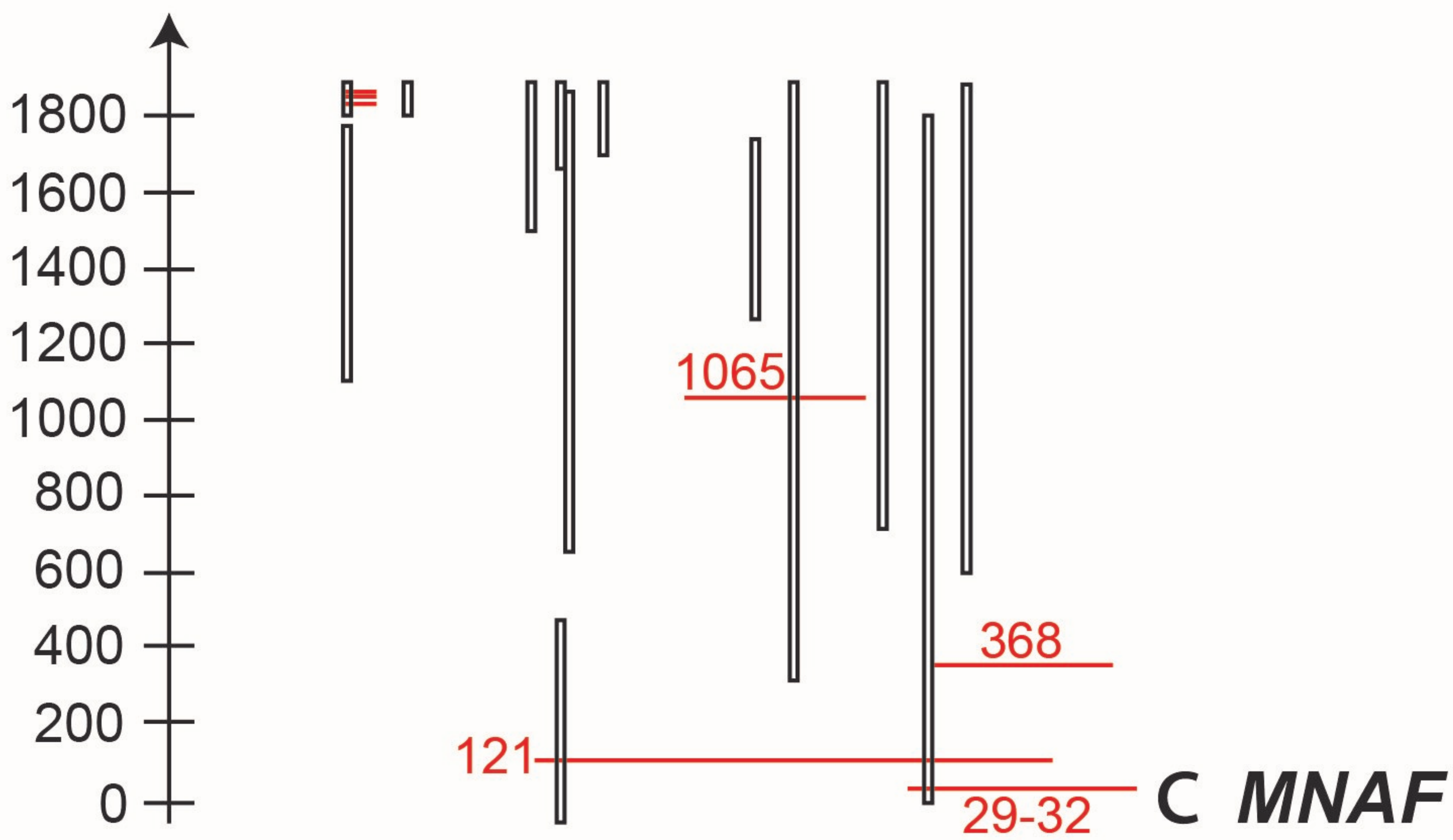
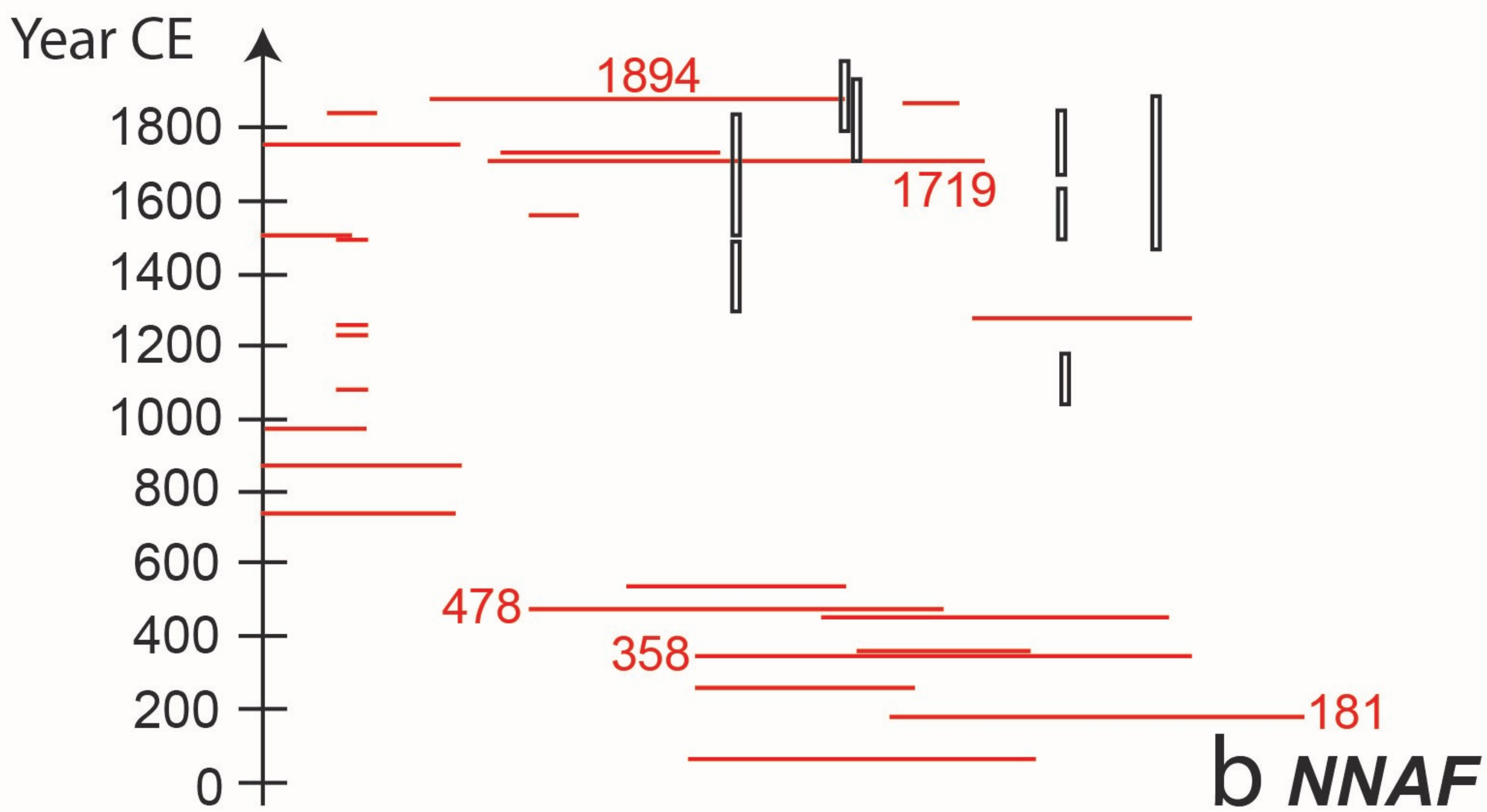
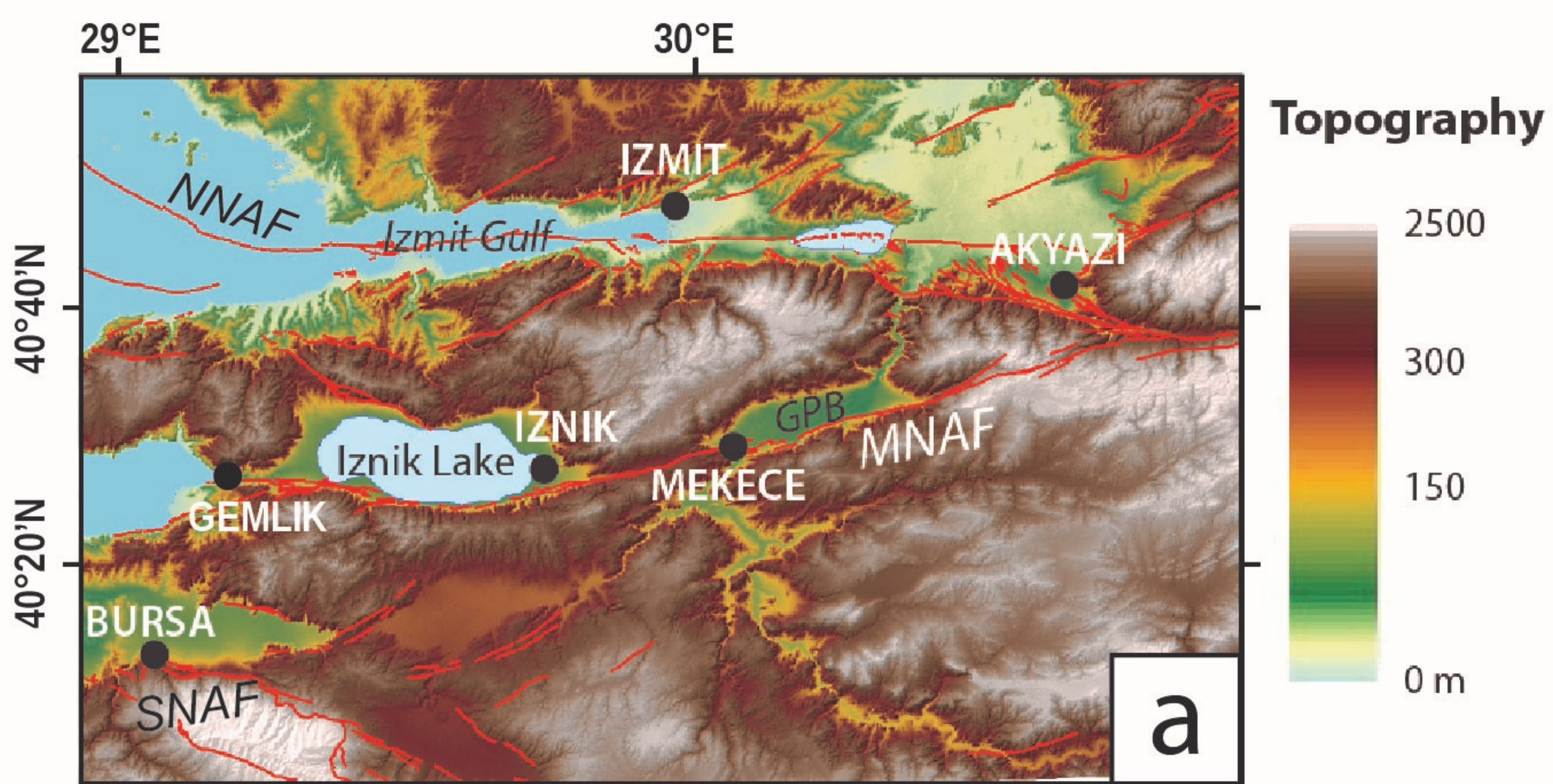


Figure 3.

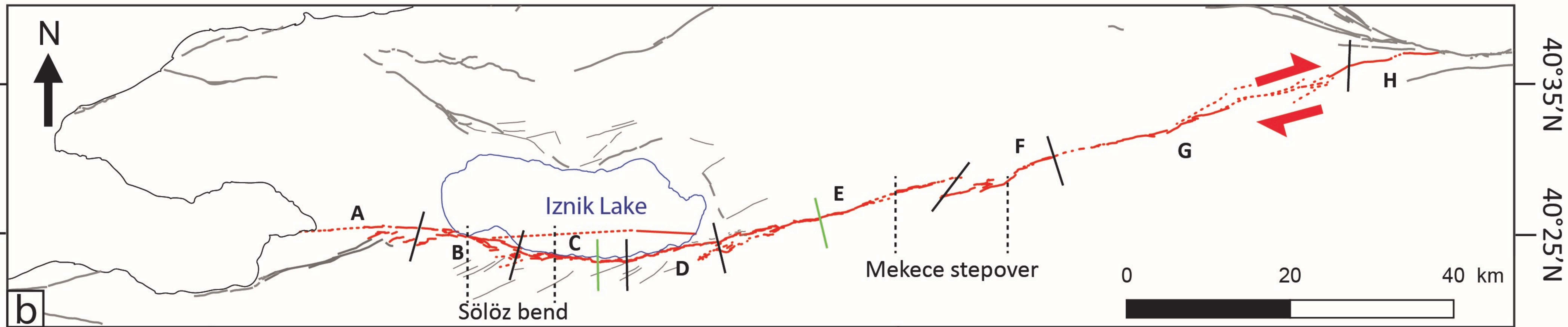
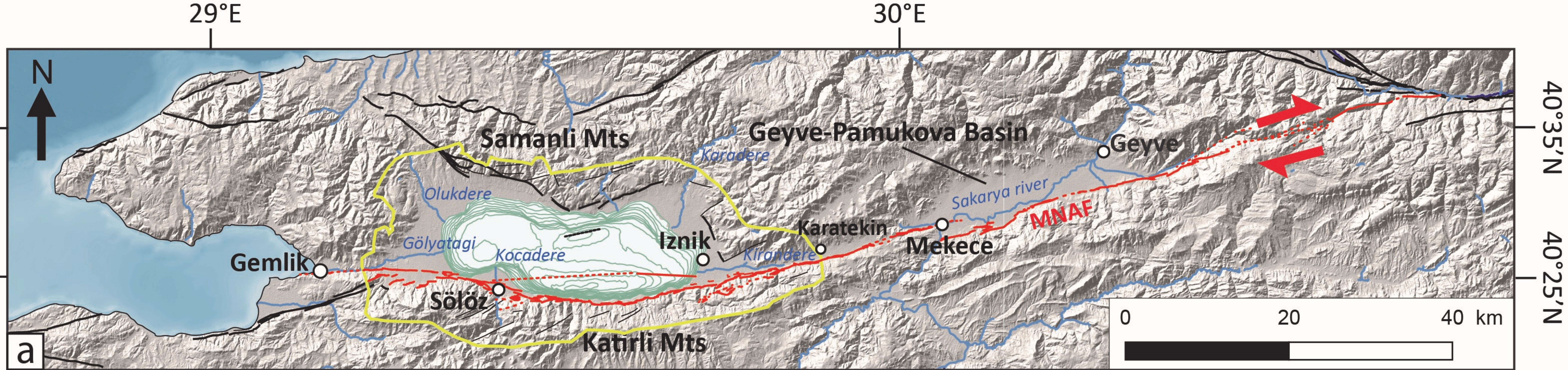


Figure 4.

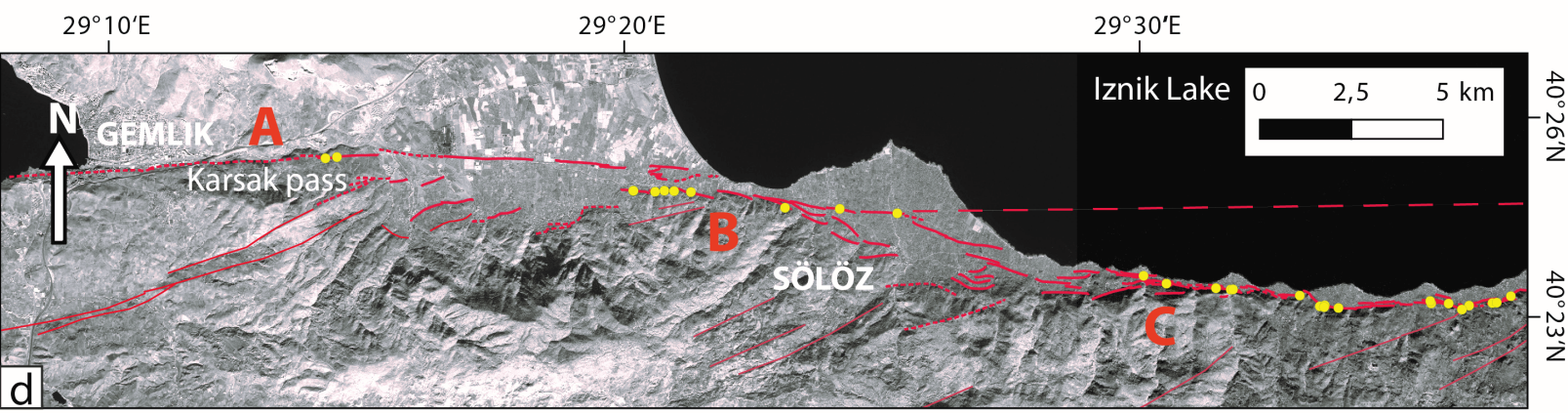
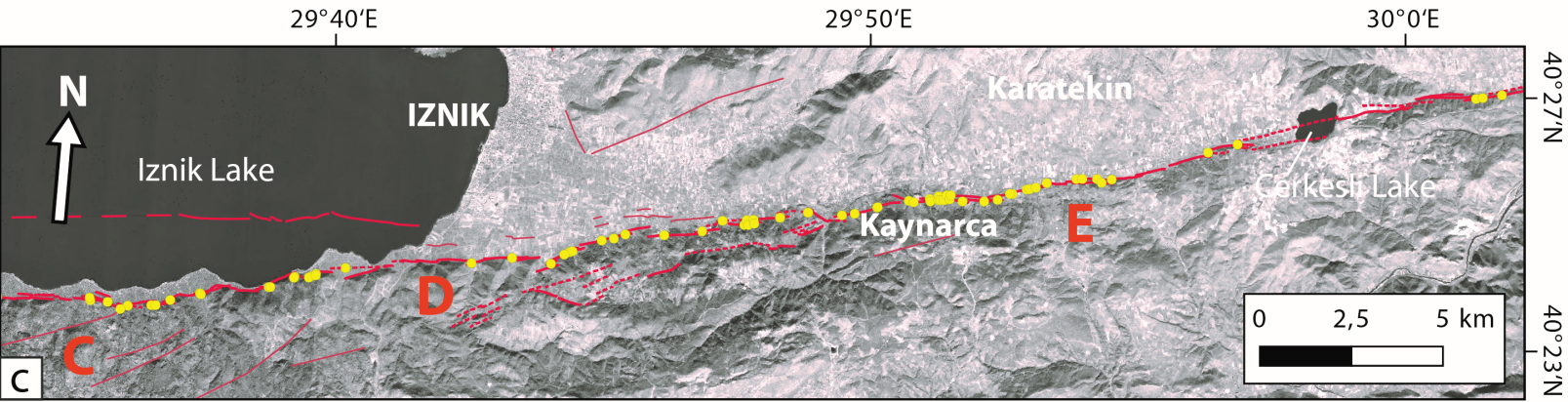
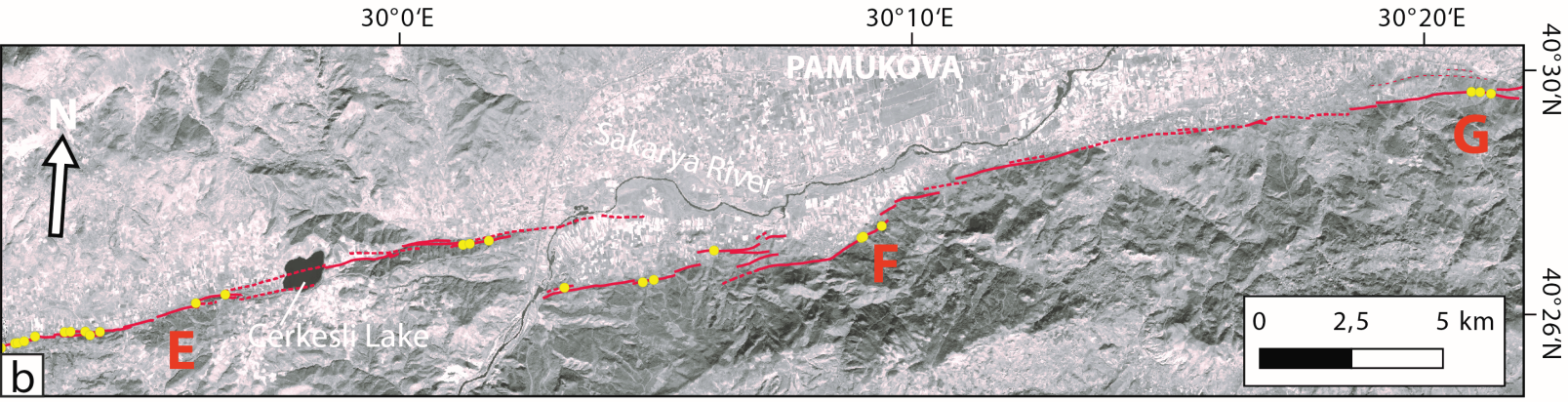
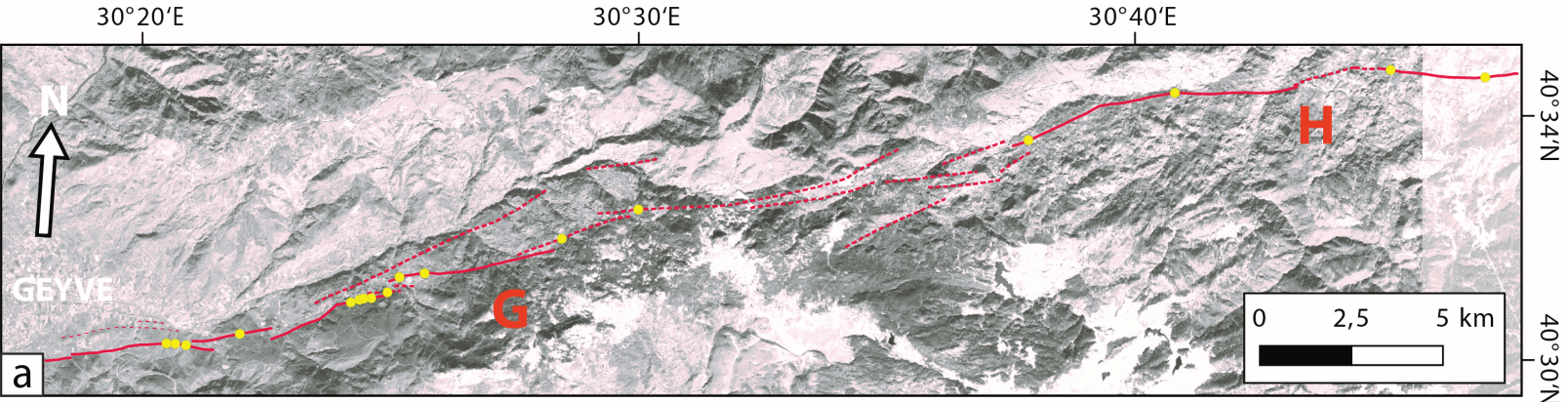


Figure 5.

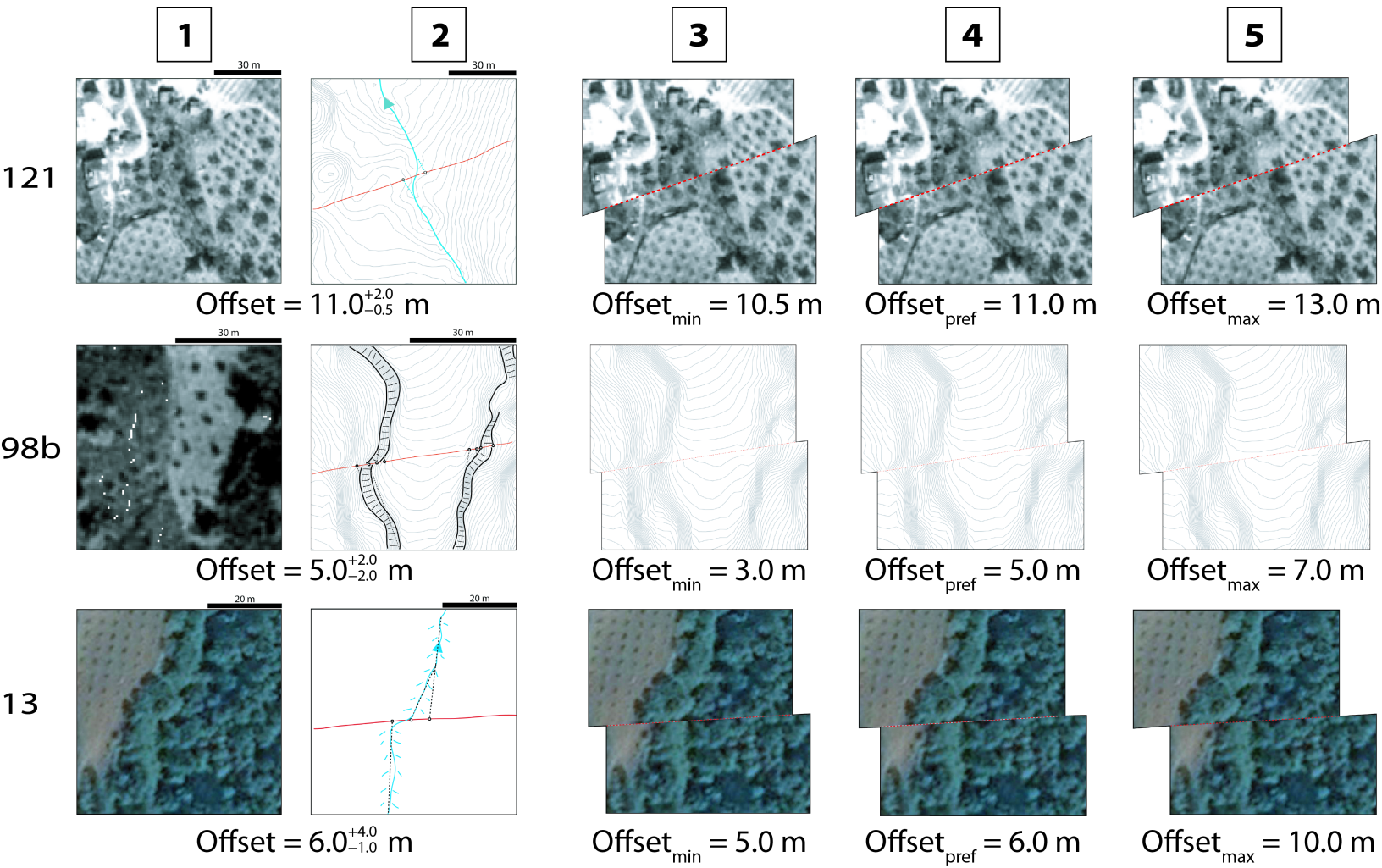


Figure 6.

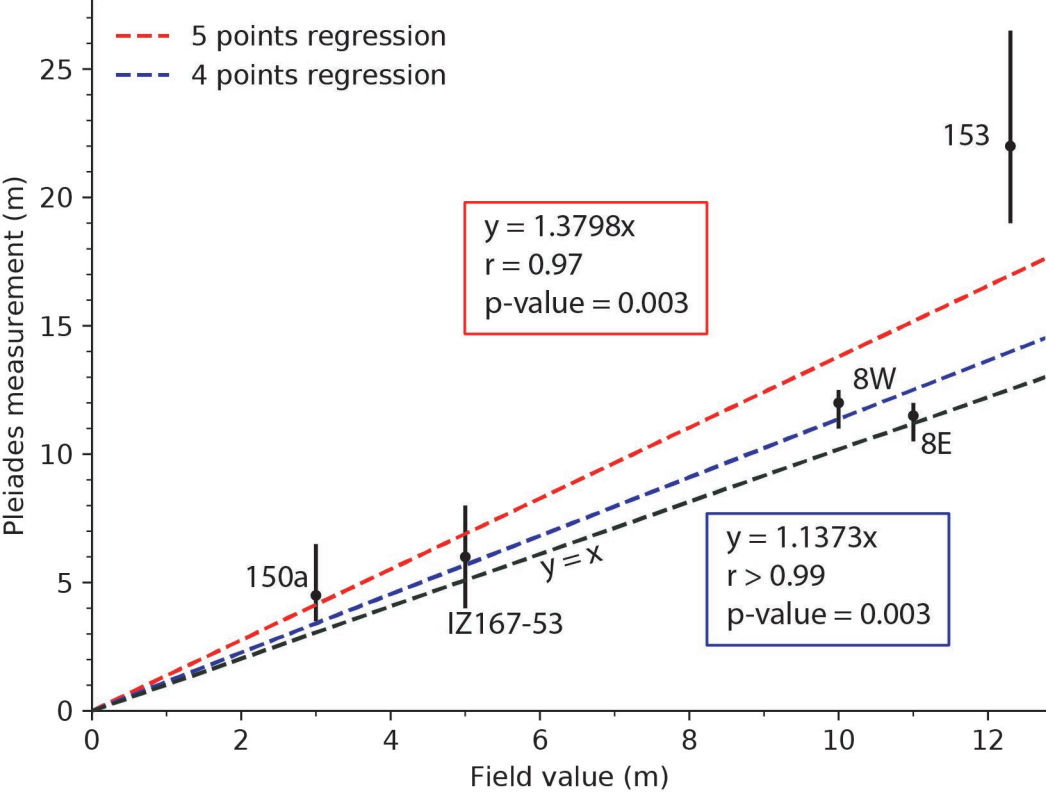


Figure 7.

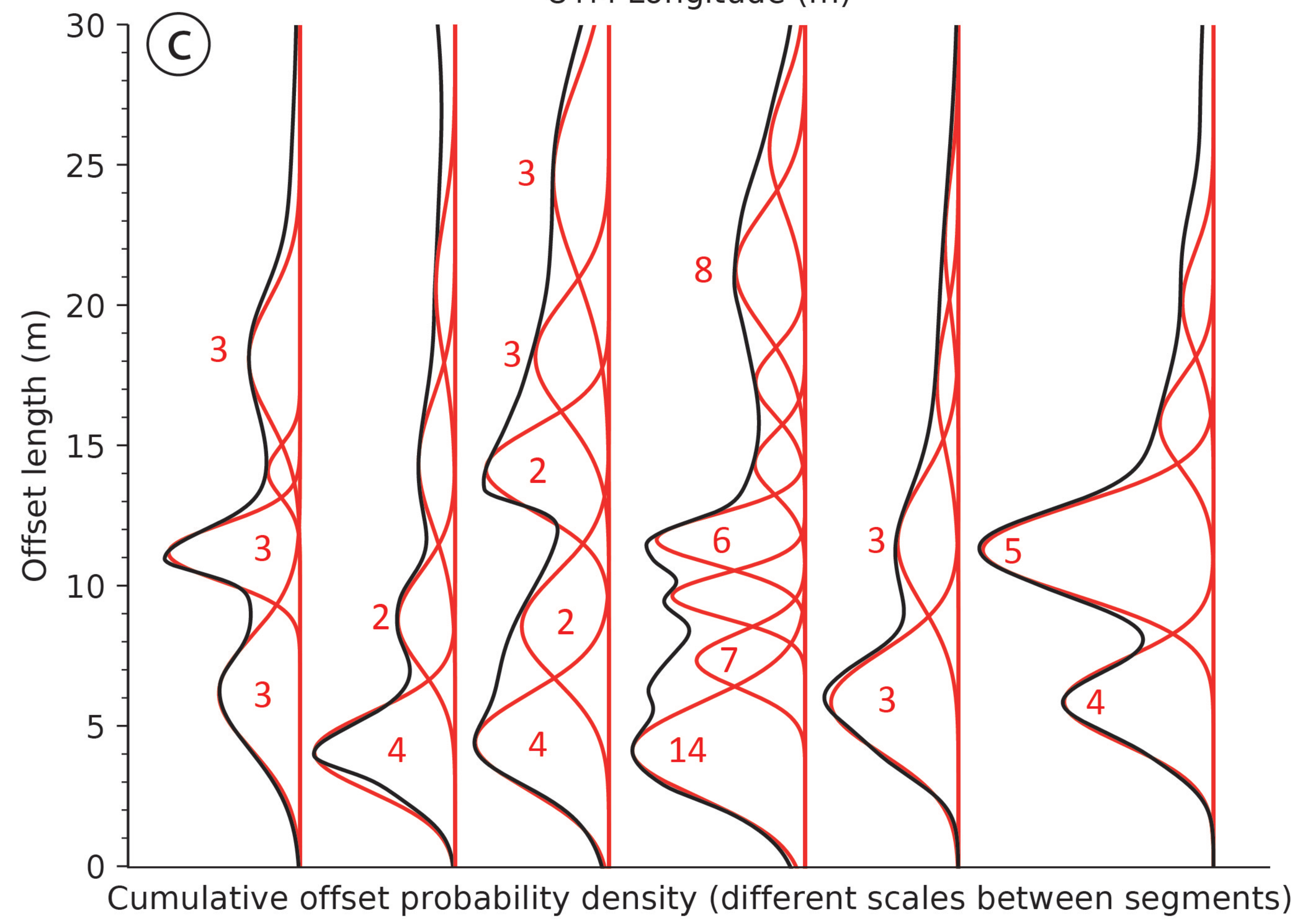
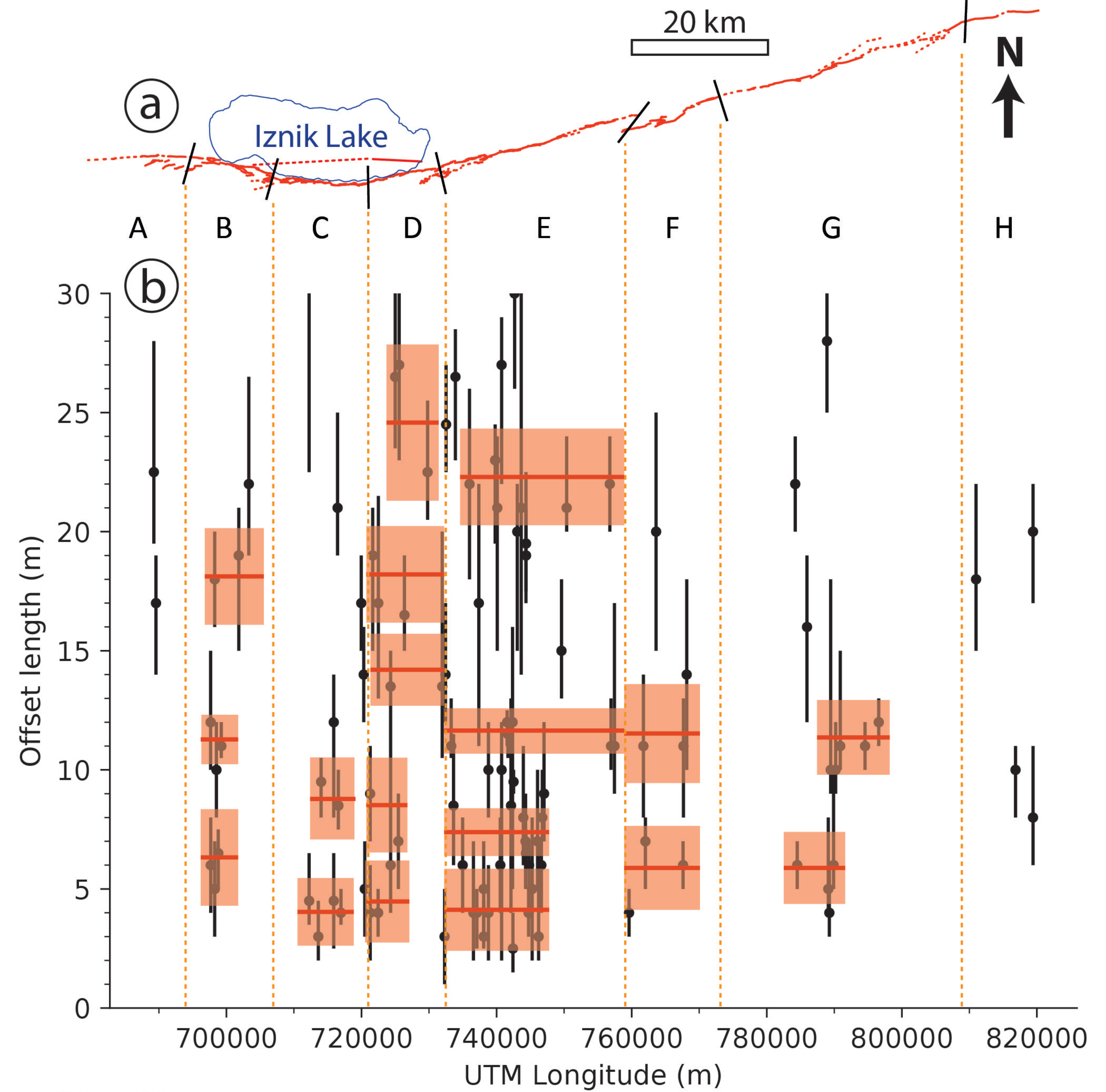


Figure 8.

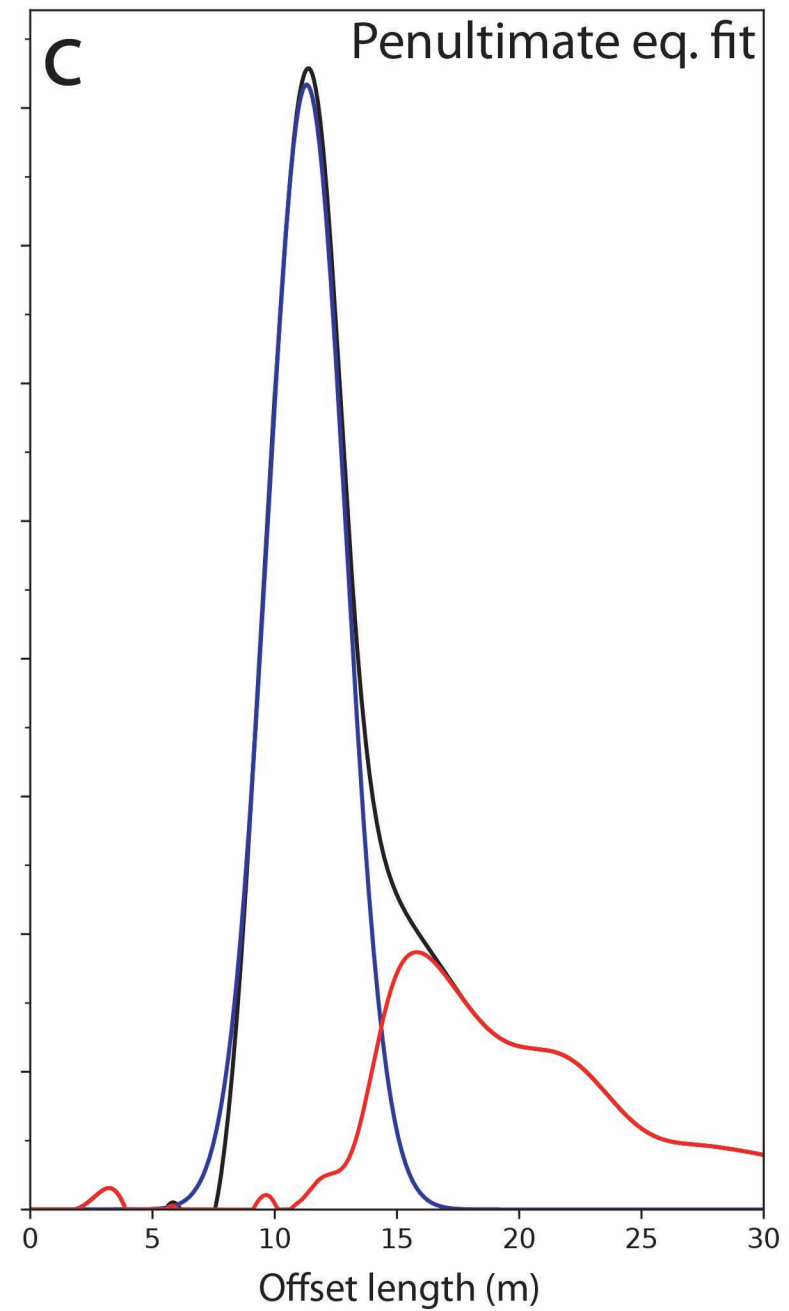
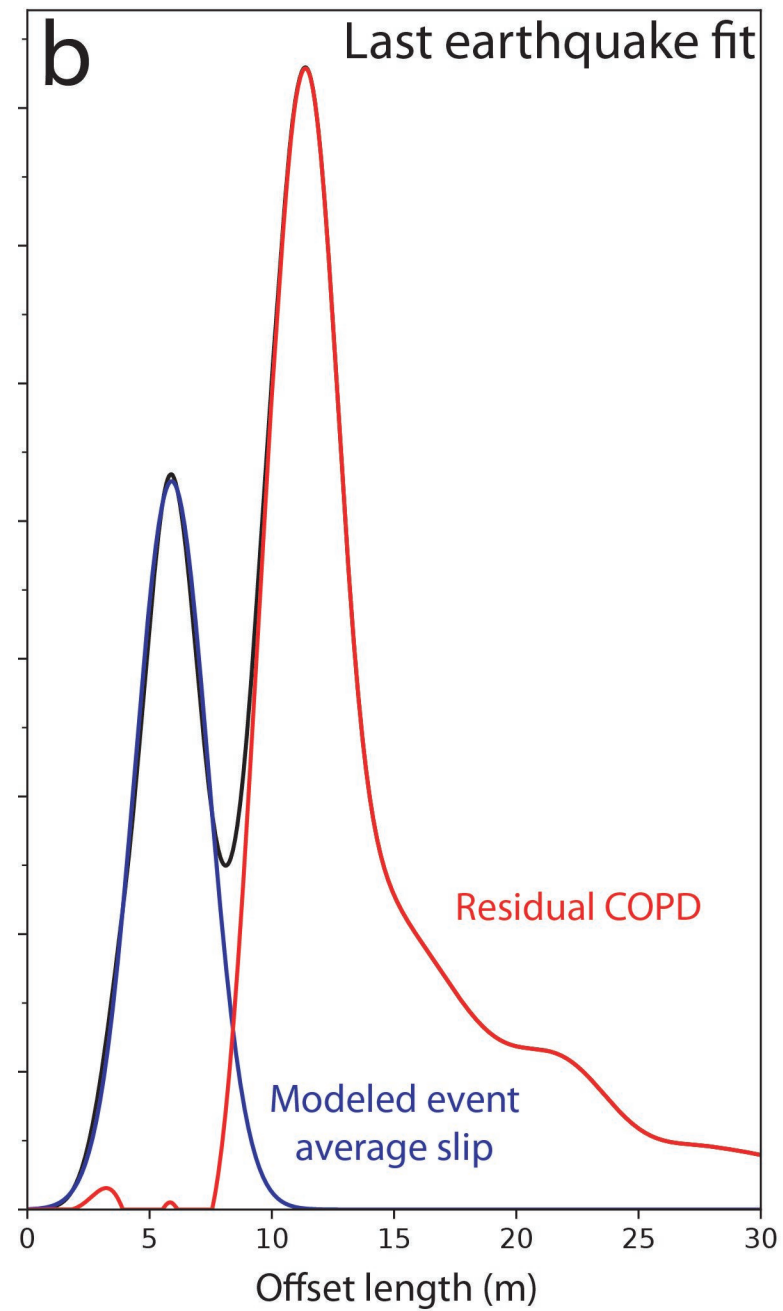
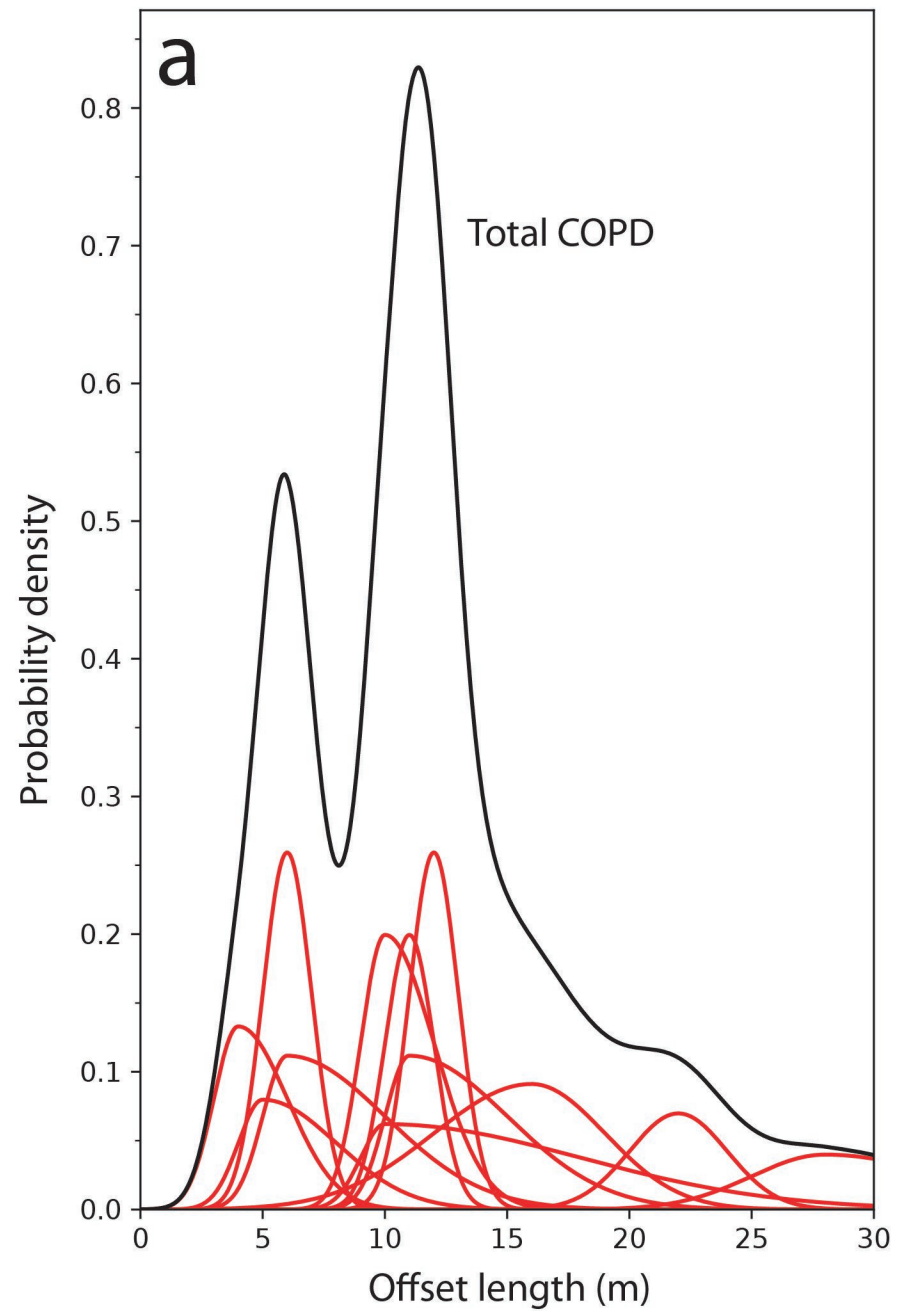


Figure 9.

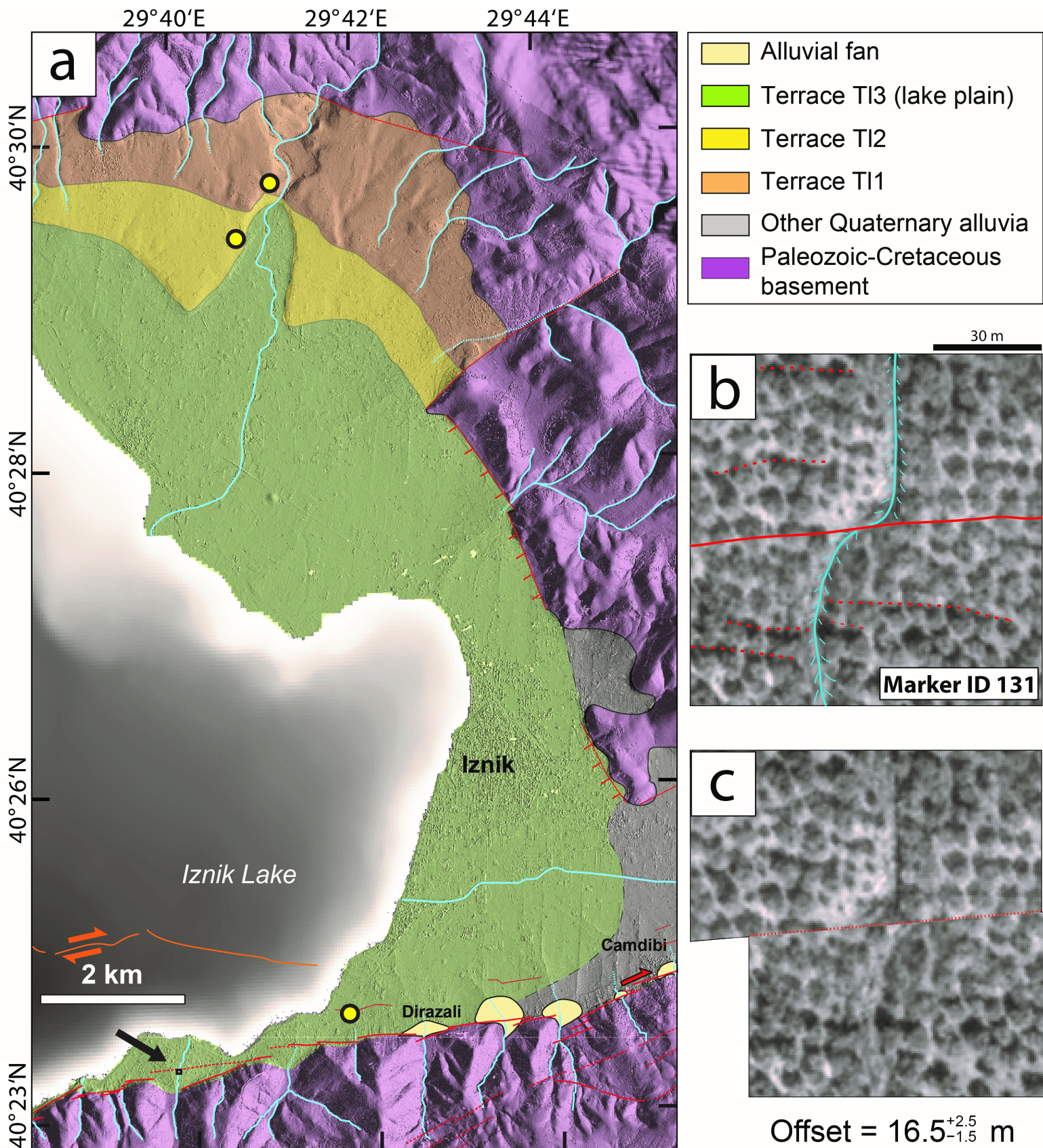
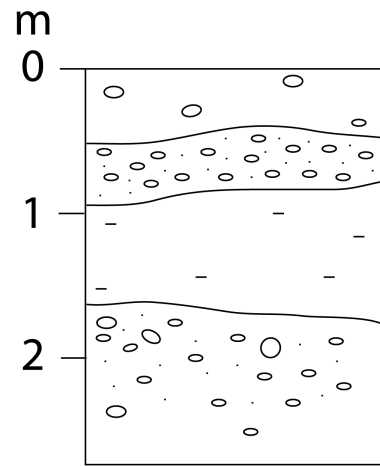


Figure 10.

Schematic log

Lithological description

TI3



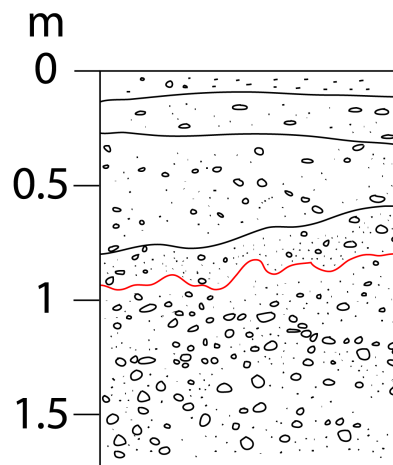
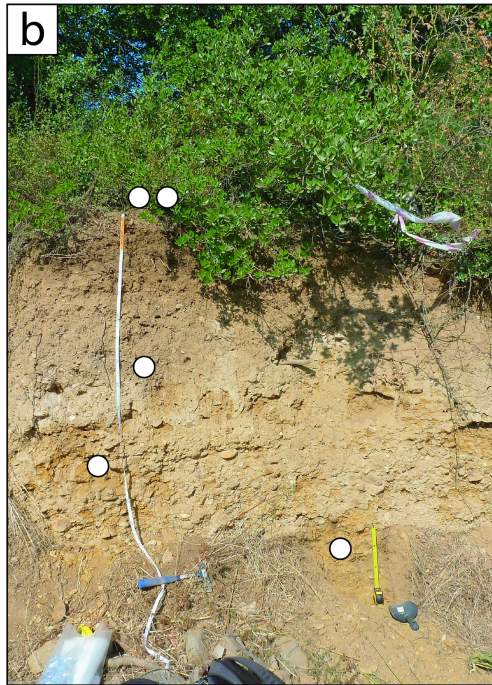
hard, dark brown soil with few, centimetric pebbles

light brown, sandy layer, numerous pebbles

brownish grey, fine layer

coarse layer, heterogeneous unsorted pebbles

TI2



thin brown soil with few gravel

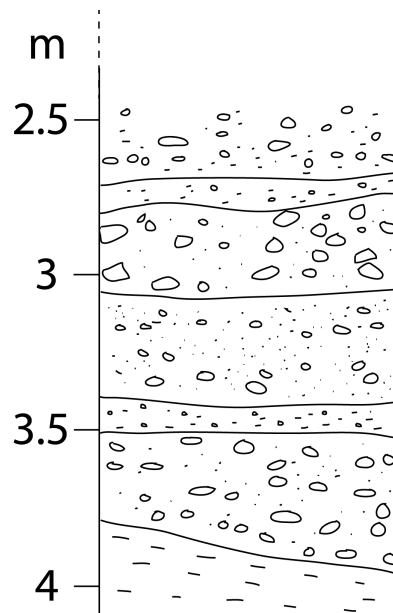
dark brown silty layer with few pebbles

brown sandy layer, homogeneous rounded pebbles

light brown, gravel-rich sandy layer with few pebbles

coarse, orange sandy layer, abundant pebbles and gravel

TI1



sandy layer, gravel and heterogeneous pebbles

fine sandy layer with gravel and few pebbles

coarse sandy layer with large, subrounded pebbles

sandy layer with abundant small pebbles

fine, gravel-rich sandy layer

sandy layer, homogeneous rounded pebbles

very fine silty-sandy layer

Figure 11.

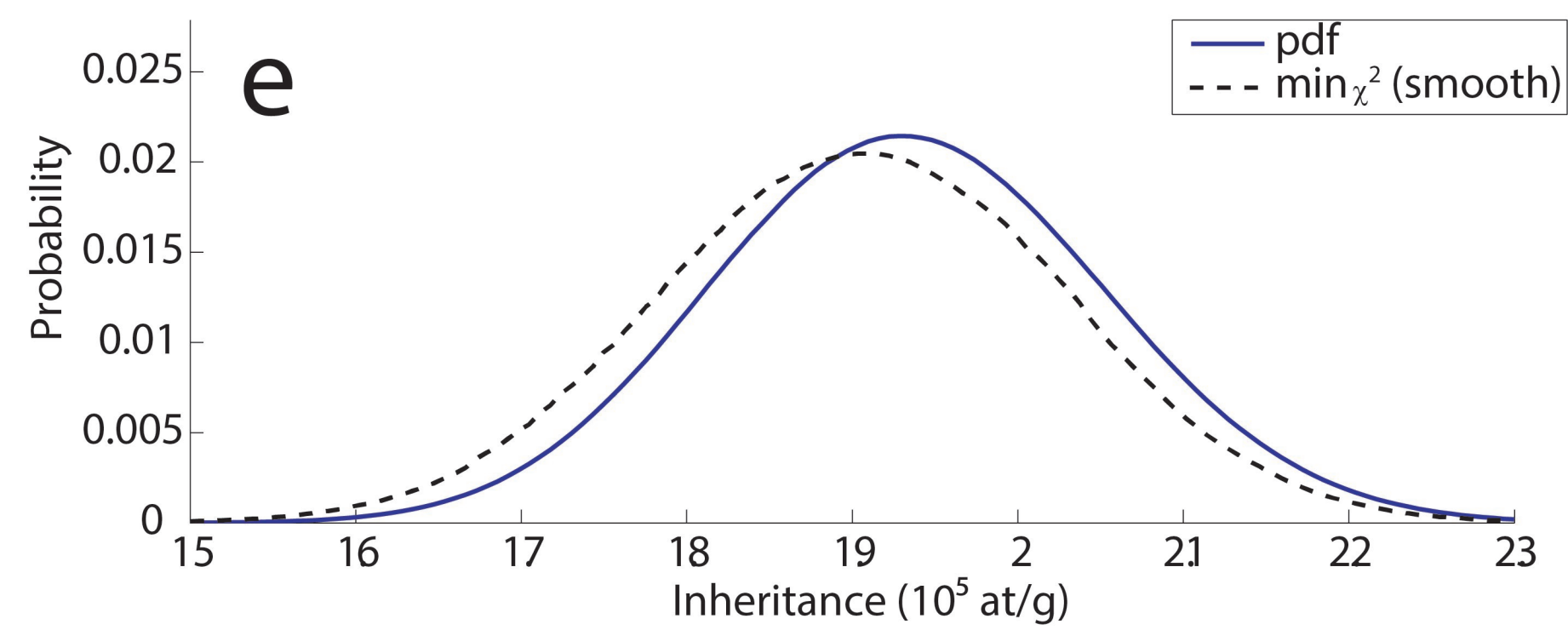
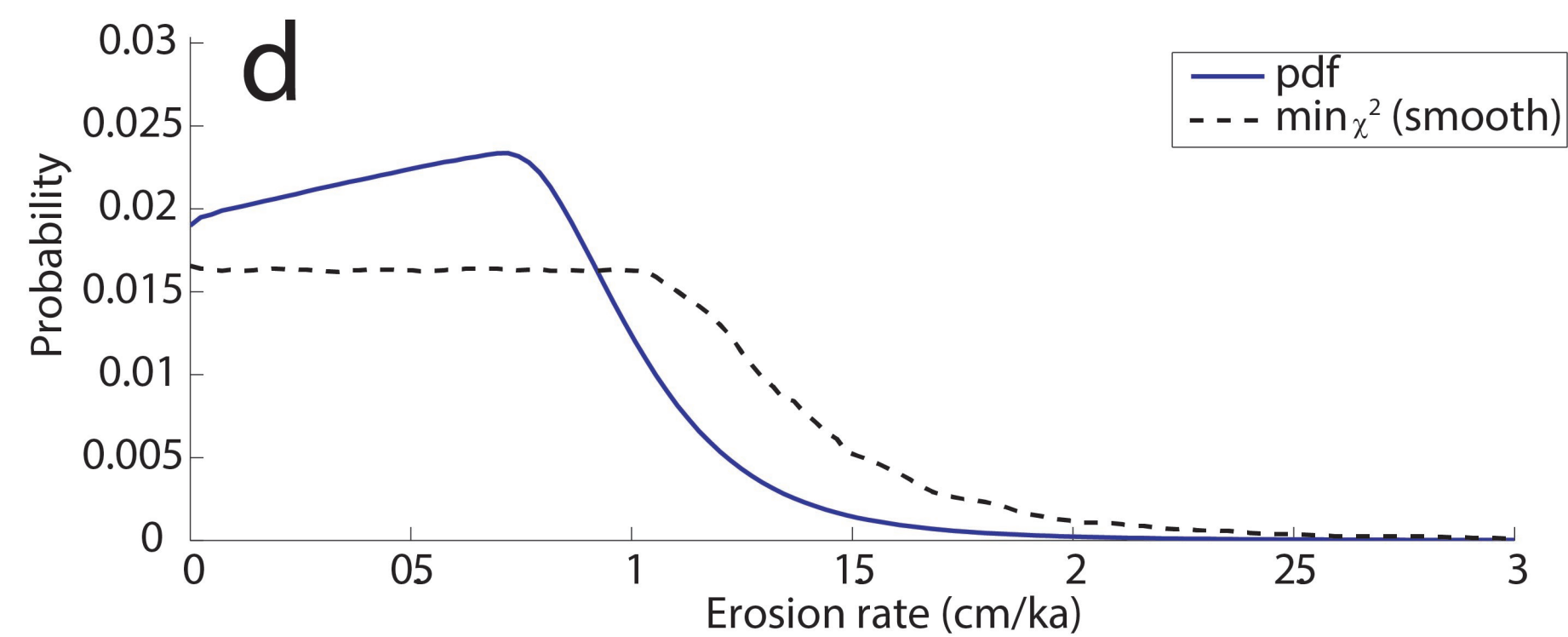
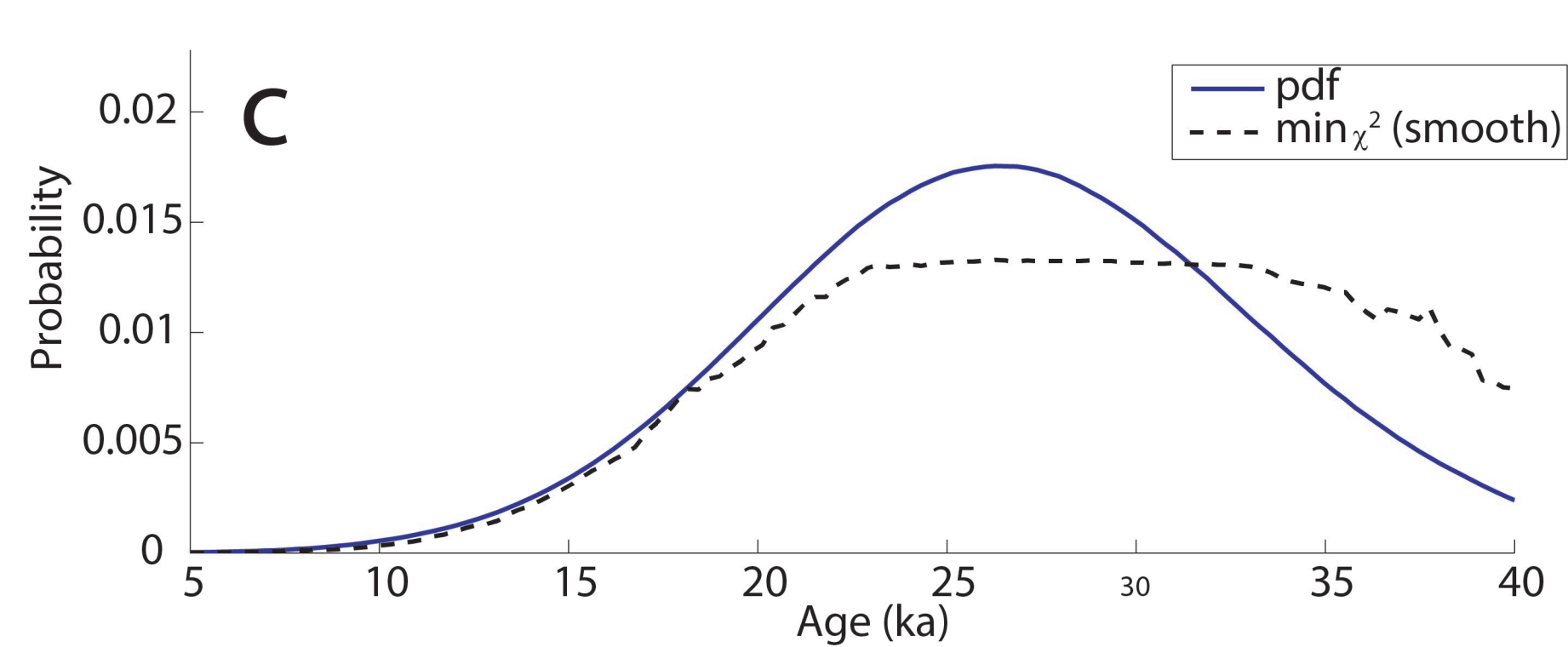
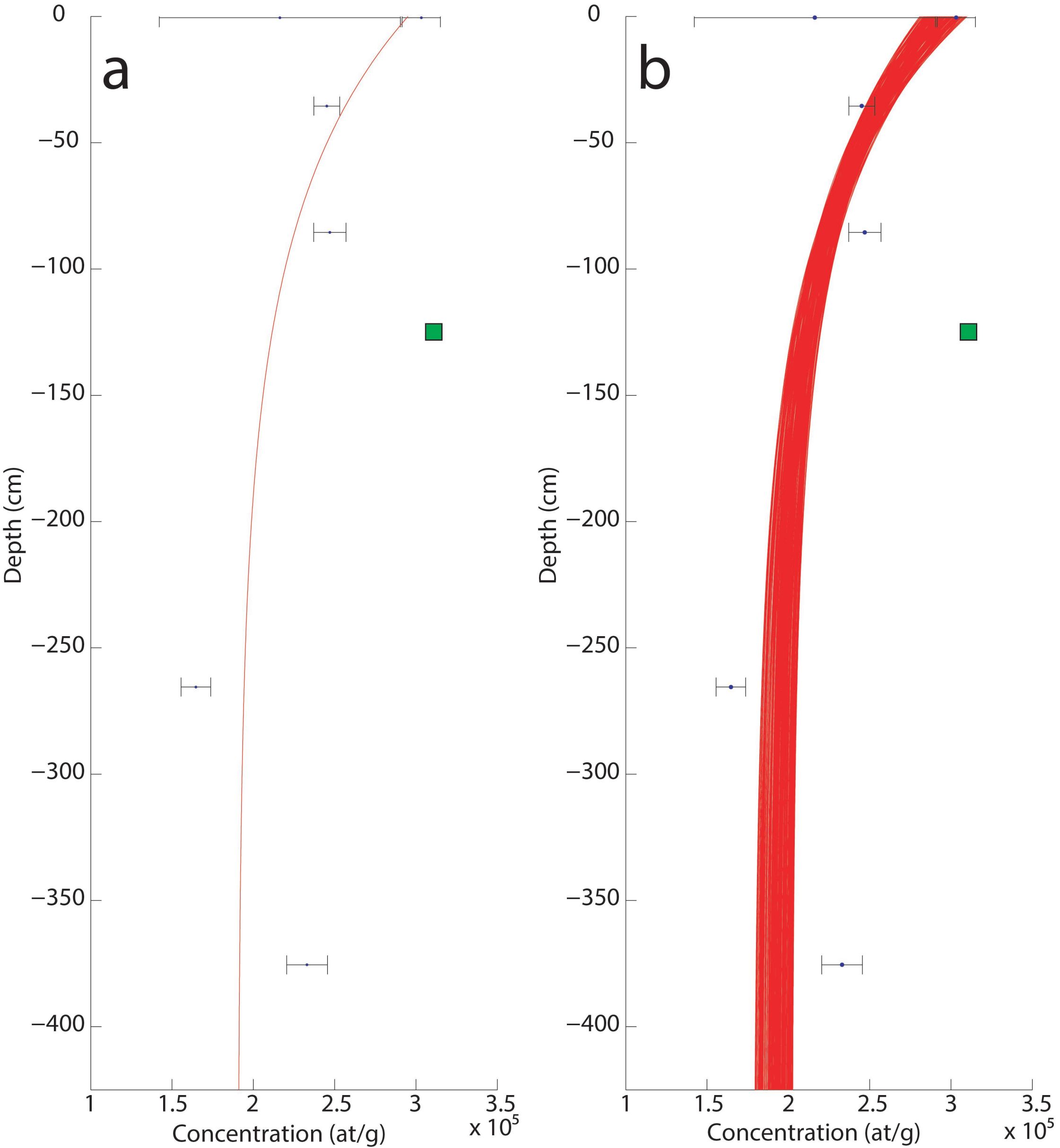


Figure 12.

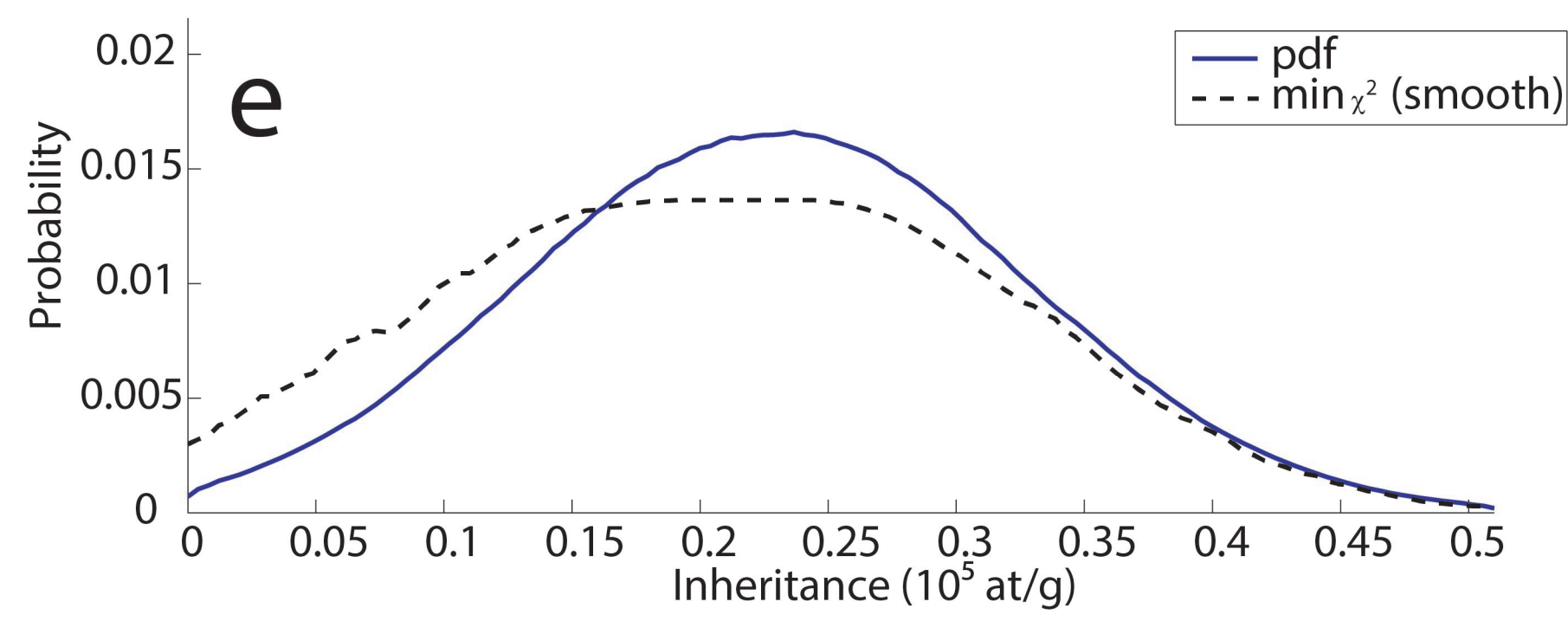
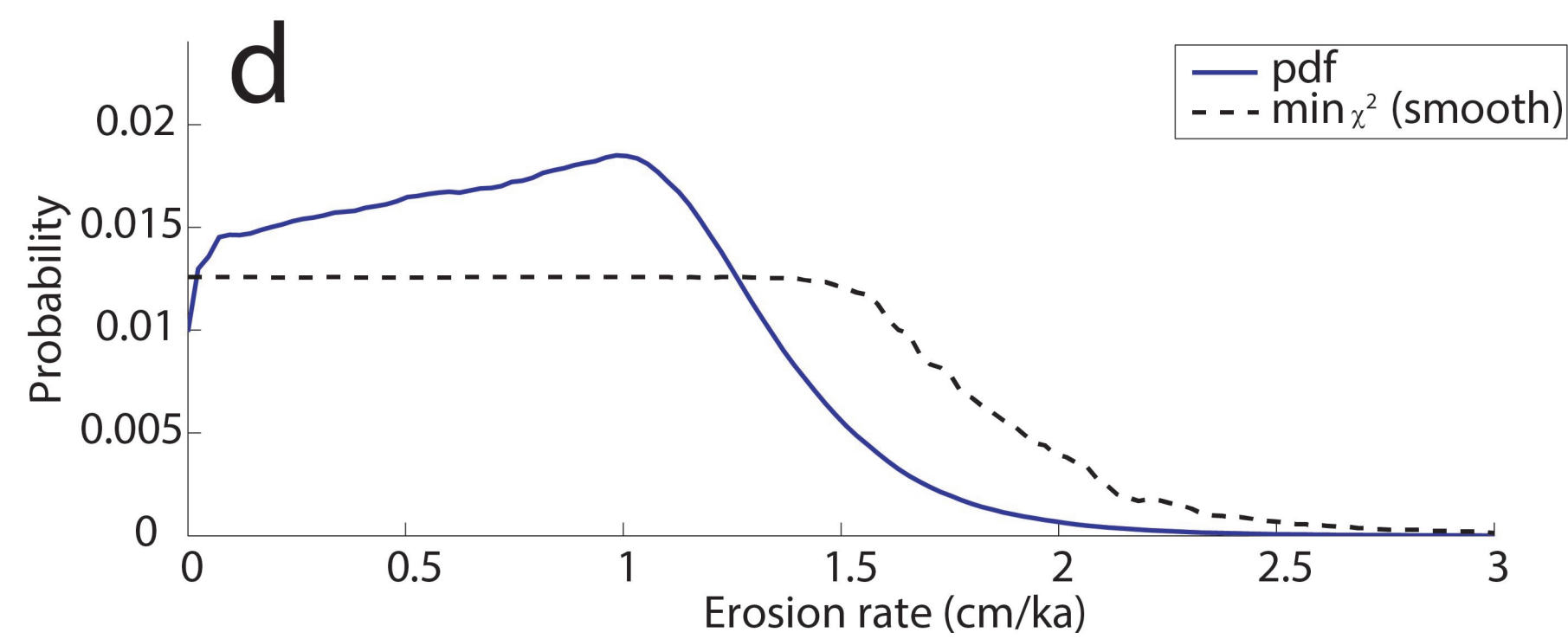
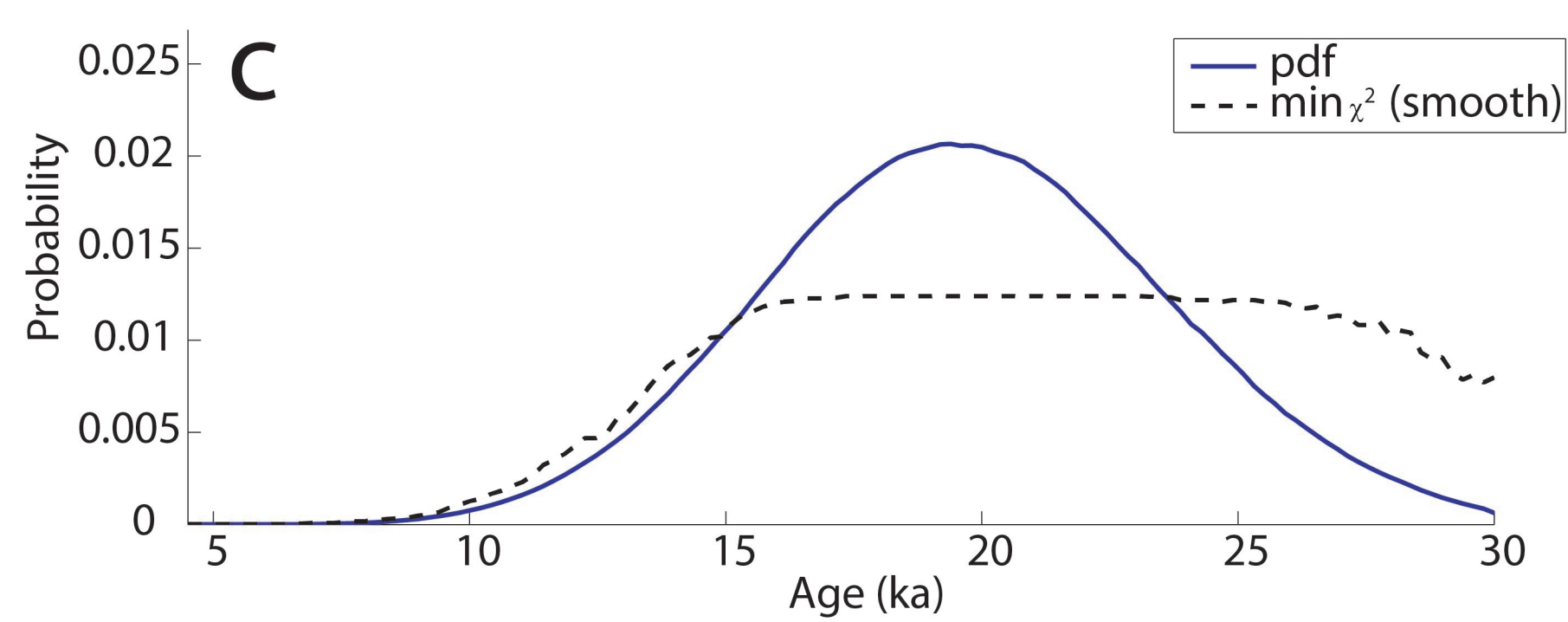
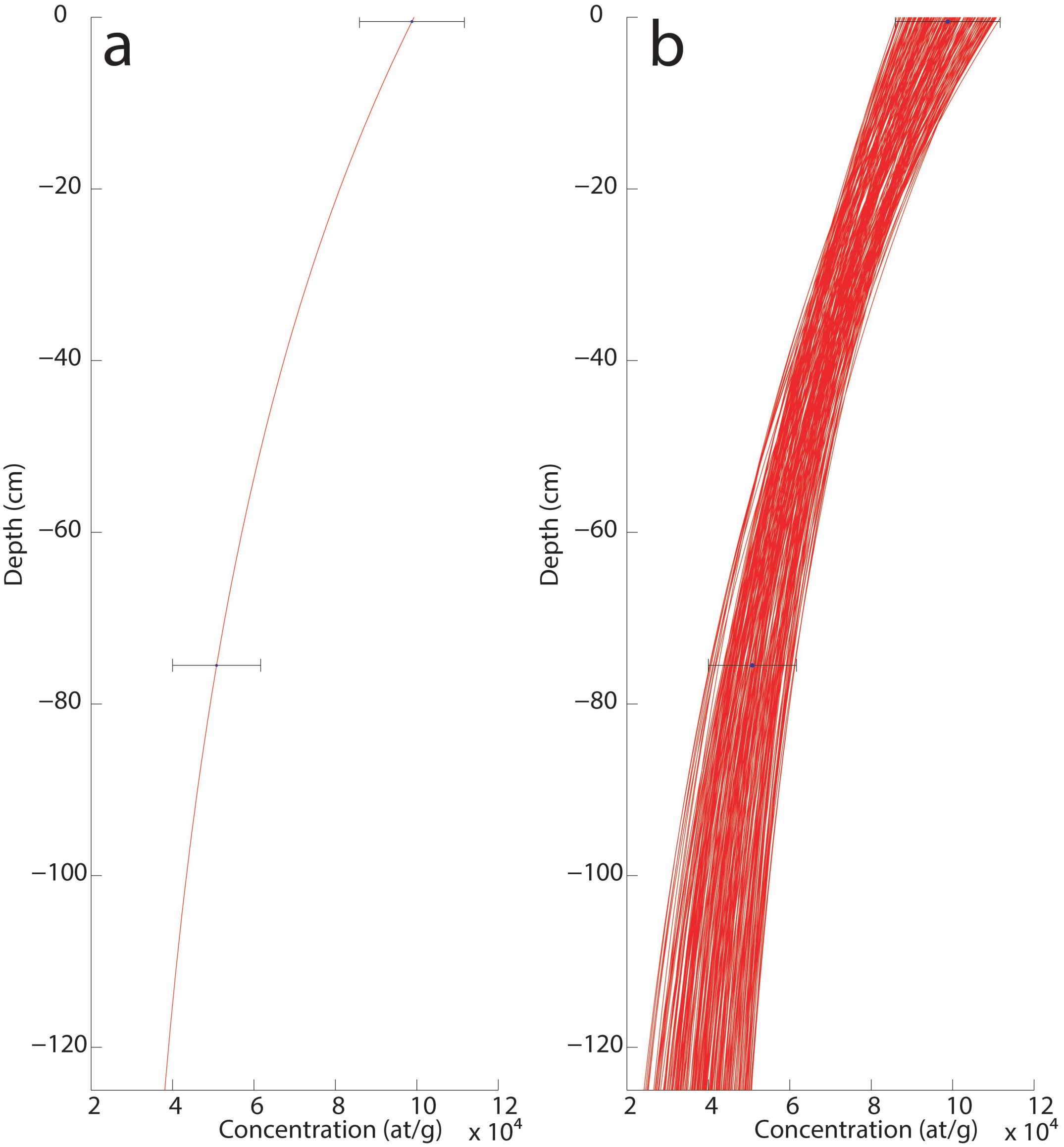


Figure 13.

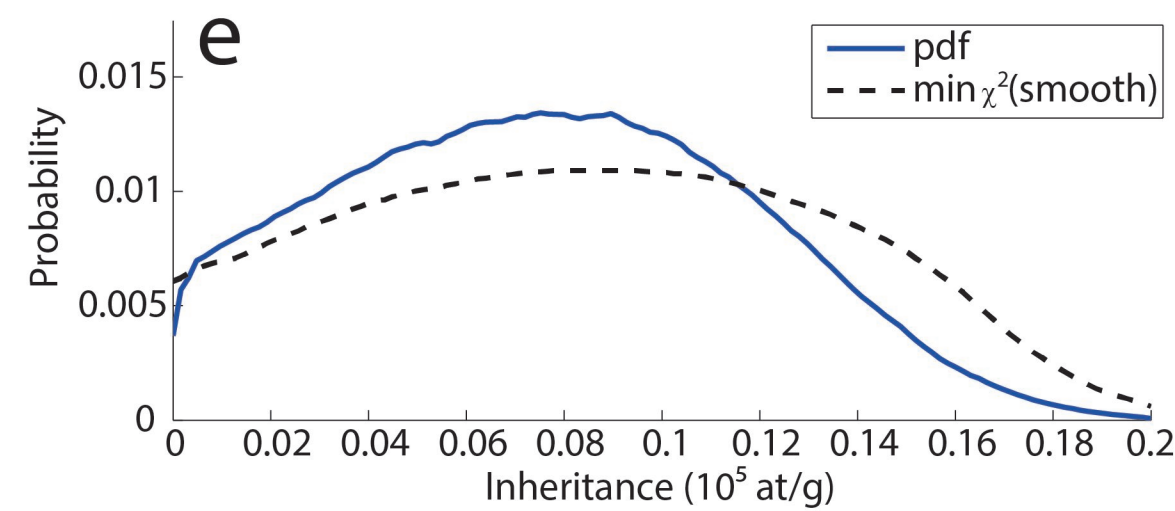
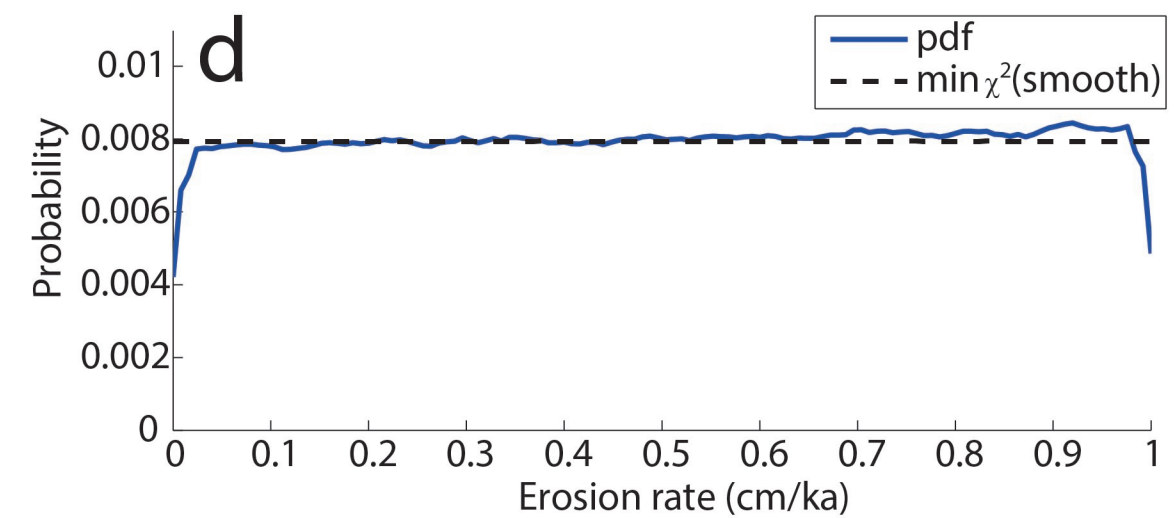
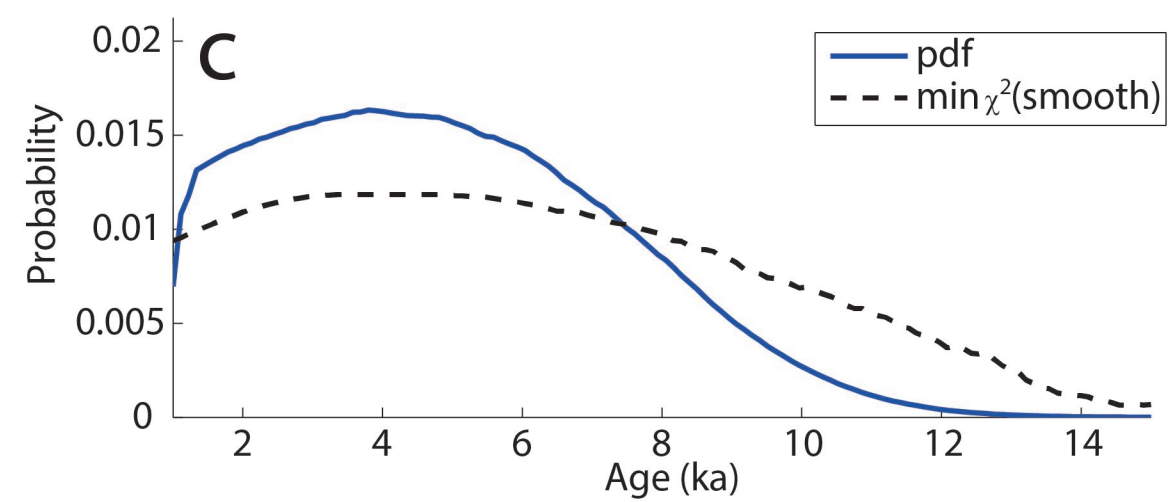
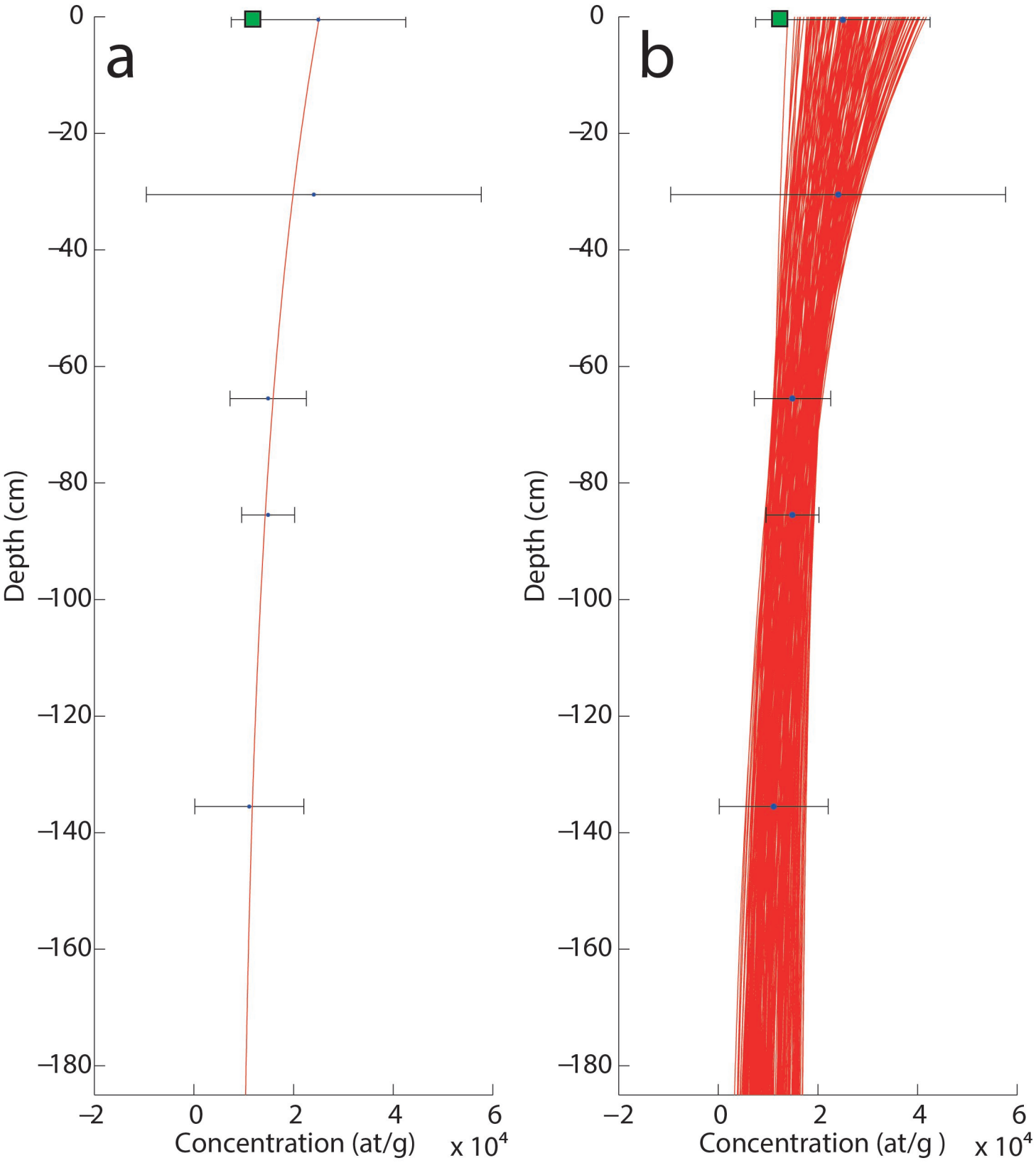


Figure 14.

